# Experimental and computational analysis of bubble generation combining oscillating electric fields and microfluidics

A thesis submitted in partial fulfilment of the requirements for the degree of

**Doctor of Philosophy**

By

**Anjana Kothandaraman**

**Supervised by:**

***Professor Mohan Edirisinghe***

***And***

***Professor Yiannis Ventikos***

Department of Mechanical Engineering

University College London

Torrington Place, London WC1E 7JE

**United Kingdom**

**December, 2017**

# Declaration

I, Anjana Kothandaraman, confirm that the work presented in this thesis is my own. Where information has been derived from other sources, I confirm that this has been indicated in the thesis.

Anjana Kothandaraman

## Abstract

Microbubbles generated by microfluidic techniques have gained substantial interest in various fields such as food engineering, biosensors and the biomedical field. Recently, T-Junction geometries have been utilised for this purpose due to the exquisite control they offer over the processing parameters. However, this only relies on pressure driven flows; therefore bubble size reduction is limited, especially for very viscous solutions. The idea of combining microfluidics with electrohydrodynamics has recently been investigated using DC fields, however corona discharge was recorded at very high voltages with detrimental effects on the bubble size and stability.

In order to overcome the aforementioned limitation, a novel set-up to superimpose an AC oscillation on a DC field is presented in this work with the aim of introducing additional parameters such as frequency, AC voltage and waveform type to further control bubble size, capitalising on well documented bubble resonance phenomena and properties. Firstly, the effect of applied AC voltage magnitude and the applied frequency were investigated. This was followed by investigating the effect of the mixing region and electric field strength on the microbubble diameter. A capillary embedded T-junction microfluidic device fitted with a stainless steel capillary was utilised for microbubble formation.

A numerical model of the T-Junction was developed using a computational fluid dynamics-based multiphysics technique, combining the solution of transport equations for mass and momentum (Navier-Stokes Equations), a Volume of Fluid algorithm for tracking the gas-liquid interfaces, and a Maxwell Equations solver, all in a coupled manner. Simulation results were attained for the formation of the microbubbles with particular focus on the flow fields along the detachment of the emerging bubble.

Experimental results indicated that frequencies between $2 - 10\ kHz$ have a pronounced effect on the bubble size, whereas elevated AC voltages of $3 - 4\ kV_{P-P}$ promoted bubble elongation and growth. It was observed that

reducing the mixing region gap to $100\ \mu m$ facilitated the formation of smaller bubbles due to the reduction of surface area, which increases the shear stresses experienced at the junction. Reducing the tip-to-collector distance causes a further reduction in the bubble size due to an increase in the electric field strength. Computational simulations suggest that there is a uniform velocity field distribution along the bubble upon application of a superimposed field. Microbubble detachment is facilitated by the recirculation of the dispersed phase. A decrease in velocity was observed upstream as the gas column occupies the junction suggesting the build-up in pressure, which corresponds to the widely reported 'squeezing regime' before the emerging bubble breaks off from the main stream.

The novel set-up described in this work provides a viable processing methodology for preparing microbubbles that offers superior control and precision. In conjunction with optimised processing parameters, microbubbles of specific sizes can be generated to suit specific industrial applications.

## Impact Statement

Microbubbles are perceived to introduce interesting textural elements in perishable items such as bread, cakes, chocolates, champagne and sparkling drinks. From a consumer's point of view, products containing bubbles have a sophisticated mouth feel, this is achieved using a gas which represents a zero calorie ingredient thus replacing fat. With nutraceuticals taking an expanding share of the market, it is believed that finer and uniform bubbles will enhance the palatability of functional foods (Ahmad et al., 2012, Shen et al., 2008a).

On the other hand, bacterial biosensing is a rapidly developing field, with particular reference to industrial applications and in public health as a result of the advancements taking place in biotechnology and microelectronics. Microbubbles have been employed in acoustic biosensing platforms as the shell properties influence the electroacoustic response of the bubble. Fine bubbles provide a large surface throughput to bacteria, ranging from $35 - 250\ \mu m$ (Mann and Krull, 2004, Mahalingam et al., 2015). The methodology described in this thesis generates bubbles to the required size range for the aforementioned application.

Alternative procedures to obtain purified water have been investigated due to the steady decline in fresh water sources. Microbubbles have also been introduced into bioreactors to extract biogases such as methane in waste water (Al-mashhadani et al., 2016). Large quantities of microbubbles of $< 150\ \mu m$ are desired in waste water treatment processes due to their high surface area to volume ratio which is essential to separate particulates from potable water. The apparatus presented in this work can be parallelised in order to generate a large quantity of bubbles this application necessitates.

In order to target biomedical applications such as ultrasound contrast agents, the acceptable size range is approximately $2 - 10\ \mu m$, without compromising the production rate or stability of the microbubbles. One of the main findings of this work was that frequency is an important contributor to the reduction in microbubble diameter. Higher frequencies

displayed favourable results in terms of size reduction. This lays the framework for targeting the biomedical field by incorporating an amplifier which has higher frequency capabilities to achieve microbubble sizes within the desired range.

The methodology presented in this research has tremendous potential to prepare microbubbles for various industries. The microbubbles produced are monodisperse and provide the user with a high degree of control over the processing parameters. The experimental apparatus also benefits from low power consumption $(1.2W)$ with prospects to parallelise the T-junctions to increase the scalability. Furthermore, it paves way to construct a portable machine to target each of these applications in economical and scalable way.

# Publications

## Journal Papers

- Kothandaraman A, Harker A, Ventikos Y, and Edirisinghe, M. Novel Preparation of Microbubbles by Integrating Oscillating Electric Fields with Microfluidics (under review).

- Kothandaraman A, Qureshi M, Ventikos Y, Alfadhl Y and Edirisinghe M. Study of the Effect of the Mixing Region Geometry and Collector Distance on Microbubble Formation using a Capillary Embedded Microfluidic Device coupled with AC-DC Electric Fields (in preparation).

## Patent

- Kothandaraman A, Edirisinghe M, Ventikos Y. International Patent Application: “Microbubbles and their generation”, PCT/GB2016/053497, November 2016.

## Conference presentations

- Kothandaraman A, Edirisinghe M, Ventikos Y. The Microfluidic Congress, London, October 2016 (Poster Presentation)

- Kothandaraman A, Qureshi M, Ventikos Y, Alfadhl Y and Edirisinghe M. International Conference on Nanochannels, Microchannels and Minichannels, Washington DC, July 2016 (Technical presentation).

- Kothandaraman A, Edirisinghe M, Ventikos Y UK Society for Biomaterials Conference, London, UK, June 2016 (Technical presentation).

- Kothandaraman A, Edirisinghe M, Ventikos Y. Departmental PhD conference, Department of Mechanical Engineering, UCL, London, UK, June 2015 (Poster and Technical Presentation).

- Kothandaraman A, Edirisinghe M, Ventikos Y. Departmental PhD conference, Department of Mechanical Engineering, UCL, London, UK, July 2014 (Poster and Technical Presentation).

# Acknowledgments

I would like to express my sincere thanks to my primary supervisor **Professor Mohan Edirisnghe** for believing I could achieve great heights. His continual support, valuable guidance and patience have been a great source of motivation.

My thanks are equally due to my secondary supervisor **Professor Yiannis Ventikos**, who has not only imparted a wealth of knowledge to me, but has always been very approachable whenever I needed any advice. It has been an honour to be under the supervision of Prof. Edirisinghe and Prof. Ventikos.

When times have been tough, support from near and dear ones have always pushed me to persevere and achieve the end goal. I would like to extend my thanks to **Dr. John Vardakis** for always guiding me in the right direction and **Mr. Adrian Matei** for his exquisite sense of humour and deep discussions.

I would like to give my sincerest gratitude to my father **Mr. R Kothandaraman**, who has been my role model, inspiration and my source of strength, and my mother, **Mrs. Sheela Kothandaraman**, whose affection and encouragement are invaluable and has always been a strong pillar of support. I credit all my accomplishments to them. To my family, thank you.

Last but not least, I would like to thank God for giving me the determination and endurance to undertake this challenge.

# Nomenclature

| Symbol | Definition | Units |
|---|---|---|
| Ca | Capillary number | Dimensionless |
| $Ca_c$ | Capillary number of the continuous phase | Dimesnionless |
| $D_b$ | Bubble Diameter | µm |
| $D_x$ | Distance between tip-to-collector | mm |
| ε | Relative permittivity | Dimensionless |
| E | Electric field Strength | V/m |
| $E_0$ | Permittivity of vacuum | Dimensionless |
| $L_{ch}$ | Length of the microchannel | m |
| $M_x$ | Mixing region distance | µm |
| $\eta_s$ | Dynamic viscosity of the solution | m Pa s |
| $\eta_w$ | Dynamic viscosity of water | m Pa s |
| Pe | Peclet number | Dimensionless |
| $P_i$ | Gas pressure at the inlet | kPa |
| $P_o$ | Gas pressure at the outlet | kPa |
| $Q_l$ | Liquid flow rate | ml/min |
| Qg | Gas flow rate | ml/min |
| Re | Reynolds number | Dimensionless |
| $R_1$ | Principal radii of curvature in the axial direction | mm |
| $R_2$ | Principal radii of curvature in the radial direction | mm |
| $T_g$ | Glass transition temperature | K |

| | | |
|---|---|---|
| $\mu_l$ | Liquid viscosity | m Pa s |
| $V_{EOF}$ | Electroosmotic velocity | m/s |
| $V_o$ | Peak voltage | V |
| $w_c$ | Inlet width of the continuous phase | mm |
| $w_d$ | Inlet width of the dispersed phase | mm |
| $\zeta$ | Zeta Potential | V |

# Glossary of Abbreviations

| | |
|---|---|
| AMG | Algebraic multigrid |
| BAC | Benzalkonium chloride |
| BSA | Bovine Serum Albumin |
| CEHDA | Coaxial electrohydrodynamic atomisation |
| CFD | Computational fluid dynamics |
| CFL | Courant-Fredrichs-Lewy |
| CFS | Continuum surface force |
| CGS | Conjugate gradient scheme |
| CEHDA | Coaxial electrohydrodynamic atomisation |
| CMC | Critical micelle concentration |
| CT | Computed tomography |
| CTAB | Cetyltrimethylammonium bromide |
| CV | Control volume |
| DAF | Dissolved air floatation |
| ECM | Extracellular matrix |
| E-coli | Escherichia Coli |
| EDL | Electric double layer |
| EF | Electro-flotation |
| EHDA | Electrohydrodynamic atomisation |
| EOF | Electroosmotic flow |
| EWOD | Electrowetting on dielectric |
| FEP | Fluorinated Ethylene Polypropylene |

| | |
|---|---|
| FVM | Finite volume method |
| HIFU | High intensity focused ultrasound |
| HPLC | High performance liquid chromatography |
| HVA | High voltage amplifier |
| LSMBS | Lysozyme microbubbles |
| MRI | Magnetic resonance imaging |
| MUSCL | Monotonic upstream-centred scheme for Conservation Laws |
| NSE | Navier-Stokes equations |
| P-P | Peak-to-Peak |
| PDE | Partial differential equations |
| PDMS | Poly(dimethylsiloxane) |
| PEG 40S | Polyoxyethylene glycol 40 stearate |
| PET | Poly(ethylene terephthalate) |
| PFC | Perfluorocarbons |
| PISO | Pressure Implicit with Splitting of Operators |
| PLIC | Piecewise-linear interface calculation |
| PMMA | Poly(methylmethacrylate) |
| PSU | Power supply unit |
| QUICK | Quadratic upwind Interpolation for convective kinetics |
| SDS | Sodium dodecyl sulphate |
| SIMPLEC | Semi-implicit method for pressure correction-consistent |
| SIMPLE | Semi-implicit method for pressure correction |

| | |
|---|---|
| SIMPLER | Semi-implicit method for pressure correction – revised |
| SLS | Sodium lauryl sulphate |
| VOF | Volume of fluid |

# Table of Contents

# List of Figures

***Figure 30:*** *Optical micrographs of bubbles obtained at a superimposed AC voltage of 2kVP-P, 500Hz at applied DC voltages of i) 0V, ii) 2kV, iii) 4kV, iv) 6kV, v) 8kV, vi) 10kV.*

***Figure 31****: Optical Micrographs of bubbles obtained at a superimposed AC voltage of 2kV P-P, 600Hz at applied DC voltages of i) 0V, ii)2kV, iii)4kV, iv) 6kV, v) 8kV, vi)10kV.*

***Figure 32:*** *Effect of applied AC electric field frequencies on the microbubble diameter. Error bars represent tree standard deviations, estimated from repeat experiments. Curves represent a fit to a simple analytic function.*

***Figure 33:*** *Variation of microbubble diameter as a function of frequency at 2kV P-P AC voltage, 6kV DC Voltage, error bars represent three standard deviations, estimated from repeat experiments. Measured points are connected by straight line segments as a guide to the eye.*

***Figure 34:*** *Optical Micrographs of bubbles of 15% BSA obtained at Mx of a) 200µm, b) 180µm, c) 160µm, d) 140µm, e) 120µm, and f) 100µm.*

***Figure 35:*** *Optical Micrographs of bubbles of 10% BSA obtained at Mx of a) 200µm, b) 180µm, c) 160µm, d) 140µm, e) 120µm, f) and 100µm.*

***Figure 36:*** *Graph of Bubble Diameter versus Mx for 15% wt. and 10% wt. BSA Solutions.*

***Figure 37:*** *Effect of varying Dx at 6kV DC, 2kV AC P-P, 2kHz. A 10% BSA solution was used in the experiments, and Dx values are a) 100mm, b) 80mm, c) 60mm, d) 40mm, e) 20mm.*

***Figure 38:*** *Effect of Dx at 8kV DC, 2kV AC P-P, 2kHz. A 10% BSA solution was used in the experiments, and Dx values are a) 100mm, b) 80mm, c) 60mm, d) 40mm, e) 20mm.*

***Figure 39:*** *Graph summarising the effect of the electric field at 6kV DC and 8kV DC at 2kV AC P-P, 2 kHz for 10%wt. BSA Solution.*

*Figu**re 40:** Optical Micrographs at 6kV at frequencies of a) 2 kHz, b) 4kHz, c) 6kHz, d) 8kHz, and e) 10kHz.*

***Figure 41:*** *Graph summarising the effect of frequency on microbubble diameter with optimised parameters of Mx= 20mm, Dx= 400,000 V/m, 2kV AC P-P at 6kV DC and 8kV DC.*

***Figure 42:*** *Microbubble formation in the T-Junction a) Without an electric field b) DC electric field of 6kV DC and c) AC on DC of 6kV, 2kHz.*

*Fig**ure 43:** Velocity magnitude vector plots of the microbubble with a) No, electric field, b) 6kV DC, c) 6kV DC, 2kHz.*

# List of Tables

# Chapter 1

## Introduction

### 1.1 Introduction and background

Naturally occurring bubbles have captured the interest of meteorologists and marine scientists for many years (Emerson and Bushinsky, 2016, Emerson et al., 1991). For example in oceanography, air bubbles have been described as important contributors to the net biological oxygen production, but also in other gas mass transfer processes, like for example CO2 exchange and sequestration, with implications on ocean acidification, etc. (Emerson et al., 1997).

The primary source of bubble formation on the surface of the ocean occurs as a result of the entrapment of air when a wave breaks on the sea surface. Due to the turbulent nature of flows in the sea, the bubbles are submerged into the ocean where various organic compounds embed themselves along the surface of the bubble. Facilitated by their high surface to volume ratio, gas exchange occurs and modifies the contents in their core. The buoyancy of the bubbles forces them to emerge to the surface and burst into an aerosol suspension in the atmosphere (Blanchard, 1975, Emerson and Bushinsky, 2016, Huang et al., 2017). The high surface to volume ratio is also a useful feature capitalised in the bioprocessing industry to enhance the heat and mass transfer in bioreactors(Jauregi and Varley, 1999).

Gas encapsulated microbubbles stabilised by a surfactant or polymer coating have gained substantial interest amongst researchers over the past two decades, branching out into various industries such as food engineering,

water purification and the biomedical field (Stride and Edirisinghe, 2008, Mahalingam et al., 2015).

They have been extensively used in food engineering as texture modifiers and fat replacers (Shen et al., 2008b, Rovers et al., 2016) to enhance the palatability of food. Their applications extend to waste water treatment processes such as ozonation and floatation (Jabesa and Ghosh, 2016, Wen et al., 2011). Microbubbles play an important role in radiology for enhancing the contrast of ultrasound imaging, targeted drug delivery, sonothrombolysis and a carrier of genes (Janib et al., 2010, Ophir and Parker, 1989, Kiessling et al., 2012, Unger et al., 2004).

In order to cater for a plethora of applications, it is essential to have optimal control over the microbubble production process and to tailor their diameter, monodispersity, surface properties and stability to suit specific applications. Various methods have been investigated to prepare microbubbles of which the microfluidic techniques have established their versatility in various fields for effective microbubble generation. This is because they benefit from advantages such as:

a) They device benefits from low set-up and manufacturing costs when compared to conventional microfluidic chips which are manufactured using more complex techniques such as soft lithography.

b) The device described in this work is simple but provides natural scalability, i.e. there is a potential to utilise multiple T-Junctions in parallel.

c) The microfluidic technique incorporated in this research provides a one-step method to generate monodisperse microbubbles without the need to constantly clean the junction or dispose it, as the capillaries are replaceable in the event of a blockage.

d) Since coarser capillaries are utilised, the pressure drop experienced at the junction is less.

e) This processing technique enables the user to have excellent control over processing parameters, and the application of and oscillating electric field adds a further degree of control by facilitating the formation of smaller bubbles when using a unique combination of parameters.

f) The set-up can be optimised by increasing the intensity of the electric field by reducing the distance between the ground plate and the outlet nozzle.

## 1.2 Research objectives

### 1.2.1 Novel preparation of monodisperse microbubbles by integrating oscillating electric fields with microfluidics

The primary objective of this study is to develop a novel and robust experimental set-up which is able to superimpose an AC on a DC field to a T-Junction microfluidic configuration to prepare monodisperse microbubbles. In addition, the aim was to investigate the effect of the new parameters such as applied AC and frequency on the microbubble production and suggest a rationale behind the electrohydrodynamic phenomenon in the presence of oscillating electric fields.

### 1.2.2 Investigating the effect of the mixing region geometry and the electric field strength on microbubble diameter

The main goal for this section of the work was to develop a more detailed understanding of the apparatus and the features that can contribute to

delivering precision and control of the microbubble size, in addition to the overall production process. Two main experiments were conducted, in the first, relevance was given to the junction area where the two fluid media. In the second experiment, the role of the electric field strength was investigated in order to determine whether the effect of this field can be intensified to further reduce the microbubble size. Finally, to complete this part of the study, the optimal electric quantities and processing parameters achieved in the experiments were employed to develop a robust set-up to efficiently prepare microbubbles of specific sizes to suit various applications.

### 1.2.3 Numerical simulation of the microbubble formation

The objective of this part of the thesis is to develop a 2D computational model of the T-junction with and without the presence of the superimposed AC on a DC electric field. A dedicated flow-solver within an established Multiphysics suite (CFD-ACE+, ESI group, Paris, France) was selected for this purpose. Flow dynamics of the microbubble detachment process in the T-junction is also presented in order to garner a better understanding of the hydrodynamics behind the bubble formation and generate a theoretical framework for future development. This study is concluded by comparing the simulation results with optical micrographs obtained from the experiments.

The research objectives are summarised in the flow chart presented in figure 1.

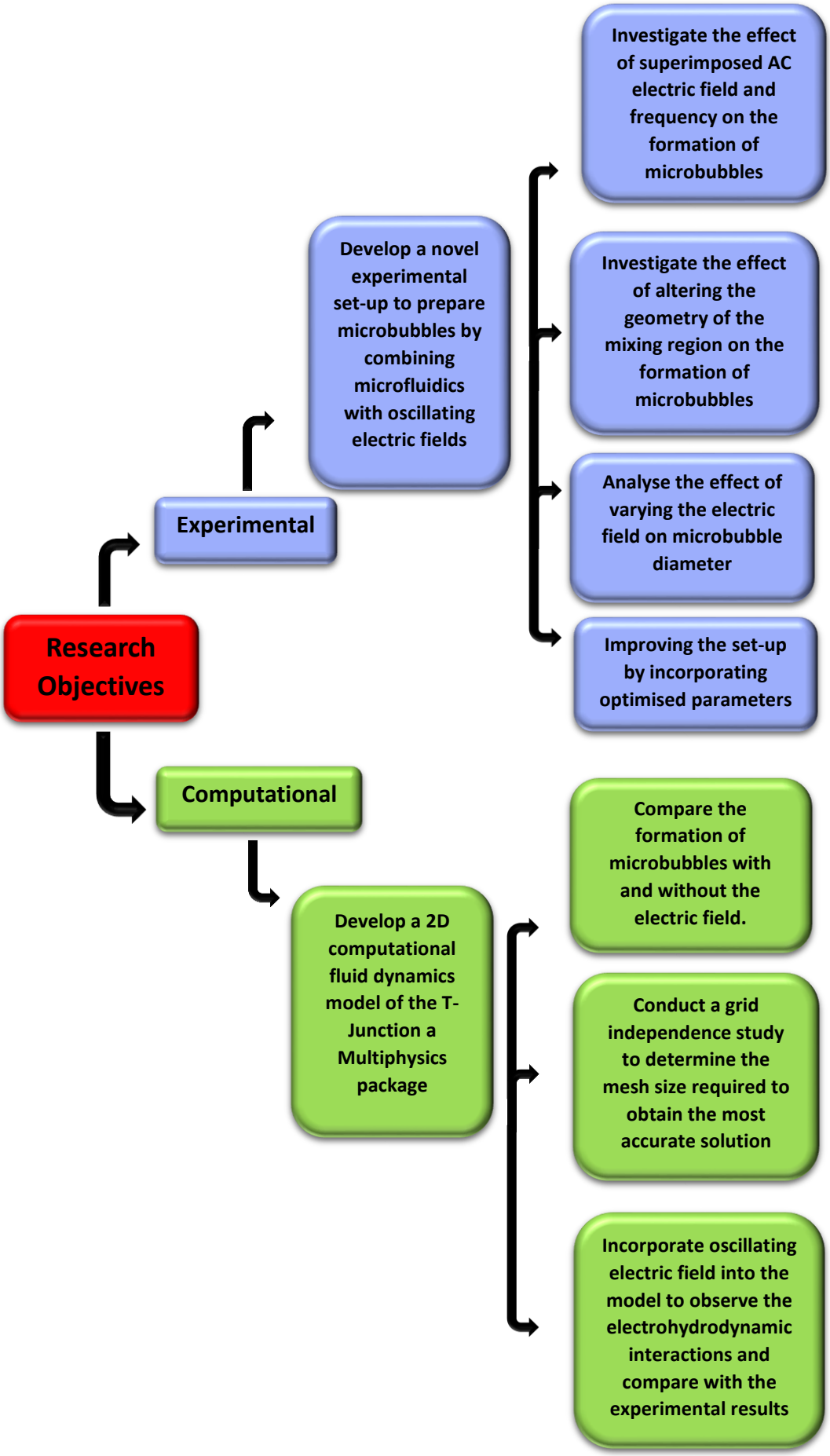


*Figure 1: Computational and experimental objectives of this research.*

## 1.3 Structure of thesis

This dissertation details the way in which the research is proceeded by extensively surveying the literature, development and construction of both experimental set-ups, selection of materials, methodology behind the experiments, and discussion of results followed by concluding remarks. In order to exploit the potential portrayed by the innovative apparatus developed in this research as a viable technique to prepare microbubbles for a plethora of applications such as the food industry and biosensors to name a few, an overview of the thesis is briefly described below:

1) **Chapter 2** presents a detailed review of the literature that has been reported over the years in this area. The aim of the research is to prepare microbubbles through T-junction microfluidics in combination with superimposed electric fields and develop a numerical model. Therefore, an extensive assessment of literature has been undertaken in order to understand the fundamental concepts behind microbubbles and their applications in industry, methods of preparation, electrohydrodynamic theory as well as governing equations that represent the fluid and electrohydrodynamic interactions.

2) **Chapter 3** presents the fundamental equations that represent the fluid flow and the electric field. The Navier-Stokes and Maxwell's equations which model the hydrodynamics and electrohydrodynamics respectively are described in depth, followed by the interface tracking methods that are crucial in multiphase flows. This section also details the discretisation schemes and solvers

available to obtain important quantities related to the dynamics of the system.

3) **Chapter 4** provides details on both novel experimental configurations used in this work, materials used, experiments and characterisation procedures carried out, and finally the calibration protocols. This chapter provides a detailed description of the experimental tools employed, and the datasheets generated to describe the various connections made in this complex system.

4) **Chapter 5**, experimental results obtained using the novel apparatus to superimpose an AC on a DC electric field are discussed. The primary aim is to attain further control over the process and the bubble diameter. This chapter is divided into two sub-sections:

   a) **Section 5.1** presents the experimental set up to superimpose an AC on a DC electric field. The two main parameters that were investigated were the applied AC magnitude and frequency in order to develop a better understanding of the effects they have on the microbubble formation.

   b) **Section 5.2**, which discusses the effect of the mixing region geometry and the electric field strength on the microbubble diameter. Based on the results acquired in sections 5.1 and 5.2, the set-up was optimised with an alternative amplifier capable of delivering higher frequencies along with the parameters that contributed positively towards the reduction of the bubble size.

5) **Chapter 6**, documents the computational model set-up of the T-Junction and corresponding simulation results. The flow field that

governs the microbubble detachment is investigated along with simulation results of bubble formation with and without the electric field always referencing and comparing to evidence from the literature. This chapter concludes by comparing the experimental findings with the simulation results and with a grid independence study.

6) **Chapter 7** is divided into three sub-sections and provides concluding remarks regarding the research presented in this thesis.

   a) **Section 7.1** outlines the main conclusions derived from the experimental and computational work detailed in this thesis.

   b) **Section 7.2** provides recommendations on how the existing work undertaken can be improved or furthered in the future.

   c) Finally, **Section 7.3** reports the marketable aspects of the novel apparatus presented in this work.

# Chapter 2

# Literature Review

## 2.1 Introduction

This section provides a comprehensive review on the applications of microbubbles across the numerous sectors including biomedical engineering, waste water treatment and food engineering. The various methods to prepare microbubbles that have been documented in research papers over the years are reviewed in order to understand the benefits and drawbacks of each processing technique. The different microfluidic systems explored by various authors is surveyed, followed by the hydrodynamics governing bubble formation. This section is concluded by introducing the concept of integrating an oscillating electric field with a microfluidic platform. The theoretical framework on modelling the hydrodynamic and electrohydrodynamic interactions will be covered in detail in chapter 3.

## 2.2 Overview of microbubbles and their applications

### 2.2.1 Food engineering

Bubbles play a vital role in the manufacturing of a plethora of food products such as: ice creams, beverages and cakes. Aeration of food also benefits from low costs and form novel structures that play a vital role in oral sensory perception (Minor et al., 2009). Due to the high surface area of bubbles, there is an increased ability to take up sauces. Their versatility is incorporated in beverages to enhance the visual appeal of soft drinks, beers and wine (Campbell and Mougeot, 1999).

Microbubbles can be described as new colloidal structures which can be used as texture modifiers and fat replacers, which can potentially pave way for the development of healthier food products without compromising their taste (Ahmad et al., 2012, Shen et al., 2008a). Furthermore, substituting conventional microbubbles with microbubbles coated with nutritional ingredients or drugs can increase the nutritional value and introduce medicinal properties in food.

Recently, microbubbles have been employed to intensify the production of yeast due to their efficient mass transfer abilities (Hanotu et al., 2016). They provide a rich oxygen supply to the yeast as opposed to coarser bubbles, therefore a sustainable and cost-effective method for yeast production.

### 2.2.2 Water and wastewater Treatment

Due to the steady decline in the availability of water resources, alternative procedures to obtain purified water, such as sea water desalination, have gained substantial interest (Gwenaelle et al., 2017). Microbubbles have also been introduced into bioreactors to extract biogases such as methane in waste water (Al-mashhadani et al., 2016). The microbubbles provide a gas-liquid interface where the methane aggregates, thus providing a means to exit the system. Dissolved air flotation (DAF) employs microbubbles of diameters < 150µm to separate particulates from potable water by harnessing on their high surface area to volume ratio which improves the mass transfer rate(Hanotu et al., 2013). Shu et al.(Liu et al., 2012b) added that incorporating microbubbles into active sludge results in sludge flotation and accumulation at the surface. Consequently, there is a decrease in sludge volume in the main tank for subsequent eradication or purification processes (Liu et al., 2012a).

Electro-flotation (EF) has been explored to float pollutants to the surface by hydrogen and oxygen microbubbles generated by water electrolysis (Choi et al., 2009). Jimenez et al. (Jimenez et al., 2010) emphasised the importance

of size distribution in this process as smaller bubbles have a larger interfacial area thus increasing the efficacy of the flotation process.

### 2.2.3 Biosensors

Biosensors represent a rapidly expanding field, especially in industrial applications and public health, owing to the rapid advancements made in biotechnology and microelectronics (De Vellis et al., 2017). Biosensors comprise of a biological component which acts like the sensor, and an electronic counterpart that detects and transmits the signal. They have been typically used to test for bioaffinity and to isolate target molecules from complex body fluids (Wang, 2016). Biosensors are used in food safety measurements to detect bacteria such as Escherichia Coli (E-Coli) due to their high level of sensitivity and accurate detection of harmful pathogens (Ten et al., 2017). Recent developments indicate that gas microbubbles coated with an albumin, lipid, phospholipid or polymer shell influence the electroacoustic response of the microbubble, therefore being a feasible option for acoustic biosensing platforms (Zhou et al., 2013). Recent research has indicated that several microbubbles along the same capillary enable simultaneous detection of more than one analyte (Berneschi et al., 2017).

Air filled lysozyme microbubbles (LSMBs) were recently employed to detect insecticides such as Paraoxon, which is a known neurotoxin (Cavalieri et al., 2013). The LSMBs are functionalised with the enzyme alkaline phosphatase (AP). The presence of Paraoxon was shown to inhibit the enzymatic activity of the functionalised bubbles hence determining the presence of this toxin.

### 2.2.4 Targeted drug delivery

Regarding microbubbles, further considerable interest is connected with their applicability in drug delivery and gene therapy. Research has indicated their potential in a diverse range of therapeutic purposes such as cancer diagnosis and cardiovascular applications (Stride and Edirisinghe, 2009).

High intensity focused ultrasound (HIFU) intervention is used as a viable tissue ablation approach (Stride, 2009) and an alternative to surgery. Microbubbles are used in conjunction with HIFU in order to improve the efficacy of the process by accelerating both the heating and the mechanical effects caused by ultrasonic energy (Yoshizawa et al., 2017). Microbubbles begin to oscillate when subjected to ultrasound, which increases the dissipation of thermal energy, thus destroying the target volume. This is advantageous as it does not involve a complex surgical procedure and is non-invasive; furthermore side effects commonly associated with cancer treatment such as chemotherapy can be moderated.

Recent advances in microbubble technology have also been shown to enhance the permeability of both, cell membranes and the endothelium (Unger et al., 2014). For example, delivery of therapeutic agents across complex vasculature such as the blood brain barrier (BBB) is an ongoing challenge to treat various neurological diseases (van Wamel et al., 2006).

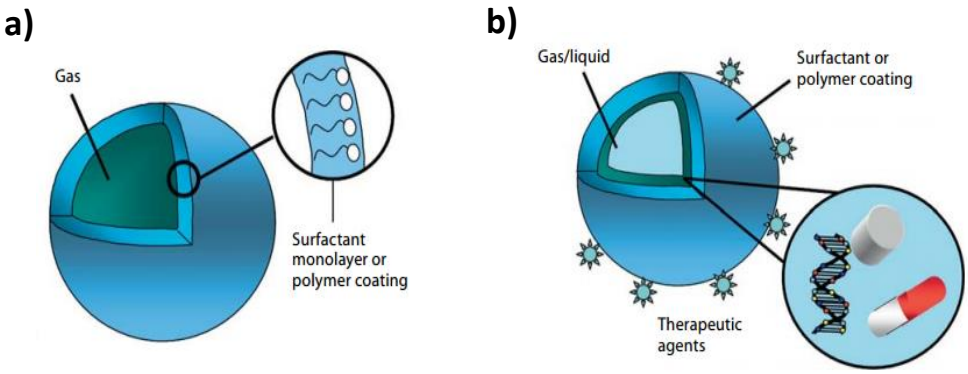


*Figure 2: a) Structure of conventional microbubble with a gas core encapsulated with a surfactant or polymer shell b) Multi-layered microbubble with an outer shell embedded with therapeutic agents (Stride, 2009).*

The structure of a microbubble containing therapeutic agents is shown in figure 2b. Once accumulation of the microbubbles occurs at the target site, stable pulsation of the ultrasound known (cavitation) can be applied. Oscillating properties of microbubbles as a result of focused ultrasound temporarily changes the vasculature by creating minor openings between the endothelial cells in the BBB(Miller and O'Callaghan, 2017). This cavitation

force causes the bubble to expand and contract rhythmically allowing steady dispensation of a drug. This is accompanied by the enhanced permeability of the membrane to the therapeutic agent, which optimises the overall drug delivery process as shown in figure 3. This eliminates the need for more invasive surgical procedures such as craniotomy and their associated complications.

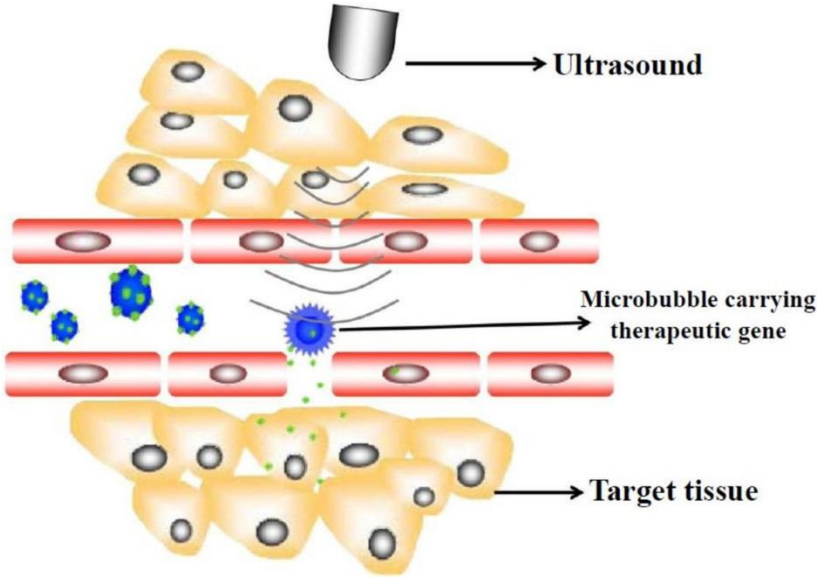


*Figure 3: Ultrasonic energy increases the permeability of the vessel wall. The steady release of the therapeutic agents to the affected region ensues (Chen et al., 2013).*

### 2.2.5 Ultrasound contrast agents

In comparison to other imaging modalities such as magnetic resonance imaging (MRI) and computed tomography (CT), ultrasound imaging is widely available and inexpensive. It is also the safest form of medical imaging as ultrasound does not emit any ionising radiation hence commonly used in foetal imaging. Microbubbles play a vital role in the preparation of contrast agents for ultrasound imaging. This is due to the useful properties they possess, such as their high compressibility and ability to undergo linear and non-linear oscillations as an acoustic response to ultrasound signals. The typical structure of a microbubble used in contrast agents consists of a gas

core, with a stabilising coating of a surfactant or a polymer as shown in figure 2a. When a suspension of microbubble contrast agents are intravenously injected into the body, the contrast between the blood vessels and the surrounding tissue is significantly improved in the ultrasound image generated thus aiding radiologists with their diagnosis(Cui et al., 2005). Targeting ligands have also been incorporated onto the shell of the microbubble to image selective targets in the body including inflammatory bowel disease, ischemia and atherosclerosis (Caskey, 2017, Mott et al., 2016, Rafailidis et al., 2017).

### 2.2.6 Tissue engineering scaffolds

Injury, disease conditions and trauma can potentially lead to damage and destruction of tissues, which necessitates treatment or therapy to promote healing, repair and/or regeneration (O'Brien, 2011). The aforementioned issues compromise the structural integrity of the natural extracellular cellular matrix (ECM), thus requiring a supporting structure to mimic the role of the ECM. An ideal tissue engineering scaffold needs to provide an effective compromise between mechanical function and steady release of bioactive agents for the regulation of cell activities (Chan and Leong, 2008).

Although denser scaffolds offer better structural integrity, porous features enable interconnectivity for cell migration and temporary resistance to biodegradation upon implantation. Several factors including pore shape, size and their spatial distribution along the scaffold need to be considered during their development(Bonfield, 2006). Scaffolds displaying spherical pores provide excellent mechanical properties and resist compressive stresses as opposed to non-homogenous pores (Elsayed et al., 2016).

Microbubble foams have been used as the porous components of a scaffold. Lima et al. (Lima et al., 2012) integrated lipid coated microbubbles to prepare porous hydrogel scaffolds. They recorded a two-fold increase in engineering cartilage properties. Nair et al. (Nair et al., 2010) also observed

an increased rate of cell proliferation using protein microbubbles, indicating the suitability of microbubbles in tissue engineering scaffolds.

## 2.3 Stability of microbubbles

The periodic break-up of a liquid stream leads to the formation of bubbles. It is of paramount importance that the microbubbles retain their structure and do not dissolve prior to performing their required function. The stability of the bubbles formed is governed by their resistance to the gravitational drainage, drainage by capillary suction between regions with different radii of curvature (Laplace equation), and finally the gas diffusion through the liquid shell induced by the pressure gradient between the two bubbles (Beneventi et al., 2001).

Microbubble stability can be optimised by the effect of surface tension, making it more resistant to gas permeation (George et al., 2017). Various materials are used to form the coating or shell of the microbubbles including polymers, lipids and proteins depending on the application. For example, lipid and protein shelled microbubbles provide better cell viability and transfection rate of genetic material than microbubbles with a polymer shell (Wu et al., 2015). Microbubbles can also be stabilised by varying the gas used to fill the core and by the addition of nanoparticles to the surface.

### 2.3.1 Stabilisation by low diffusivity gases

Microbubble contrast agents are employed in ultrasound imaging due to their highly compressible nature which scatters ultrasound more effectively than blood. This feature is as a result of the gas core which generates a strong echo and significantly enhances the contrast (Riess, 2003). Air bubbles tend to dissolve rapidly in the blood as a result of the combination of the Laplace pressure, arterial pressure, oxygen metabolism and ultrasound energy. This ultimately renders them undesirable for this

application. To mitigate this, microbubbles are filled with gases of high molecular weight such as perfluorocarbons (PFC), Sulphur hexafluoride and nitrogen due to their high degree of stability and inertness, absence of metabolism, density and gas dissolving capacity (Riess, 2002, Forsberg et al., 1999).

Forsberg et al. (Forsberg et al., 1999) reported that the durability of the injected microbubbles increases at lower Ostwald coefficients. This dimensionless number is the ratio between the gas solubility in the liquid to the gas density $(mol/m^3)$, their observations conform to the findings of Sridhar et al. (Sridhar et al., 2016).

Microbubbles stabilised by gases with low Ostwald coefficients have generated tremendous interest in biomedical applications such as oncology to target tumour cells, intravascular oxygen transport, ophthalmology and pulmonary drug delivery (Liu et al., 2017, Riess and Krafft, 1998). All the commercially available microbubble agents for therapeutics and diagnostics are stabilised by PFC compounds such as perfluorobutane, perfluoropentane and perfluorohexane (Rossi et al., 2010, Kwan et al., 2012, Mountford and Borden, 2016).

### 2.3.2 The role of surfactants in microbubble stability

Due to the nature of the applications discussed in section 2.2, there is significant interest in increasing the life-time of the microbubbles. As a result of the interfacial action along the surface of the bubble, they are naturally unstable. The effect of the capillary pressure acting on the spherical microbubble surface can be expressed by the Laplace equation:

$$\mathrm{P}_{\mathrm{Laplace}} = \frac{2\sigma}{R} \qquad (2.1)$$

Where $R$ is the instantaneous radius $(m)$, and $\sigma$ represents the interfacial

tension ($Nm^{-1}$). The diameter of the microbubble decreases exponentially as the gas diffuses into the surrounding liquid at a constant ambient environment.

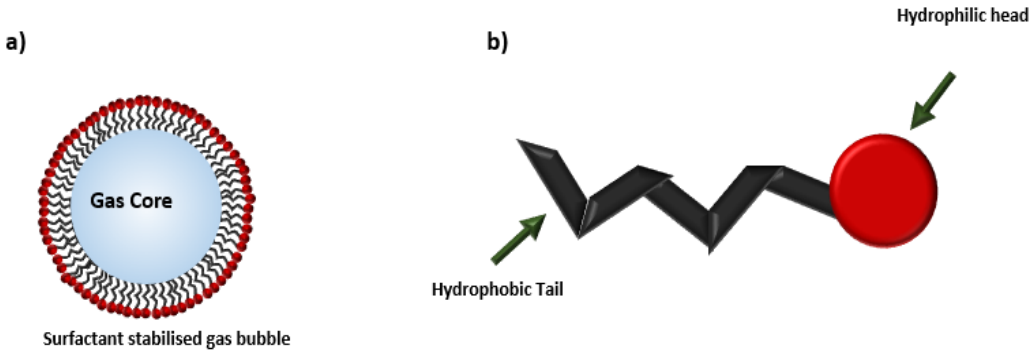


*Figure 4: a) Schematic of adsorption monolayer of a gas bubble coated with a surfactant b) Molecular structure of surfactant depicting the hydrophobic and hydrophilic components.*

| | Type | Hydrophilic head polarity | Example of surfactants |
|---|---|---|---|
| **1** | Anionic |  | - Sodium lauryl sulphate (SLS) (Fan et al., 2017)<br>- Sodium dodecyl sulphate (SDS) (Zhao and Qi, 2006)<br>- Long chain alkyl acids (fatty acids, N-acyl amino acids(Che et al., 2003) |
| **2** | Cationic |  | - Cetyltrimethylammonium bromide (CTAB) (Landfester et al., 1999)<br>- Benzalkonium chloride (BAC) (Scharff and Maupin, 1960) |
| **3** | Zwitterionic | 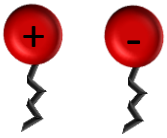 | -Sulphobetaines(positively charged trimethylammonium and negatively charged sulphonate) (Zhu et al., 2017) |
| **4** | Non-ionic |  | -Polyoxyethylene glycol octylphenol ethers(Rahimpour et al., 2007)<br>-Polyoxyethylene sorbitan fatty esthers (Gou et al., 2017) |

*Figure 5: Table summarising the various classes of surfactants and corresponding examples*

Surfactants are added to control the interfacial tension between the immiscible streams and facilitate bubble formation (Xu et al., 2006, Parhizkar et al., 2015). A surfactant is said to have three well known influences on bubble motion: (i) reduction of rising velocity, (ii) prevention of coalescence and (iii) the reduction of mass transfer. In a surfactant containing system, the critical micelle concentration (CMC) is a fundamental parameter(Xu et al., 2009). Studies indicate that at the CMC, the surfactant begins to aggregate to form structures known as micelles; in order for the maximum effect of the surfactant to be present, the concentration of the surfactant must exceed the CMC.

Surfactants have a characteristic molecular structure comprising a structural group called the Lyophobic group (the hydrophobic component), which has little attraction for the solvent. This is combined with a group that has a strong attraction for the solvent known as the Lyophilic group (the hydrophilic component), this structural formation is known as an amphipathic structure (Rosen and Kunjappu, 2012). The hydrophobic group is usually a long chain hydrocarbon residue, and the hydrophilic group is a highly polar group. These structures align themselves such that the hydrophilic head is in contact with the aqueous medium and the hydrophobic tails orient themselves away from the aqueous phase as shown in figure 4.

The surfactants can be classified based on the polarity of their hydrophilic group as anionic (positive) , cationic (negative), zwitterionic (positive and negative) and non-ionic (neutral polarity) (Fan et al., 2017, Zhao and Qi, 2006, Landfester et al., 1999, Rahimpour et al., 2007, Gou et al., 2017).

### 2.3.3 Nanoparticle loaded microbubbles

An alternative method of bubble stabilisation is by incorporating solid nanoparticles onto the microbubble surface. Mohamedi et al. (Mohamedi et al., 2012) introduced gold nanoparticles onto the microbubble surface, which was observed to improve the microbubble stability, attributing to the

Pickering stabilisation phenomena in liquid-liquid emulsions. Pickering emulsions are described as emulsions that are stabilised by solid particles, which adsorb onto the interface between the two phases (French et al., 2016). Pieranski (Pieranski, 1980) established that this process is facilitated by the interplay of interfacial tensions, resulting in the irreversible adhesion of the particles to the interface with energies that are several orders of magnitude greater than the thermal energy present at the interface.

Gozenbach et al.(Gonzenbach et al., 2006) reported a versatile yet simple approach to prepare high stable foams that are stabilised by nanoparticles. The emphasised that particle-stabilised foams alleviates the instability associated with the gas-liquid interface. This instability constitutes a driving force for decreasing the interfacial area of the foam via coalescence and disproportionation if the bubbles. Similarly, Juillerat et al. (Krauss Juillerat et al., 2011) incorporated hydrophobised colloidal particles to the air-water interface using short-chain amphiphiles which modify the wetting behaviour of the particles *in-situ*. The ability to control the wetting properties enables the preparation of suspensions containing a high concentration of hydrophobised particles. This in turn, results in the production of homogenous foams, which feature closed-porous microstructures upon drying (Gonzenbach et al., 2006).

Metallic foams have been used in various industrial applications such as filters, impact absorbers and to manufacture porous ceramics and polymers (Colombo and Degischer, 2010, Studart et al., 2012). Studart et al.(Studart et al., 2012) introduced surface-active nanoparticles to stabilise foams and emulsions through their irreversible adsorption at the gas– liquid and liquid–liquid interfaces, respectively. The nanoparticles are made surface-active by tuning their wettability in the continuous liquid phase where they are initially dispersed. They highlighted that the resultant wet foams prepared remained extremely stable even when the bubbles or nanoparticles were separated by just a few layers of nanoparticles.

## 2.4 Current preparation techniques

In order to meet the increasing demand for microbubbles and the ability to obtain more control over their preparation, numerous technologies have been developed to generate microbubbles. Amongst these techniques are sonication, electrohydrodynamic atomisation (EHDA) and microfluidic devices (Keller et al., 1989, Farook et al., 2007a, Hettiarachchi et al., 2007) as shown in figure 6. Farook et al.(Farook et al., 2007a) explored the various parameters to obtain the microbubbling regime by EHDA; although they were able to attain microbubbles at diameters < 10µm, the microbubbles were not entirely monodisperse, but displayed a narrower size distribution in comparison to sonication.

$Monodispersity$, defined as having coefficient of variation $(the\ standard\ deviation\ divded\ by\ the\ mean\ diameter\ x\ 100)$ less than $5.0\%$ (Seo et al., 2010) is crucial in ultrasound contrast agents because a homogenous contrast agent population generates similar radial oscillations from ultrasound pulses, thus a smaller variation in the echo is received (Hettiarachchi et al., 2007). Microfluidic devices deliver precision and exceptional control over microbubble size and size distribution making them a high throughput platform to generate microbubbles for various applications(Teh et al., 2008). This section provides a detailed review of the various techniques that have been investigated to prepare microbubbles.

### 2.4.1 Sonication

Sonication involves agitating particles within a solution using ultrasound, and is also known as acoustic emulsification (Feshitan et al., 2009). In this process, high intensity ultrasound is used to generate a suspension of microbubbles in a liquid containing an appropriate coating of a surfactant or polymer which forms the stabilising coating on the microbubble shell.

Feshitan et al. (Feshitan et al., 2009) reported that the emulsification process occurs in two main stages; the first phase occurs due to the disruption

caused by ultrasound waves at the surface, initiating the bubble formation. The second phase involves inertial cavitation, which facilitates the breakdown and further reduction of the droplet size until the required bubble stability and size is reached. Bubble stability is promoted via the equilibrium between surface tension and inertial forces at the droplet surface.

This technique is disadvantaged by the large size distribution of microbubbles formed, requiring additional fractioning techniques to isolate the larger bubbles (Szíjjártó et al., 2012, Park et al., 2010). The size distribution primarily depends on the frequency, power and pulse of the ultrasound. Stride and Edirisinghe (Stride and Edirisinghe, 2009) reported that sonication generated bubbles with a polydispersity index (PDI, is defined as the ratio between the standard deviation and mean diameter in percentage) of $\sim 150\%$ limiting their potential use in medicine (Castro-Hernandez et al., 2011).

### 2.4.2 Electrohydrodynamic atomisation (EHDA)

Electrohydrodynamic Atomisation (EHDA) is process whereby a fluid is passed through a needle at a controlled flow rate and maintained at a high DC voltage (several kilovolts), the liquid meniscus deforms into various shapes under the influence of the electric field (Mahalingam et al., 2014). The first published experimental study of this process was conducted by Zeleny (Zeleny, 1914) along with a scientific description. In this process, a liquid is supplied to a metal nozzle at a low flow rate, a droplet is formed at the tip of the nozzle forming a hemispherical shape as a result of surface tension (Hartman et al., 1999). A strong electric field is applied tangentially to the droplet which generates electric stresses along the surface. Positive and negative charges separate inside the liquid and charges of the same polarity as the nozzle move towards the drop surface, inducing a surface charge density (Borra et al., 2004). Thus, the electrostatic pressure, induced at the liquid surface, increases against the capillary pressure forcing the

droplet to elongate to form a conical shape commonly known as the $Taylor\ Cone$ (Taylor, 1964, Doshi and Reneker, 1993).

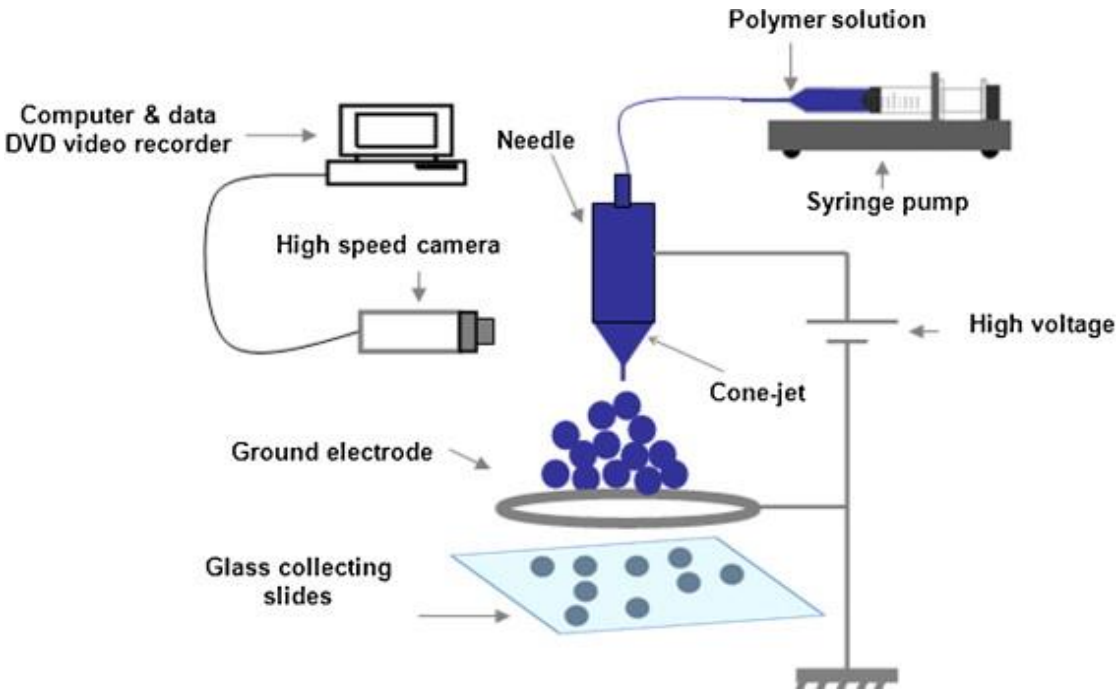


*Figure 6: Schematic diagram of a single needle electrohydrodynamic arrangement (Enayati et al., 2011).*

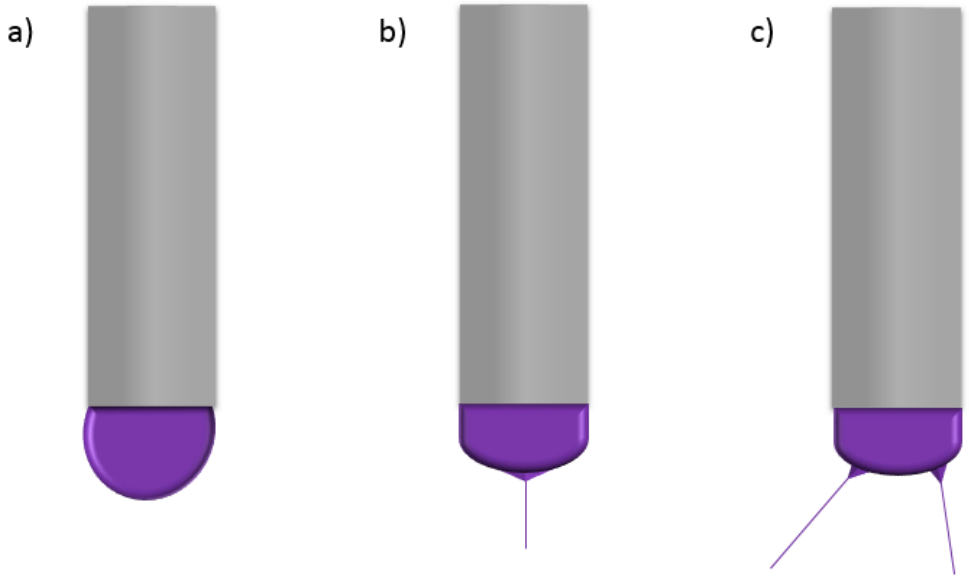


*Figure 7: Schematic showing different modes of electrohydrodynamic atomisation a) Dripping mode b) Stable cone-jet mode c) multi-jet mode.*

As the intensity of the electric field increases, it reaches a critical limit, known as the Rayleigh limit (Xie et al., 2006). When the electrostatic force overcomes the surface tension of the droplet as the charges towards the liquid surface are accelerated towards the cone apex, from which a thin jet emerges which either. Depending on the specific processing parameters such as collector distance, voltage and solution properties, these techniques can produce micro- and nano-scale fibres, particles or droplets(Wu and Clark, 2008). Figure 6 illustrates a typical EHDA apparatus, which consists of a single needle supplied with a fluid from a syringe pump.

There are numerous manifestations of the meniscus under the influence of the electric field including the micro-dripping mode, multi-jet mode and stable cone-jet mode. These are schematically represented in figure 7.

#### 2.4.2.1 CEHDA using DC electric fields

Coaxial Electrohydrodynamic Atomisation (CEHDA)(Farook et al., 2007a, Farook et al., 2007b) has evolved from customary electrohydrodynamic atomisation. In this technique, two different fluid media are pumped using two syringe pumps. The fluids flow into a set of co-axially arranged needles, which is then atomised by the introduction of a steady DC electric field at the nozzle of the outlet. As the intensity of the electric field is further increased and the repulsive electric forces overcomes the surface tension, a charged jet of the solution is ejected from the tip of the Taylor cone. A schematic of the apparatus for CEHDA is exemplified in figure 8.

In this process, there are three sub-processes that have been identified, leading to microbubble formation. These are bubble dripping, coning and microbubbling (Farook et al., 2007a). When an equilibrium between the gas and liquid has been established, the meniscus formed is a droplet composed of air-filled microbubbles. As gravitational forces exceed the surface tension experienced at the nozzle, the droplet encompassing the bubbles detaches, this is known as the dripping mode. Once a potential difference is introduced, the droplet takes the shape of cone called a $Taylor\ Cone$,

referred to as the coning mode. As the applied potential difference is increased, the coning mode progresses into the microbubbling mode. Although CEHDA enables a single-step preparation of multi-layered gas-bubbles; the inability to obtain uniform microbubbles is still a significant drawback of this system.

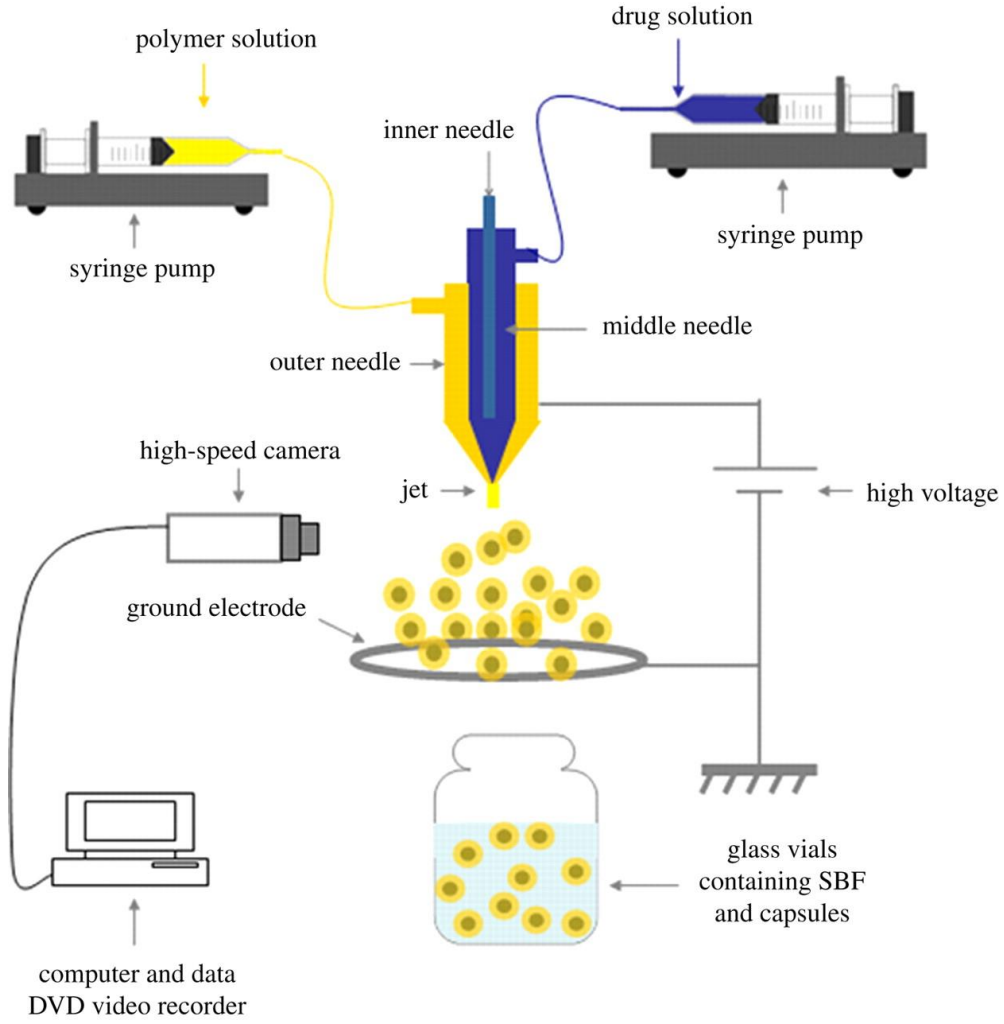


*Figure 8: Schematic representation of the CEHDA arrangement (Enayati et al., 2010).*

### 2.4.2.2 EHDA using AC electric fields

A significant amount of research has been conducted by incorporating AC electric fields in Electrohydrodynamic setups (Maheshwari et al., 2009, Yeo et al., 2005, Demekhin and Polyanskikh, 2010, Tan et al., 2014). DC fields

encompass a time-invariant cycle, as opposed to AC electric fields where the direction changes (alternates periodically).

The use of AC electric fields involve introducing another variable i.e. the frequency (Hz); this is the number of waves that pass a given point in one second. There is an electrical stress associated with electrohydrodynamic arrangements known as the $Maxwell\ Pressure$ which is represented by $\varepsilon E^2/2$, where ε is the permittivity and E is the electric field. As the ions accumulate at the liquid/capillary interface, a corresponding charge build-up occurs, resulting in droplet detachment or spraying when this charge over comes the surface tension of the emerging liquid.

Maheshwari et al. (Maheshwari et al., 2009) reported that varying the frequency resulted in contrasting jet behaviour. They also observed that low frequency electrospraying displayed similar results to DC electrospraying. They matched the applied frequency to the resonant frequency of the droplet ($\leq 10\ kHz$) the resultant effect being the formation of a transient polyhedral Taylor cone that ejects liquid every half cycle. In contrast, increasing the frequency of the sinusoidal wave $\geq 10\ kHz$ caused varied deformation of the meniscus, and past $6kV_{p-p}$, corona discharge occurred which promoted droplet ejection.

Similarly, Yeo et al. (Yeo et al., 2005) observed that frequencies between $20 - 50\ kHz$ lead to droplet detachment, producing droplet sizes below 10µm. They emphasized the importance of droplet size with regard to targeted drug delivery to various respiratory organs. In order for a droplet to encapsulate the required dosage, in addition to safely traversing through the respiratory airways, a bubble diameter of 2.8µm is required. Demekhin and Polyanskikh (Demekhin and Polyanskikh, 2010) showed that implementing an AC electric field offers advantages over DC fields, such as the electric neutrality of the resultant droplets formed. This conforms with the theories laid out by Yeo et al. (Yeo et al., 2005) who added that electro-neutrality of the droplets prevents the occurrence of Rayleigh Fission and the system has a lower power requirement.

Tan et al. (Tan et al., 2014) implemented the use of AC fields into their flow-focusing microfluidic unit to obtain further control over droplet size at the flow-focusing junction, during the dripping regime of the jet break-up. They elucidated that the conductivity of the dispersed phase and field frequency greatly influence the stability of the droplet production, which indicates that fluids of different conductivities can be selected to facilitate stability of the droplet or compounds. An example is the use of Sodium Chloride (NaCl), which can be added to simply increase the conductivity of the solution such that the applied potential difference has the required effect on the liquid jet.

Lastochkin and Chang (Lastochkin and Chang, 2005) employed high frequency AC in their electrospraying apparatus. They observed the continuous deposition of submicron drops at the substrate and attributed this phenomenon to Maxwell stress at the liquid meniscus. The Maxwell stresses stretches the emerging droplet into a conical shape and periodically ejects the charged droplets at frequencies above $1\ kHz$. Similarly, Zheng at al. (Zheng et al., 2014) recorded an increase in deposition rate of the droplets as higher frequencies were utilised. Maheshwari and Chang (Maheshwari and Chang, 2006) postulated that higher frequencies facilitated the stabilisation and growth of the liquid meniscus.

#### 2.4.2.3 EHDA using oscillating electric fields

Another idea that has been explored in literature is superimposing an AC on a DC electric field (Jaworek et al., 2000, Balachandran et al., 1992, Huneiti et al., 1996, Sarkar et al., 2007) and vary the amplitude of the AC . Depending on the applied frequency and amplitude, the bubbles are subjected to non-linear oscillations, which results in their break-up when further increased (Movassat et al., 2015).

The electrospray system in conjunction with an AC/DC excitation was first proposed by Vonnegut and Neubauer (Vonnegut and Neubauer, 1952). They controlled the droplet formation process by an AC voltage of 60 Hz, and

suggested that the use of pulsed DC electric fields can control the frequency of droplet formation.

Movassat et al.(Movassat et al., 2015) modelled the oscillatory behaviour of a bubble when subjected to large vibrations. The bubble begins to deform, resulting in the formation of a dimple in its centre as shown in figure 9a. When this oscillatory force increases, the bubble undergoes break up. These authors suggested that this break-up is facilitated by a thin liquid jet that forms within the core of the bubble (figure 9b).

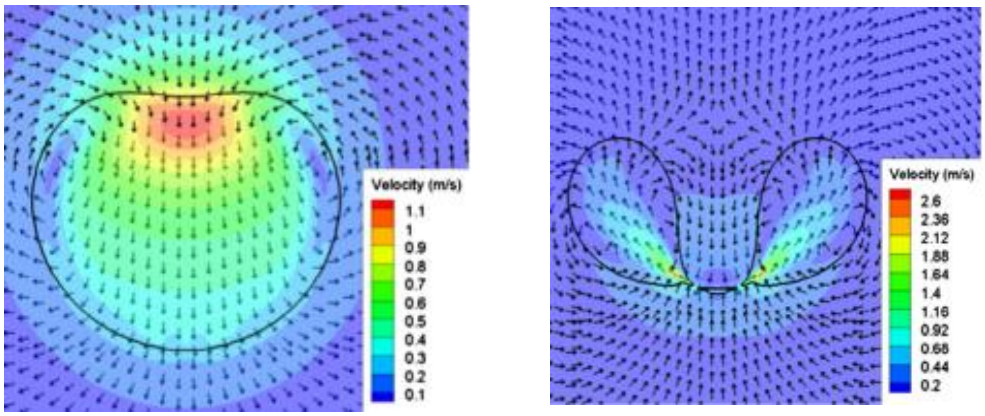


*Figure 9: a) Cavitation of bubble resulting in the formation of a slight depression in the centre of the bubble b) a cut forms through the centre of the bubble due to increase in oscillatory force, the two halves are held together by a thin liquid jet (Movassat et al., 2015).*

In bubble dynamics, the resistance to change in velocity (inertia) of the liquid penetrates towards the centre of the bubble, altering the bubble volume. Jagannathan et al. (Jagannathan et al., 2011) added that when bubbles suspended in liquid are subjected to an acoustic vibration of specified frequencies, they experience variations in the surrounding pressure. They observed rapid fragmentation of bubbles at high frequencies as a result of the cavitation and subsequent deformation of the larger bubbles which is in accordance with the research conducted by (Movassat et al., 2015).

Plesset and Prosperetti (Plesset and Prosperetti, 1977) added that under applied steady pulsation, radial acceleration becomes concentrated towards

the core of the bubble. When the radius of the bubble contracts increasing the likelihood of dip formation and subsequent break-up.

Superimposed AC on DC fields have been employed in electrospraying of droplets. Jaworek et al. (Jaworek et al., 2000) indicated that mechanical methods of droplet formation limited the applied frequency to the harmonic frequency of the liquid jet, however combining a DC voltage with a superimposed AC voltage enables use of set steady state DC electric field, with an applied oscillation (sinusoidal, square) at a peak-to-peak (P—P) value (Huneiti et al., 1995, Jaworek et al., 2000). An example of setting the DC voltage to $5\ kV$ with a superimposed AC voltage of $4\ kV_{P-P}$ is shown in figure 10.

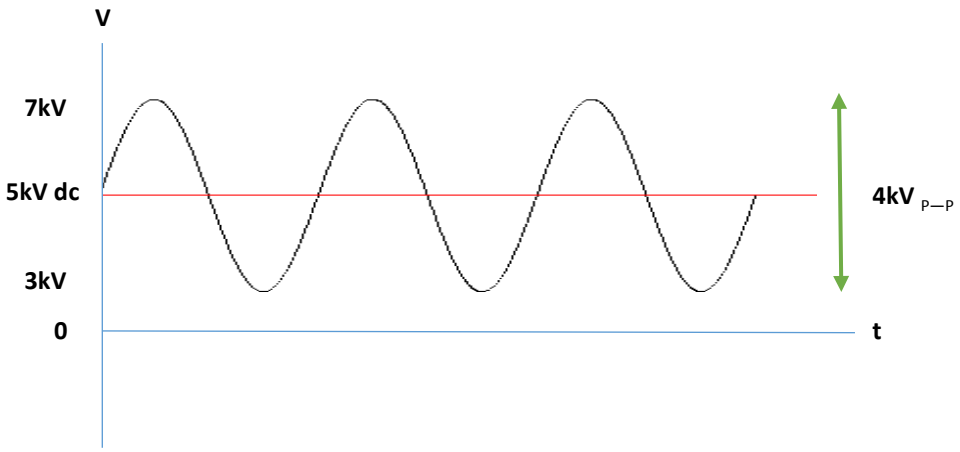


*Figure 10: A 2kV P-P AC superimposed on 5kV DC electric field.*

Balachandran et al. (Balachandran et al., 1992) indicated that an instability known as the whipping instability was recorded in DC electrospray arrangements, this was eliminated when an appropriate AC field and frequency was set, resulting in normal axisymmetric disturbance forming monodisperse droplets. They observed that increasing the frequency from $1500\ Hz$ to $1900\ Hz$ resulted in an increase in droplet formation and a subsequent decrease in droplet size, indicating that the magnitude of frequency can be used to tailor droplet diameter depending on the application they are being developed for. The whipping instability brought by the charge relaxation effect in DC is eliminated by AC fields as the period of the alternating field is longer than the charge relaxation time. The

resulting jet is stabilised by the aid of a shear force which is promoted by the polarisation effects and dielectric loss. Sarkar et al. (Sarkar et al., 2007) note that the combination of positively and negatively charged regions reduce the electrostatic repulsion prevalent in unipolar regions, thus increasing the stability of the fibres that are formed.

Huneiti et al. (Huneiti et al., 1996) indicated that the amount of charge dissipated by a DC and an AC/DC field with respect to the mass can be related by the charge to mass ratio $(Q/m)$ . They measured the current of the spray ejected from the nozzle when subjected to DC and AC/DC fields and the corresponding charge to mass ratio under these electrical stresses. They recorded a higher magnitude of spray current when only a DC field is used, and attributed this phenomena to the high percentage of very fine droplets in the polydisperse spray. Homogenous droplets combined with lower spray current and $(Q/m)$ were observed with AC/DC electric fields due to the absence of unwanted additional droplets also referred to as satellite droplets. Jaworek (Jaworek, 2007) controlled the droplet size by the bias, AC voltage magnitude, AC voltage frequency and the volumetric flowrate of the liquid.

Tran et al.(Tran et al., 2009) employed an AC superimposed on DC electric field for an EHD based drop-on-demand printing device. The indicated that during spraying, the electric field within the liquid will result in an accumulation of the free charge at the surface of the charged meniscus. As a result of the finite conducting nature of the dielectric liquid, a voltage difference will exist between the base of the cone and the end of the nozzle and the tip of the cone. This voltage difference ensures that the interface is subjected to a tangential electric field $E_t$ in the direction of the flow. The tangential electrical stress experienced at the cone becomes

$$\tau_t = \varepsilon_0 E_t E_n \qquad (2.2)$$

where $\varepsilon_0$ is the permittivity of free space and $\varepsilon_0 E_n$ describes the surface charge. Li and Zhang(Li and Zhang, 2009) emphasised that the DC voltage as well as the amplitude of the superimposed AC voltage could affect the droplet formation process as well as the size. Their observations included that higher DC voltages result in the formation of smaller bubbles, and that increasing the superimposed component led to an increase in droplet diameter. However, the width of the waveform did not contribute to a significant difference in the droplet diameter. Kim et al.(Kim et al., 2008) obtained droplet sizes between $95 - 200\mu m$ by varying the frequency of the superimposed AC voltage between $0 - 30kHz$. They were also able to exploit this technique for drop-on-demand patterning enabling the formation of uniformly patterned drops with uniform spacing corresponding to each voltage pulse.

Although, electrospraying using superimposed AC on DC electric fields enables the formation of droplets between $1 - 4\mu\mathrm{m} \pm 1.4$ . However, electrospraying requires very low flow rates $(0.5 - 4\mu m)$ in order for the meniscus to be atomised by the applied voltage (Lastow and Balachandran, 2007) therefore is not a scalable method to generate large quantities microbubbles (Parhizkar et al., 2017).

### 2.4.3 Microfluidic devices

Microfluidic devices have established their versatility in various fields for effective microbubble generation. They provide exquisite control over various parameters such as the solution flow rate and gas pressure (Garstecki et al., 2005a).. The Reynolds number provides a means to determine whether flow through a pipe is laminar or turbulent, and is defined as the ratio between inertial and viscous forces:

$$Re = \frac{\rho \mathrm{v} \mathrm{L}}{\mu} \qquad (2.3)$$

Where ρ is the density $(kg/m^3)$, $v$ is the velocity along the cross section of the pipe/capillary $(m/s)$, μis the dynamic viscosity $(Ns/m^2)$ and $L$ is the characteristic length $(m)$ of the capillary. The numerator represents the inertial forces, and the denominator represents the viscous forces. The Reynolds number of the liquid phase was calculated as 45 for the constant liquid flow rate of $0.01\mu l/min$ for a solution viscosity of $1\ mPa\ s$. Fluids of lower velocities are used in microfluidic units, therefore the flow in micro-capillaries is often represented by low Reynolds numbers $(1 \leq Re < 100)$, based on pipe diameter and bulk velocity (Di Carlo, 2009, Thorsen et al., 2001, Garstecki et al., 2005a)), and thus the fluid streams in micro-channels are laminar and easy to control.

The dynamics of bubble formation has been studied extensively both theoretically and experimentally by various researchers (Pancholi et al., 2008a, Stride and Edirisinghe, 2008, Qian and Lawal, 2006). This process occurs at the junction orifice where the column of gas impinges upon the continuous liquid stream. This results in the formation of an instability at the liquid-gas interface, and consequently the bubbles are formed by a 'pinch-off' process.

Various factors affecting the size and uniformity of the microbubbles include the size of the orifice, viscosity of the immiscible phases, use of surfactants, physical characteristics of the channels and the flow-rates of the liquid and gas (Teh et al., 2008, Lee et al., 2010).

The microfluidic devices used to prepare microbubbles are categorised into three main categories:

(1) Co-flowing

(2) Flow-focusing

(3) Cross flowing

These are shown in figure 11. These techniques rely on the flow field near the 'pinch off' region to promote the generation of the bubbles. In these

techniques, two fluid media are introduced into the system via a pressure driven flow.

The varying geometry associated with each technique determines the flow field, which initiates the formation of the bubbles. The competition between the fluid stresses acting at the liquid interface and the capillary pressure resisting this action causes the emerging droplet to detach from the fluid stream. This section details the various geometries employed in microfluidic arrangements.

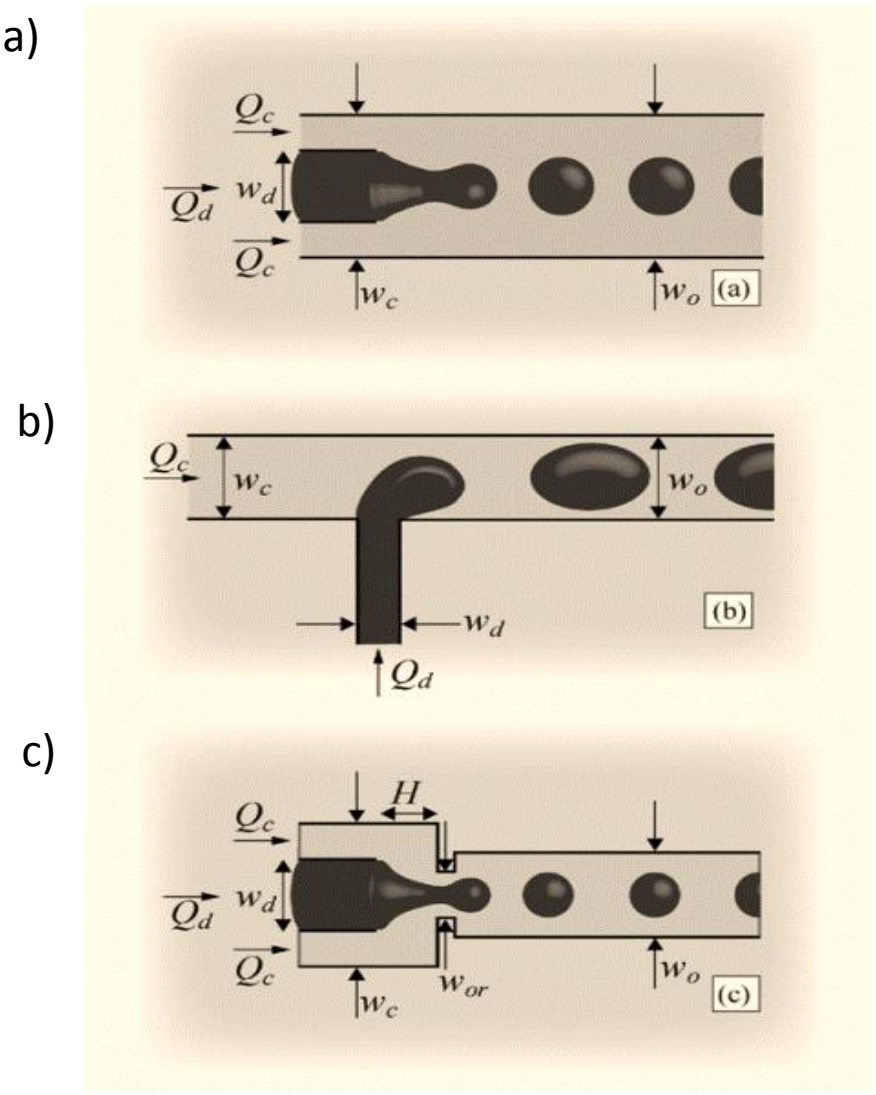


*Figure 11: Illustrations of the three main microfluidic geometries used for droplet formation. (a) Co-flowing streams, (b) cross- flowing streams in a T-shaped junction, and (c) elongational flow in a flow focusing geometry. In each case the widths of the inlet and inlet and outlet streams are indicated. It is assumed that the device is planar with a uniform depth h (Christopher and Anna, 2007).*

#### 2.4.3.1 Co-flowing devices

The co-flowing geometry is one of the ways to generate microbubbles as shown in in figure 11a. Droplets are generated by introducing the dispersed phase via a capillary or needle into the co-flowing continuous fluid phase (Cramer et al., 2004). As the dispersed phase enters the system, there are two main droplet formation mechanisms observed: (a) the droplets are formed directly at the tip of the needle (dripping regime) or (b) further from the main channel and from an extended stream as a result of Rayleigh instabilities (Zhao and Middelberg, 2011). Competition between the high shear force generated at the leading edge of the droplet and surface tension contribute to the generation of the droplets (Hong and Wang, 2007).

#### 2.4.3.2 Flow focusing devices

Flow focusing units have been investigated extensively to generate emulsions in the micro and nanoscale (Anna et al., 2003). These units are prepared using soft lithography (Anna et al., 2003, Garstecki et al., 2004) on hydrophobic polymer blocks such as Polydimethylosiloxane(PDMS)(Garstecki et al., 2004). In this microfluidic configuration, a liquid flows into the central channel and a second liquid enters the system via two external channels (figure 11c). These liquid phases are then forced to flow through a narrow orifice located further downstream to the three inlet channels (Anna et al., 2003). The outer fluid media exerts a force on the primary liquid resulting in the narrowing of the fluid stream (Baroud et al., 2010) referred to as the 'squeezing regime' by Garstecki et al. (Garstecki et al., 2005b). As the fluid stream further narrows, the enlarging droplet becomes stable as a result of the Rayleigh plateau instability, and finally breaks off as a result of inertia and surface tension. The flow focusing method confines droplets to the centre of the channel, thus preventing damage to the droplets formed as a result of shear stresses or wetting at the capillary walls (Takeuchi et al., 2005).

### 2.4.3.3 T-junction devices

Amongst the different microfluidic devices investigated in literature; the T-Junction device has been widely investigated due to the exquisite control it offers over processing parameters such as the solution flow rate and gas pressure which govern the dynamics of droplet formation and detachment in the junction. (Parhizkar et al., 2014, Parhizkar et al., 2013, Xu et al., 2006, Garstecki et al., 2006, Wang et al., 2011). The formation of bubbles using this geometry is distinguishably different in comparison to co-flowing and flow-focusing microfluidic systems.

The inlets that introduce the dispersed fluid media are arranged perpendicularly to the main channel (figure 11b). When the dispersed fluid media enters the junction, the bubble begins to grow and obstructs the flow of the continuous fluid. This results in an increase in dynamic pressure upstream, forcing the emerging bubble to pinch-off as the viscous shear stress overcomes the interfacial tension. However, this device is flawed by the poor production rate and bubble size variation without an external force especially when viscous solutions are used.

### 2.4.3.4 Y-Junction and V-junction devices

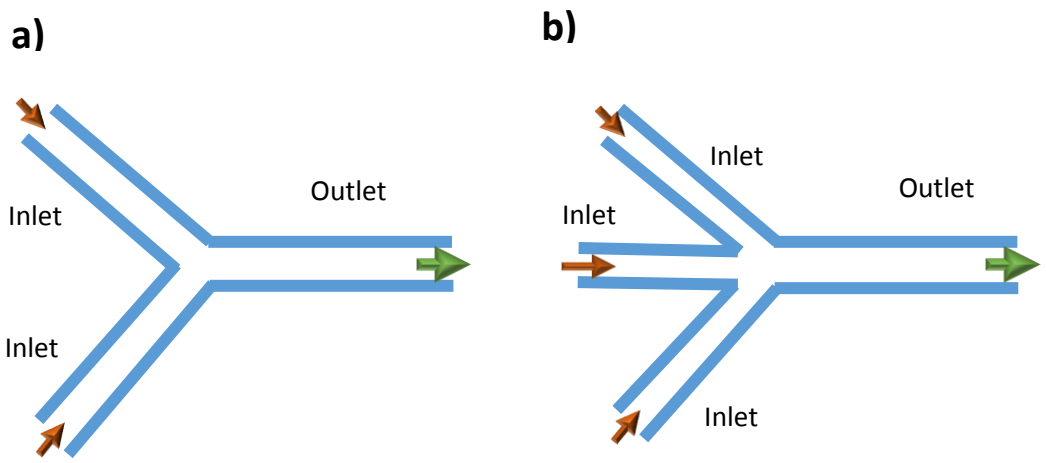


*Figure 12: Schematic of a) Y-Junction microfluidic device b) V junction microfluidic device.*

Alternative configurations of microfluidic devices include Y- and V- Junction devices as shown in figure 12. In the Y-junction device(figure 12a), the angle between the two inlet channels is usually higher than $90^{\circ}$ (Ushikubo et al., 2015), which influences the droplet generation as a result of the shear imposed by the continuous phase on the dispersed one.

The droplet detachment process in a Y-junction is described as a single-step process, when the dispersed phases moves along one of the inlet channels, the angular arrangement of inlets facilitate the detachment of the droplet as it enters the outlet channel (Steegmans et al., 2009), due to the competition between shear and interfacial forces. Ushikubo et al. (Ushikubo et al., 2015) reported that this device has the potential to develop novel food structures by encapsulation for controlled release. Single and multiple emulsions, emulsion-template microparticles and self-assembled nanoparticles with low size polydispersity can be generated to load hydrophilic and/or hydrophobic compounds.

The V-junction device (figure 12b) has also gained considerable attention for their feasibility in drug delivery applications (Kucuk et al., 2014, Gunduz et al., 2013). It enables the use of 3 fluids, hence the potential to encapsulate multiple agents within a single microbubble. Gunduz et al. (Gunduz et al., 2013) employed the V-junction device to prepare ethyl cellulose drug delivery carriers. The microbubbles generated composed of an ethyl cellulose shell and the drug. As the solvent evaporates, the ethyl cellulose is precipitated in the form of particles at the bubble surface, thus encapsulating the drug and forming an ethyl cellulose nanocapsule. Similar to this study, Kucuk et al. (Kucuk et al., 2014) were able produce polymethylsilsesquioxane (PMSQ) nanospheres using the aforementioned device. They recorded a high drug loading efficiency of 13% with certain solution formulations, demonstrating its potential in drug delivery applications.

## 2.5 Mechanism of bubble formation in microfluidic devices

Various studies have been conducted in order to establish a better understanding of bubble and droplet formation within microfluidic devices (Thorsen et al., 2001, Taylor, 1934, Garstecki et al., 2006, De Menech et al., 2008). The very first experiments using two phase microfluidic systems were conducted by Thorsen et al. (Thorsen et al., 2001) where the droplet dynamics for a classic oil-in-water system was discussed. The discontinuous phase (water) blocks the continuous stream (oil), causing an increase in shear forces at the leading edge of the emerging water droplet. The flow is described to be non-linear because the boundary is not static. This is because the movement of one fluid will consequently affect the other. This results in the formation of an instability, which facilitates the formation of droplets, owing to the competition between surface tension and shear forces which was detailed in depth in the work of Taylor (Taylor, 1934). Their work reports that the movement of a secondary fluid causes the distortion of a droplet due to the presence of tangential viscous and dynamical forces acting on the droplet surface, the surface tension retains the spherical shape of the emerging droplet.

## 2.6 Types of flow in microfluidic devices

Numerous actuation methods have been employed to pump or regulate fluids within microchannels, in order to ensure optimal throughput and performance of the system. They are classified into two main categories – pressure driven and electrokinetically driven flows (Mitchell, 2001). Flow into microchannels is commonly achieved by means of a pressure gradient, introduced by mechanical pumps (Chakraborty et al., 2012). An alternative approach to control the fluid flow is by the application of an electric potential known as electroosmotic flow (David et al., 1999, Xiangchun and Dongqing, 2004).

The two most commonly investigated types of electrokinetic flows are electrophoresis and electroosmosis. In the prior, the ionised particles move relative to the stationary liquid by the application of an electric potential ($>$ $100\,V/cm$). Whereas in latter, the ionised liquid flows relative to the stationary charged channel surface by the application of an electric potential.

External fields have been extensively employed to manipulate microfluidic flows including pressure, electric, magnetic and capillary forces(Stone et al., 2004). As channel dimensions are reduced, the importance of surface to volume forces increases. Manipulating the flow in this manner can be achieved macroscopically by applying the force at the appropriate inlet or outlet, or the force can be generated within the channel by incorporating integrated components.

The presence of a gas-liquid interface or liquid-liquid interface allows fluid motion to be generated by controlling the variations of surface tension (known as the Marangoni stresses) (Baroud et al., 2010). Surface tension variations can be generated with chemical, thermal, electrical or light gradients. It is also feasible to actuate liquid/gas or liquid/liquid menisci in channels with partially wetting surfaces by capitalising on capillary pressure gradients. The Young-Laplace law states that the latter can be induced by modifying the wetting properties such as the contact angle or surface tension, or the geometric features such as the channel diameter.

External fields can be used to promote the movement of particles suspended in the fluid. For example, magnetic fields can be used to manipulate the flow of fluids containing dispersed magnetic particles, and sound fields can generate acoustic streaming motions. Physical features of the channels can also be modified in terms of geometry, chemical and mechanical properties to enable further control over fluid motion. The rheology of the fluid is also important, therefore Newtonian and non-Newtonian fluids need consideration. The optimal protocol on how to mix, react, detect, analyse and separate in microflows can be attained by a unique combination of the driving forces and surface characteristics.

The following section provides an overview of pressure driven and electroosmotic flows within microchannels.

### 2.6.1 Pressure driven flows

Pressure driven flows have been preferably used in microfluidic arrangements due to the relatively easy implementation and their insensitivity to surface contamination, ionic strength and pH (Kamholz and Yager, 2001, Dutta et al., 2006). Although the production rate is quite low, this method enables the potential of parallel production (Link et al., 2004). The velocity profiles generated by this type flow conform to the Poiseuille flow theory, and the fluid velocity at the walls is zero known as the no-slip boundary condition (Lauga et al., 2006). However, this sort of velocity profile leads to hydrodynamic dispersion effects which can be undesirable in many separation applications (Author, 2008).

The most common way to drive microfluidic flow by pressure is by connecting a syringe pump to the capillary tubing. Regulating the in-flow of fluids into the microfluidic system using this method is straight forward however, it is bulky and not a feasible option for miniaturisation which is fundamental in lab-on-chip technologies.

A broader range of materials can be actuated using this method as it is not affected by factors such as surface contamination.

### 2.6.2 Electroosmotic flows

Electroosmotic actuation is another technique that has been widely deployed to control the flow of fluids in microchannels. The fluid flow can be controlled by applying a tangential electric potential simultaneously at various locations (Pak Kin et al., 2004). This causes a double layer of ions known as the electrical double layer (EDL) or Debye layer (Kirby and Hasselbrink, 2004) to form along the polarised walls. The ions that form the double layer are forced to move along the capillary, dragging the carrier fluid

along with it via viscous forces toward the electrode of opposite polarity, the net flow that is generated is referred to as electroosomotic flow (EOF) (Gaudioso and Craighead, 2002, Ross et al., 2001) with a uniform velocity profile. The electroosmotic velocity is given by:

$$v_{EOF} = \frac{\varepsilon \zeta E}{4\pi\eta} \qquad (2.4)$$

Where ε is the dielectric constant of the fluid, $\eta$ is the fluid viscosity, $E$ is the applied electric field strength and $\zeta$ is the Zeta potential of the surface. The ζ- potential is defined as the difference in electrostatic potential between the bulk solution and the fluid-solid interface(Tandon et al., 2008). EOF reduces the broadening of the plugs or hydrodynamic dispersion which is predominantly experienced in pressure driven flows (Tang et al., 2006), and due to the small cross-sectional area of the microchannels, large potential differences can be maintained with low currents. Cho et al. (Cho et al., 2002) developed an experimental configuration using an electrowetting on dielectric (EWOD) microfluidic actuation to achieve the four main droplet manipulation mechanisms – (1) creating, (2) transporting, (3) cutting and (4) merging of the droplets utilising relatively lower voltages which were effectively confined to the junction capillaries.

A major advantage that electrokinetic flows offer over pressure-driven flows is the uniform velocity profile, as a uniform charge distribution is applied on the microchannel walls (Bayraktar and Pidugu, 2006). They also enable easy control over the flow in interconnected or branched channels by simply switching the voltages, hence do not require valves. One of the drawbacks of electrokinetic flow is that this type of flow is limited to polar solvents.

Electrically driven microfluidic devices have been extensively explored by various researchers to prepare fibres, droplets and microbubbles (Srivastava et al., 2008, Kim et al., 2007). Srivastava and colleagues (Srivastava et al., 2008) reported a method to prepare hollow and core/sheath nanofibers.

The 8 outlet spinnerets are fitted with stainless steel tubes to provide a conductive surface and scalability in terms of fibre production. A voltage of $\sim 15\ kV$ was applied to the steel tube that connects the syringe output to the inlet capillary, which generated dense and uniform fibrous mats.

Kim and co-workers (Kim et al., 2007) presented a microfluidic flow focusing configuration to generate emulsion droplets using an electric field. They inserted the source and ground electrodes in the polydimethylsiloxane (PDMS) microfluidic chip, which results in the polarisation of the solid-liquid interface at the exit of the capillary, which finally breaks into a stream of fine droplets as a result of the Rayleigh instability.

More recently, researchers have explored combining T-junction microfluidic devices with electrohydrodynamics (Pancholi et al., 2008b, Parhizkar et al., 2014). Pancholi et al. (Pancholi et al., 2008b) utilised a T-junction fabricated from two fused silica capillaries with internal diameters of $50\ \mu m$, and a stainless steel outlet capillary with an internal diameter of $500\ \mu m$. Using this configuration, they were able achieve microbubbles down to $\sim 5\ \mu m$ at a voltage of $\sim 18\ kV$. However, the limitation of this research was the large size distribution of microbubbles formed. Parhizkar et al. (Parhizkar et al., 2014) adapted a similar configuration, but instead of fused silica capillaries, two coarser detachable Fluorinated Ethylene Polypropylene(FEP) and a stainless steel outlet capillary with inner diameters of $100\ \mu m$, where a potential difference was applied. Their method yielded monodisperse microbubbles with a polydispersity index of $\sim 1\%$, however increasing the voltage beyond $12\ kV$ did not alter the microbubble diameter any further.

The T-junction microfluidic device is a simple and economic method to prepare monodisperse microbubbles. However, this configuration experiences limitations in terms of achieving microbubble diameters smaller than the channel dimensions due to constraints on capillary size especially using highly viscous solutions and the relatively low rate of production in comparison with techniques such as sonication. From the material reviewed above, it has been demonstrated that electric fields can be used to manipulate the hydrodynamics of liquids in microchannels which present

high electrical resistance to ionic currents, therefore high voltages can be maintained at low currents as detailed by Stone et al. (Stone et al., 2004).

## 2.7 Scaling models associated with bubble break-up and size prediction in T-junction devices

Over the years, various scaling models have been developed to predict the size of bubbles, although a consensus regarding the most accurate model has not been reached. Thorsen et al. (Thorsen et al., 2001) developed a model that postulated that droplet formation occurs as a result of high shear forces at the leading edge of the droplet competing with the interfacial forces. Conversely, Garstecki et al. (Garstecki et al., 2006) argued that interfacial forces dominate shear forces at lower Capillary numbers and the dynamics of bubble detachment is dominated by the pressure drop across the bubble as it forms. The capillary number is a dimensionless quantity, defined as the ratio between the viscous forces and interfacial forces acting across an interface between a liquid and gas, or between two immiscible liquids (Seebergh and Berg, 1992), and is given by:

$$Ca = \frac{\mu_l v_l}{\gamma} \tag{2.5}$$

Where $\mu_l$ is the dynamic viscosity of the liquid $(m\,Pas)$, $v_l$ is the velocity$(m/s)$ and $\gamma$ is the interfacial tension $(Nm^{-1})$ between the two fluid phases. They emphasised that the size of the bubble is governed by the volumetric flow ratios of the two liquids and referred to this as the 'squeezing regime'. The pressure within the bubble is given by the Young-Laplace equation (Walker and Beebe, 2002).

$$\Delta P = \gamma \left( \frac{1}{R_1} + \frac{1}{R_2} \right) \tag{2.6}$$

Where $R_1$ and $R_2$ denote the principal radii of curvature in the axial and radial directions. The scaling model developed by the aforementioned authors taking to account of the break-up mechanism and the resultant slug size is expressed by equation 2.7.

$$L = w + \varepsilon\left(\frac{Q_g}{Q_l}\right) \tag{2.7}$$

Where $L$ represents the length of the slug, w denotes the width of the channel, $(Q_g/Q_l)$ is the ratio of the flow rates of the gas and liquid phases respectively, and finally $\varepsilon$ is the characteristic width of the slug, which depends on the geometric width of the microchannel. The inflow of the gas phase $(Q_g)$ is given by the following expression:

$$Q_g = \left(\frac{P_i - P_o}{R_F}\right) \tag{2.8}$$

Where $P_i$ and $P_o$ denote the difference in pressures at the gas inlet and the outlet respectively, $R_F$ is the resistance to flow in the channel, and assuming it scales in the same way as a channel filled with the continuous liquid medium, it can be expressed by equation 2.9.

$$R_F = \frac{\mu L_{ch}}{h^2 w^2} \tag{2.9}$$

where $L_{ch}$, is the length of the channel. De Menech et al. (De Menech et al., 2008) correlated the two models described above and identified that past a critical value of the capillary number, the system enters the 'dripping regime' which is shear dominated droplet formation. They asserted that as the capillary number increases, the droplet formation is characterised by long threads of the fluid stream prior to the enlargement of the droplet that is

referred to as the 'jetting regime', which is associated with inertial forces of the continuous stream. It was identified that when $Ca < 0.015$, the squeezing regime occurs and the dripping regime occurs at capillary numbers above the aforementioned value.

Although much attention has been given to the process of bubble formation and break-up; the dynamics of the emerging slug between the upper and lower limits $(0.01 < Ca < 0.02)$ has been neglected. Xu et al. (Xu et al., 2008) indicated that the droplets produced during this transitional regime were by both squeezing and dripping processes. They developed a model that predicts the plug length under both mechanisms:

$$L = w + \varepsilon \left(\frac{Q_g}{Q_l}\right)^{\alpha} \left(\frac{1}{Ca_c}\right)^{\beta} \qquad (2.10)$$

Where $Ca_c$ is the capillary number of the continuous phase and $\alpha$ and $\beta$ are the ratios of the previously described mechanisms respectively. Van Steijn and colleagues (van Steijn et al., 2010) observed that changing the geometric configuration from circular to rectangular presents varied results which also need to be considered in order to formulate and accurate scaling model. Upon substituting a circular cross section with a rectangular one resulted in the formation of longer bubbles and slugs as there is substantial leakage of the continuous phase into the corners of the channels known as 'gutters,' resulting to a drop in velocity at which the liquid is squeezed. This suggests that the geometric configuration of the channels greatly influences bubble dynamics.

### 2.7.1 Influence of geometry on bubble formation

The influence of geometry on bubble formation was presented by Gupta et al. (Gupta and Kumar, 2010). In their simulations, they noticed that

decreasing the height to width ratio of their model resulted in the reduction plug/bubble length. They argued that the work conducted by Garstecki et al.(Garstecki et al., 2006) did not account for the channel depth, which led these authors to suggest that two channel geometries of the same widths and flow ratios form bubbles of the same dimensions. Liu et al. (Liu and Zhang, 2011) developed a dimensionless parameter to express the ratio between the inlet widths of the two phases.

$$\Lambda = \frac{w_c}{w_d} \tag{2.11}$$

Where $w_c$ and $w_d$ denote the inlet widths of the continuous and dispersed phases respectively. An increase in $\Lambda$ resulted in a consequent increase in the volume of plugs, and the pinch off process moves further downstream of the junction. The channel geometry influences the bubble dynamics as the squeezing pressure becomes significant when the emerging slug obstructs the main channel.

Fei et al. (Fei et al., 2008) investigated the effects of converging, diverging and straight channels. They recorded that as the channel size converges, the bubble length increases due to the compression of the bubble. The bubble flow is restricted due to an increase in upstream capillary force, the opposite effect is observed in diverging channels.

One of the greatest advantages of mechanically assembled units is that the geometry can be selected based on the application that is being targeted, and the composition of the bubble that is necessary for the specified application. Gunduz et al. (Gunduz et al., 2013) generated drug delivery nanocarriers using a V-junction device, which is composed of three inlets and a single outlet. Using this geometry, it is possible to generate nanocarriers which contain active pharmaceutical ingredients, and by studying the release dynamics of the encapsulated drug they were able to

concur that the bubbles produced have tremendous potential for sustained drug delivery.

### 2.7.2 Influence of flow properties on bubble formation

Multiphase flows occur when two or more immiscible streams interact resulting in the formation of suspended droplets, channel spanning slugs and wall wetting films depending on interactions between interfacial, inertial and viscous forces (Günther and Jensen, 2006). The presence of interfacial forces combined with the laminar nature of flows at low Reynolds numbers form very regularly shaped liquid-gas plugs.

Keeping the flow rate of the dispersed phase constant, increasing the flow rate of the continuous phase $(Q_c)$ results in a linear decrease the bubble diameter (Nisisako et al., 2002) and a consequent increase in the production rate due to lower continuous shear forces acting at the continuous/dispersed phase interface. In shear-droplet forming processes (perpendicular shear droplet break-up), the droplet length is only influenced by the ratio between the continuous and dispersed phases $(Q_c/Q_d)$ but is independent of the total flow rate.

On the other hand, using cross-flowing rupture technique, the relative length of the plugs was lower due to the dominating shear forces. In the perpendicular shear droplet break-up process, the wall effects and interfacial tension influence the formation of bubbles.

## 2.8 Microfluidic device material and fabrication methods

Fabrication methods to generate robust microfluidic technologies have been an area of paramount interest over the past decade (Hutchison et al., 2004). Commonly used materials for their construction are silicon and glass, which allow batch processing and have desirable polarised surfaces which support

electroosmotic flow (Anderson et al., 2000). However, these processes are expensive and require clean room conditions.

For this reason, alternative materials have been considered such as poly(dimethylsiloxane) (PDMS), poly(methylmethacrylate) (PMMA) and poly(ethylene terephthalate)(PET) (Becker and Locascio, 2002). As opposed to silicon and glass, the aforementioned polymers are economical and their assembly is not cumbersome.

The drawback of devising microfluidic chips using polymers is that they are usually incompatible with organic solutes and not resistant to high temperatures. Injection moulding, imprinting or soft embossing, soft lithography and laser ablation are some of the fabrication techniques explored in the literature by various research groups over the years (De Mello, 2002, Narasimhan and Papautsky, 2003, Unger et al., 2000, Xia and Whitesides, 1998, Qin et al., 2010, Kim et al., 2005, Pugmire et al., 2002).

### 2.8.1 Injection moulding

With injection moulding, the appropriate polymer is melted and injected into an evacuated cavity containing predefined mould at a high pressure, the cavity is maintained at the melting point of the polymer in order ensure that the melted polymer evenly coats the entire mould (De Mello, 2002). Finally, the cavity is cooled and the device is ejected and typically used for electrophoretic applications.

### 2.8.2 Imprinting/hot embossing

This technique enables the creation of microstructures on the surface by placing wires of a specific diameter on a substrate and heating them slightly below the glass transition temperature $(T_g)$ of the substrate (Narasimhan and Papautsky, 2003). The assembly is then cooled to below the $(T_g)$ before the wires are removed forming microchannels of $\sim 10\ \mu m$. Although this process cannot be completely automated, it enables replication of

microstructures on substrates having different glass transition temperatures.

### 2.8.3 Soft lithography

This is a widely used fabrication technique to generate microchannels on a polymeric substrate, where a particular polymer and curing agent are decanted into a micromachined template/mould (Unger et al., 2000, Xia and Whitesides, 1998). After the curing process, the polymer is peeled away and can be enclosed thus forming a microfluidic device. Soft lithography also provides a basis for nanofabrication where the process can generate structures on a substrate smaller than $\sim 100\ nm$ (Qin et al., 2010).

### 2.8.4 Laser ablation

Laser ablation involves using high power laser pulses as a micromachining tool to generate patterns on a substrate to micrometre precision(Kim et al., 2005). These pulses result in the destruction or ablation of the polymer enabling the formation of a network of channels along the surface of the substrate. An added advantage of laser ablation is that the surface properties of the substrate can be modified, which can influence the overall functionality of the device(Pugmire et al., 2002).

## 2.9 Summary of literature

A detailed survey of the literature was presented in this section, and the summary of the pertinent points are listed below:

- The first section provided a detailed overview of microbubbles in various industries. They are incorporated in food products to improve their visual appeal as well enhance the texture of perishables. Microbubbles are also used in wastewater treatment to

filter biogases and in biosensors to detect bacteria such as E-coli. Due to the high surface area of microbubbles.

- The preparation techniques to generate microbubbles were reviewed. Microfluidic devices were observed to be a robust technique to prepare uniform microbubbles/droplets due to the excellent control they provide over the processing

- The different geometrical configurations of microfluidic devices were explored and the hydrodynamics in the microchannel were discussed, with emphasis on pressure driven and electroosmotic flows. The various scaling models for their formation, break-up and size prediction proposed by various authors were presented.

- Finally, the methods of manufacturing microfluidic devices such as injection moulding, imprinting/hot embossing, soft lithography and laser ablation were discussed.

Based on the literature reviewed, The T-junction microfluidic device is a simple yet economic method to prepare monodisperse microbubbles for a plethora of applications. However, this configuration experiences limitations in terms of achieving microbubble diameters smaller than the channel diameters especially when course capillaries are used.. DC electric fields have been introduced to microfluidic units, however requiring the use of very high voltages to vary the microbubble diameter. Microbubble sizes ceased to reduce beyond a particular voltage, thus necessitating alternative stress fields to achieve better control over the process. The experimental set-up developed and presented in this thesis aims to alleviate the problems experienced in previously described set-ups by introducing new variables to achieve further control over the microbubble size. The novel apparatus will be presented in chapter 4, after the numerical methods required to generate the 2D model of the T-Junction is discussed.

# Chapter 3

# Numerical Methods

## 3.1 Introduction

This chapter discusses the governing equations in microfluidics, formulated in terms of the continuum field description of velocity, pressure, density electrical field. The electrical stresses as a result of the electric filed applied at the nozzle are studied by analysis of the Maxwell's equations. The 2D simulations of the T-junction conducted were based on the finite volume method (FVM) using a structured mesh to discretise the governing equations. An overview of the volume of fluid (VOF) method to simulate the bubble formation and break up is presented. Moreover, to highlight the accuracy of the numerical model, an overview of the first and second order discretisation schemes is presented and a theoretical description of the underlying solvers i.e. the Algebraic Multigrid (AMG) and the Conjugate Gradient Scheme (CGS), important in the iterative solution to the problem, are offered.

## 3.2 Governing equations

### 3.2.1 Modelling the hydrodynamics

The simulation of hydrodynamic fluid flow using computational fluid dynamics (CFD) tools is based on the iterative solution of a discretised set of equations which comprise the conservation principals of mass, momentum and energy expressed by the Navier-Stokes equations (NSE). Given that we are dealing with isothermal flows, the energy equation is not needed.

$$\nabla . \boldsymbol{u} = 0 \tag{3.1}$$

$$\rho\left(\frac{du}{dt} + u \cdot \nabla u\right) = -\nabla p + \nabla \cdot \left(\mu(\nabla u + \nabla u^T)\right) + F^s + F^{el} \tag{3.2}$$

In equations 3.1-3.2, $\boldsymbol{u}$ is the fluid velocity, $p$ is the fluid pressure, $\rho$ is the fluid density and $\mu$ is the dynamic viscosity of the fluid. $F^s$ and $F^{el}$ are the surface tension and electric tensors respectively. The averaged values of the density and viscosity are calculated using the volume fraction:

$$\rho = \alpha\rho_1 + (1-\alpha)\rho_2 \tag{3.3}$$
$$\mu = \alpha\mu_1 + (1-\alpha)\mu_2$$

Where $\alpha$ represents the volume fraction which indicates the two-phase interphase position which is updated followed by the calculation of the surface tension. The surface tension is based on the Young-Laplace equation, and is expressed by equation 3.4 in terms of the surface curvature (Chen et al.):

$$F^s = \sigma k \check{n} \tag{3.4}$$

Where $k$ is the surface curvature, $\sigma$ is the surface tension coefficient and $\check{n}$ is the surface normal. The Continuum Surface Force (CSF) model developed by Brackbill et al.(Brackbill et al., 1992) has been integrated in various commercial codes available(Meier et al., 2002), it converts the interfacial surface into a volume force such that it can be added as a source term in the NSE as shown in eq. 3.2. The surface tension force is implemented by the piecewise-linear interface calculation (PLIC) scheme, which enables the

accurate calculation of the curvature of the droplets that are formed for reconstruction of the interface front (Sontti and Atta, 2017).

### 3.2.2 Modelling the electrohydrodynamics

The presence of an electric field in the flow problem necessitates the simultaneous solution of charge e/field equations, i.e. the Maxwell equations. The capability to solve for this type of physics, in a discretised manner and in a mode that is fully to the hydrodynamics, is offered by the software suite used in this study (CFD-ACE+, ESI Group, Paris, France) This enables the calculation of various electrical quantities based on a truncated[1] version of the Maxwell's equations (Rahmanpour and Ebrahimi, 2016). Electrohydrodynamic configurations such as electrospraying and electrohydrodynamic atomisation utilise high voltages but lower applied currents (Hohman et al., 2001, Alexander et al., 2006, Kim et al., 2011) to achieve the desired regimes. When an electric potential is applied at the nozzle, a tangential electric force is experienced at the gas-liquid interface, consequently, an electric charge builds up and begins to accumulate at the gas-liquid interface such that it behaves like a capacitor. The current values are very small and occur over a relatively long time scale (Ernst et al., 2012), in light of this, it is adequate to solely consider the electrohydrodynamic effects within the electrostatics limits where electromagnetic effects are neglected. The electric momentum is defined by the Maxwell's stress tensor (Lastow and Balachandran, 2007).

$$F^{el} = q\vec{E} - \frac{1}{2}\vec{E}\cdot\vec{E}\nabla\varepsilon + \frac{1}{2}\nabla\left(\rho\frac{\delta\varepsilon}{\delta\rho_T}\vec{E}^2\right) \qquad (3.5)$$

Where q represents the volume charge density at the interface, $\vec{E}$ is the

[1] Due to the assumption of absence of the magnetic component in the electromagnetic fields.

electric field vector and ε is the relative permittivity of the fluid. The first term in equation 3.5 embodies the coulombic force, which occurs as a result of the interaction between the charged interface and the electric field. The second and third terms embody the polarisation forces and are referred to as the dielectric and the electrostrictive forces respectively. The electrostrictive force can be neglected in this case, due to the incompressible nature of the fluids used in this work. Therefore, equation 3.5 can be further simplified as:

$$F^{el} = q\vec{E} - \frac{1}{2}\vec{E} \cdot \vec{E}\nabla\varepsilon \qquad (3.6)$$

In order to obtain the Maxwell stress terms, the governing equations for the electric field need to be resolved. Based on Gauss's Law, applying an electric potential generates an electric field, this law asserts that the flux of that field passing through any closed surface is proportional to the total charge contained within that surface (Fleisch, 2008) and can be expressed in differential form as shown below:

$$\nabla \cdot D = q \qquad (3.7)$$

Where $D$ is the electric displacement flux density $(C/m^2)$. The Electric flux density $D$ can be correlated with the electric field $E$ by the following expression:

$$D = \varepsilon \cdot E \qquad (3.8)$$

Where the electric permittivity can be expanded by the following (Liu, 2010):

$$\varepsilon = \varepsilon_r \varepsilon_0 \tag{3.9}$$

Where $\varepsilon_r$ is the dielectric constant and $\varepsilon_0$ is the permittivity of vacuum. The electric field vector $E$ is described to be non-rotational i.e. $\nabla \mathrm{x}\, E = 0$, therefore a scalar electric potential $\Psi$ can be defined by the following expression:

$$E = -\nabla\Psi \tag{3.10}$$

Substituting equations 3.8 and 3.10 into equation 3.7, we deduce the Poisson's equation for the electric potential denoted by equation 3.11.

$$\nabla \cdot (\varepsilon_r \varepsilon_0 \cdot \nabla\Psi) = -q \tag{3.11}$$

Using equation 3.11, the electric potential distribution within the system under different electric fields can be elucidated. Lima et al (Lima and d'Ávila, 2014) added that the characteristic time for electrostatic processes is large in contrast to magnetic phenomenon, therefore the aforementioned electrostatic equations sufficiently describe an electrohydrodynamic system.

## 3.3 The Finite Volume Method (FVM)

The finite volume method (FVM) is a popular scheme to discretise the incompressible mass and momentum equations. Other well-known discretisation include the finite-element method (FEM) and finite difference method (FDM) (Glockner and Naterer, 2006). The FVM is robust, flexible and enables the solution to flow problems with complex geometrical

configurations(Feistauer, 2007). This is a fundamental step as it transforms the various partial differential equations (PDEs) specified as the governing equations into discrete algebraic equations.

This method divides the solution domain into a discrete number of control volumes (CV), such that there is one control volume surrounding each grid point as shown in figure 13a-b. These CV are generated for discretisation by means of a computational mesh. The grid points are positioned in the middle of the CV, i.e. all the dependent variables and material properties are stored at the cell centre (figure 13a) therefore the average value of any quantity within a CV is given by its corresponding value in the centre of the cell.

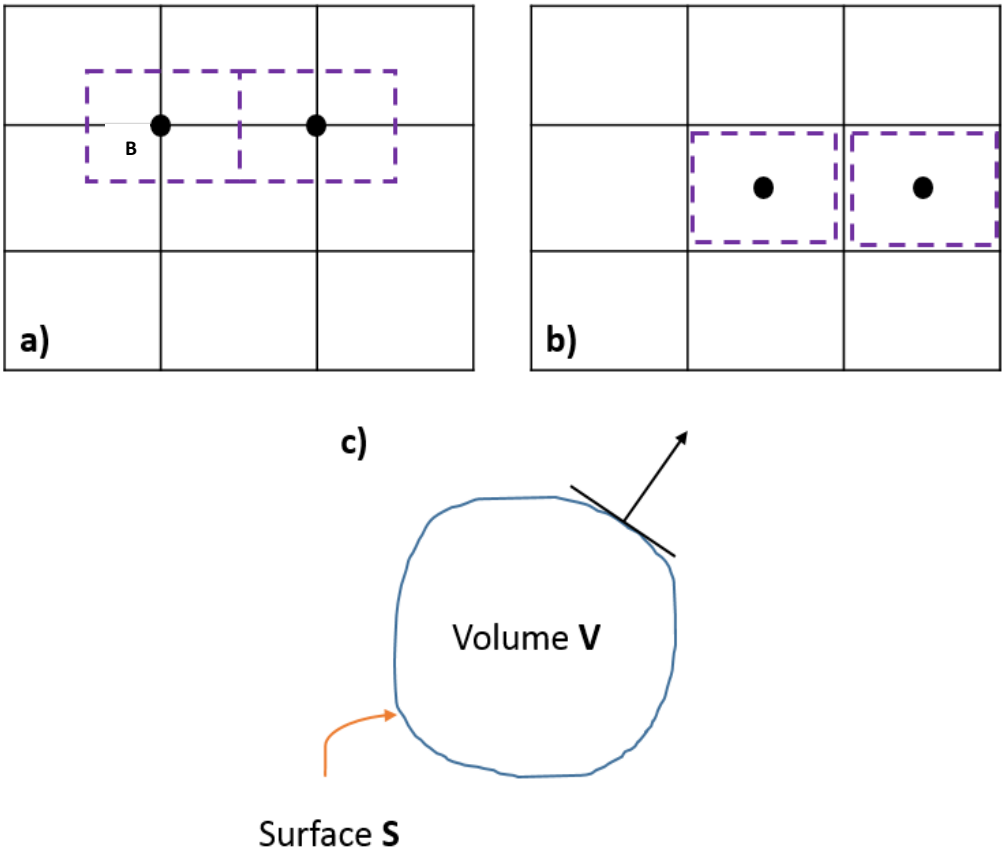


*Figure 13: a) The computational node (where the variable is stored) is located at the intersection of the two grid lines, the boundaries of the control volume are located midway between adjacent nodes b) An alternative arrangement of the nodes is on the centroid of the control volume c) General volume V and surface S, which bounds V.*

The general transport equation for quantity ($\varphi$) is expanded in as shown below.

$$\underbrace{\frac{\partial(\rho\varphi)}{\partial T}}_{\text{Transient}} + \underbrace{\nabla\cdot\left(\rho\,\vec{V}\,\varphi\right)}_{\text{Convection}} = \underbrace{\nabla\cdot(\Gamma\nabla\varphi)}_{\text{Diffusion}} + \underbrace{S_{\varphi}}_{\text{Source}} \qquad (3.13)$$

The integration of the generic transport equation 3.13 on each CV is based on Green's theorem to convert volume integrals containing a divergence term into surface integrals. These terms are subsequently evaluated as fluxes at the surface of each cell in the computational domain. Let **n** be unit normal vector on **S**, which is assumed to be positive when drawn outward with respect to the volume ***(V)*** enclosed by **S** (figure 13c). The general transport equation can be expanded and integrated over a control volume cell $\omega$:

$$\underbrace{\int_{\omega}\frac{\partial(\rho\varphi)}{\partial t}d\omega}_{\text{Transient}} + \underbrace{\int_{\omega}\nabla\cdot\left(\rho\vec{V}\varphi\right)d\omega}_{\text{Convection}} = \underbrace{\int_{\omega}\nabla\cdot(\Gamma\nabla\varphi)d\omega}_{\text{Diffusion}} + \underbrace{\int_{\omega}S_{\varphi}}_{\text{Source}} \qquad (3.14)$$

The rate-of-change and source terms are integrated over the cell volumes, whereas the convection and diffusion terms form the sum of fluxes through the CV faces. The evaluation of each of these terms is described in sections 3.4.1-3.4.4.

### 3.3.1 Integrating the transient term

The value of the dependent variable, which is located in the middle of the control volume (point B in figure 13a) represents an overall average of the control volume. Therefore, the rate of change term can be discretised as follows(Demirdžić and Perić, 1990)

$$\int_{\omega} \frac{\partial(\rho\varphi)}{\partial t}\partial\omega = \frac{\rho^{a}\varphi^{a}\omega^{a} - \rho^{a-1}\varphi^{a-1}\omega^{a-1}}{\partial t} \qquad (3.15)$$

The superscripts 'a' and 'a-1' represent the new and old time levels respectively,  is the time step and is the CV, which may be time dependent when moving grids are used.

### 3.3.2 Integrating the convection term

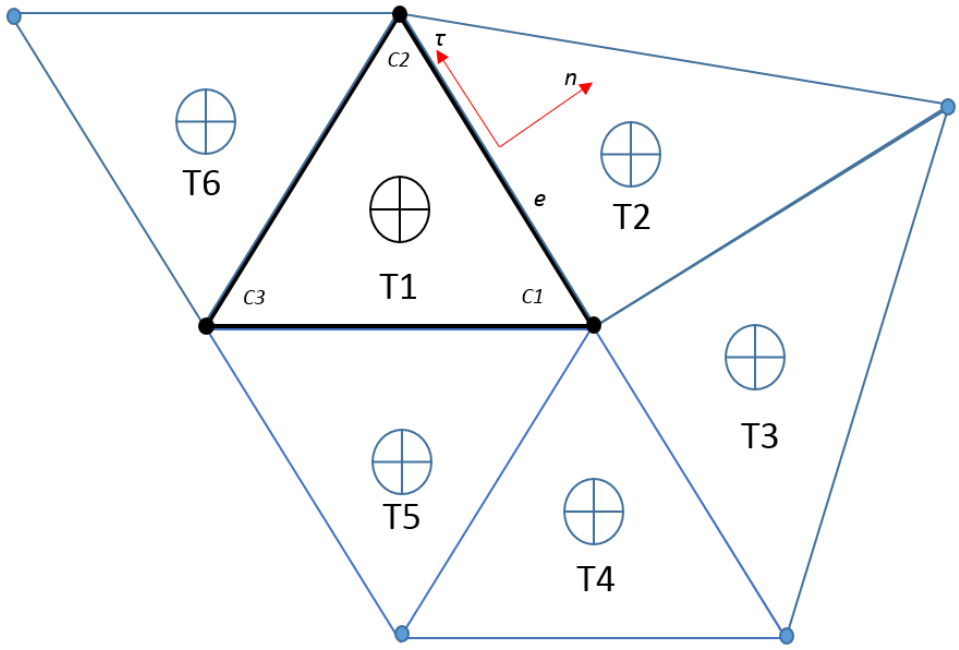


*Figure 14: Adjacent finite volumes (here 2D triangles T1-T6). The dependant variables and material properties are averaged over the cell volume and stored at the marked cell centre for interpolation.*

The convection term is a volume integral of a divergence term, therefore the convection term can be discretised as follows:

$$\int_{\omega} \nabla\cdot\left(\rho\vec{V}\varphi\right)d\omega = \oint \rho\varphi\vec{V}\cdot\vec{n}dA = \sum_{e}(\rho_{e}\varphi_{e}V_{e}^{n})A_{e} = \sum_{e} C_{e}\varphi_{e} \qquad (3.16)$$

In equation above, the subscript $e$ denotes the face of the current computational cell (figure 14). $A_e$ is the area of the face of the cell and $u_e^n$ is the velocity normal to the face. $C_e$ can be described as the flux through the face and its evaluation is dealt with in section 3.6 relating to pressure-volume coupling. The value at face $e$, $\varphi_e$, can be evaluated through a variety of interpolation schemes that provide varying levels of numerical stability and accuracy which are discussed in sections 3.6 and 3.7.

### 3.3.3 Integrating the diffusion term

The diffusion term is discretised in the following manner:

$$\int_\omega \nabla \cdot (\Gamma \nabla \varphi) d\omega = \int_A \Gamma \nabla \varphi \cdot \vec{n} dA = \sum_e \Gamma_e \left(\frac{\partial \omega}{\partial n}\right)_e A_e \qquad (3.17)$$

Where the unit vector in figure 14 is defined as:

$$\frac{\partial \varphi}{\partial n} = \frac{1}{\vec{n} \cdot \vec{e}} \left(\frac{\partial \varphi}{\partial e} - \vec{e} \cdot \vec{\tau} \frac{\partial \omega}{\partial \tau}\right) \qquad (3.18)$$

the diffusion term becomes:

$$\int_\omega \nabla \cdot (\Gamma \nabla \varphi) d\omega = \sum_e \frac{\Gamma_e}{\vec{n} \cdot \vec{e}} \left(\frac{\partial \varphi}{\partial e}\right)_e A_e - \sum_e \frac{\vec{\tau} \cdot \vec{e} \Gamma_e}{\vec{n} \cdot \vec{e}} \left(\frac{\partial \varphi}{\partial \tau}\right)_e A_e \qquad (3.19)$$

where

$$\left(\frac{\partial \varphi}{\partial e}\right)_e = \frac{\varphi_{T2} - \varphi_{T1}}{\delta_{T1,T2}} \qquad \text{and} \qquad \left(\frac{\partial \varphi}{\partial \tau}\right)_e = \frac{\varphi_{C2} - \varphi_{C1}}{\delta_{C1,C2}}$$

where $\delta_{T1,T2}$ and $\delta_{C1,C2}$ represent the distances between T1 and T2 and C1 and C2 respectively.

### 3.3.4 Integrating the source term

If the source term is a function of $\varphi$ itself, it can be linearised as:

$$S_\varphi = S^U + S^P \varphi \tag{3.20}$$

Both $S^U$ and $S^P$ can be functions of $\varphi$. The source terms are then integrated over the control volume using the latest value of $\varphi$ (which is taken at the previous iteration):

$$\int_\omega S_\varphi d\omega = S_U + S_P \varphi_P \tag{3.21}$$

Where $S^P = S_p \omega$ and $S^U = S_U \omega$

Afonso et al. (Afonso et al., 2012) adapted the FVM to resolve the associated equations for electroosomotic flows specifically for viscoelastic fluids. They were able to capture the onset of instabilities that are prevalent specifically in electro-elastic flows providing a better understanding of the effect of electric fields on viscoelastic fluids. Similarly, Moshkin and Yambangwai (Moshkin and Yambangwai, 2012) elucidated volumetric flow rate values in the T-junction based on the numerical solution using the FVM. They reported the presence of unique flow patterns at particular points during the simulation and emphasised that their algorithm enabled them to determine the variation of volumetric flow rate with time in each channel of the junction at different pressure drop values.

In order to quantify the numerical errors and account for any variations in the solution, the order of accuracy of the numerical schemes need to be considered, which is discussed sections 3.6 and 3.7.

## 3.4 Velocity-pressure coupling methodology

### 3.4.1 Continuity and mass evaluation

The continuity equation governing mass conservation cannot be written in the form of the general convection-diffusion equation. It is used to determine the pressure field in the pressure-based method as employed in CFD-ACE+. Integrating the mass conservation equation over a finite volume cell generates the following expression:

$$\frac{\partial \rho}{\partial t} + \nabla \cdot (\rho \boldsymbol{u}) = \dot{m} \tag{3.22}$$

Integrating the equation above over the cell in figure 14, we get:

$$\frac{\rho^{a}\omega^{a} - \rho^{a-1}\omega^{a-1}}{\Delta t} + \sum_{e} \rho_{e} u_{e}^{n} A_{e} = \dot{m}\omega^{k} \tag{3.23}$$

where, $u_e^n$ represents the face-normal component of the velocity at face $e$, which is obtained by the inner product of the velocity vector $(u, v)$ and the face-normal vector $(n_x n_y)$.

$$u_e^n = n_x u_e + n_y u_e \tag{3.24}$$

Since the fluid density and velocities are available at cell centres, their respective face values need to be interpolated from cell-centre values. Linear interpolation de-couples the velocity and pressure fields giving rise to checkerboard instability. In CFD-ACE+, the checkerboard problem is circumvented by calculating the cell-face mass flux by averaging the momentum equation to the cell faces and relating the cell face velocity directly to the local pressure gradient (Date, 2003).

### 3.4.2 Pressure correction and SIMPLEC algorithm

Pressure correction techniques have been used widely for many years in the solution of the Navier-Stokes equations. The finite-difference equations obtained from the governing equations form a coupled non-linear system.

In the pressure correction method, the iterative scheme adopted is such that the momentum equations become uncoupled and can be solved sequentially in terms of an applied pressure field (Connell and Stow, 1986). The resulting velocity field in general, will not satisfy the continuity equation, therefore the applied pressure field must be corrected. Using pressure-velocity relationships from the linearised momentum equations, a pressure correction equation is derived from the continuity equation.

Pressure-based methods include the continuity equation to formulate an equation for pressure. Frequently used pressure-based methods include the Semi-Implicit Method for Pressure Correction (SIMPLE), , SIMPLER (SIMPLE−Revised), SIMPLEC (SIMPLE-Consistent)(Patankar, 1981) (Caretto et al., 1973) and PISO (Pressure Implicit with Splitting of Operators). The SIMPLE method is essentially a guess-and-correct procedure for the calculation of pressure on a staggered grid arrangement. In CFD-ACE+, the SIMPLEC (Semi-Implicit Method for Pressure-Linked Equations – Consistent) scheme has been adopted, based on the work of Van Doormal and Raithby (Van Doormaal and Raithby, 1984). SIMPLEC follows the same steps as the SIMPLE algorithm, with the difference that the momentum equations are

manipulated so that the SIMPLEC velocity correction equations omit the terms that are less significant than those in SIMPLE. The algorithm is derived from the finite difference form of the momentum equation for the cell centre of the triangle T1:

$$\Psi_{T1} v_{T1} = (\sum_i \Psi_i v_i + S_U)_{T1} - (\sum_e p_e A_e n_e)_{T1} \qquad (3.25)$$

In the equation above, $\Psi$ is the link coefficient and $S_U$ is the linearised source term described in section 3.5.4. The subscripts $e$ and $i$ denote each face of the cell and each adjoining cell, respectively. To initiate the SIMPLEC calculation process a pressure field $p*$ is guessed in order to solve the discretised momentum equations to yield the velocity components from equation 3.25 such that:

$$\Psi_{T1} v^*_{T1} = (\sum_i \Psi_i v^*_{T1} + S_U)_{T1} - (\sum_e p^*_e A_e n_e)_{T1} \qquad (3.26)$$

Using the above equation, however will still not satisfy continuity, hence using the corrections $v'$ and $p'$ will aid in acquiring an improved solution, where:

$$v = v^* + v' \qquad (3.27a\text{-}b)$$

$$p = p^* + p'$$

for which an expression can be obtained by subtracting Equation 3.26 from 3.25 and simultaneously assuming $v'_i$ can be approximated by $v_{P1}$, *we* obtain the following expression:

$$\Psi_{T1} v'_{T1} = \frac{-1}{\Psi_{T1} - \sum_i \Psi_i} \left( \sum_e p^*_e A_e n_e \right) \quad (3.28)$$

Then, the velocity correction at the face, $v'_e$, is obtained by averaging the cell centre values from adjacent cells (T1 and T2):

$$v'_e = \gamma_e v'_{T1} + (1 - \gamma_e) v'_{T2} \quad (3.29)$$

The conservation of mass equation was already integrated in 3.23, and if one defines the mass flux as:

$$C_e = \rho_e u^n_e A_e \quad (3.30)$$

We then have:

$$\frac{\rho^a \omega^a - \rho^{a-1} \omega^{a-1}}{\Delta t} + \sum_e C_e = \dot{m} \omega^a \quad (3.31)$$

If $v^*$ and $p^*$ are used to calculate $C_e$, the resulting $C^*_e$ will not satisfy equation 3.31, hence another corrective term is introduced:

$$C_e = C^*_e + C'_e \quad (3.32)$$

Equation 3.31 can be recast by incorporating the corrective mass flux:

$$\frac{\rho'_{TI}\omega^k}{\Delta t} + \sum_e C'_e = S_M \qquad (3.33)$$

In the above equation, $S_M$ represents the mass correction within the control volume:

$$S_M = \frac{\rho_{T1}^{a-1}\omega^{a-1} + \rho_{T1}^{*}\omega^a}{\Delta t} + \dot{m}\omega^a - \sum_e C_e^* \qquad (3.34)$$

With the face-normal velocity correction and the density correction expressed in terms of the pressure correction, substitutions can be made in equation 3.34 and the pressure correction can be obtained from:

$$\Psi_{T1} v'_{T1} = (\sum_i \Psi_i v'_i) + S_m \qquad (3.35)$$

A summary of the SIMPLEC procedure is:

1) *Guess a pressure field $P^*$;*
2) *Obtain the velocity field by solving Equation 3.26;*
3) *Evaluate $C^*$ from $\rho^*$ and $v^*$;*
4) *Evaluate the mass source, $S_M$;*
5) *Obtain the pressure correction from Equation 3.35;*
6) *Correct the pressure and velocity fields using Equation 3.27a-b;*
7) *Solve the discretized equations for other flow variables such as enthalpy, turbulent quantities, scalars etc. and finally,*

8) *Go to step 2 and repeat the procedure until convergence is achieved.*

## 3.5 Interface tracking

### 3.5.1 Volume of Fluid (VOF)

A wide range of numerical methods have been explored to study multiphase flows in microchannels, of which the Volume of Fluid (VOF) approach has been employed when the gas/liquid interface in bubble dynamics is of principal interest (Fang et al., 2008). The VOF method introduces a new variable $f$, which represents volume fraction for a particular fluid inside a cell. The volume fraction $f$ describes the phase distribution across each control volume. When $f = 1$ it indicates a control volume that is completely filled by liquid; on the other hand a volume fraction for the gaseous phase is represented by $f = 0$ and any other state has a value of $(0 < f < 1)$ (Gerlach et al., 2006). The time propagation of the volume fraction can be calculated by resolving the passive transport equation.

$$\frac{df}{dt} + \nabla \cdot (uf) = 0 \qquad (3.12)$$

where $f = \frac{\text{cell volume occupid by liquid}}{\text{total volume of the conrol volume}}$

Mirzaee et al. (Mirzaee et al., 2016) employed the VOF method to capture the interface deformation of the airborne bubbles formed by pumping a sample of air through a microchannel. Their simulations indicated that high velocity values contributed to the increase in the rate of release of airborne particles ejected from the bubbles which is essential in identifying the constituents of a sample of air which is essential in air quality monitoring.

Nabavi et al. (Nabavi et al., 2015) incorporated the VOF-CSF numerical model to simulate the droplet formation using three liquid phases. When an emerging bubble begins to form and extends into the main channel it forms a neck; this leads to a region of high pressure in the neck leading to its subsequent detachment from the stream. The increase in drag force exerted by the outer fluids competing with the interfacial tension leads to the stretching of the fluid thread downstream reinforcing the understanding of the phenomenon causing jet break up by providing exact flow and pressure distributions at the interface.

Although VOF is a powerful numerical tool, there are a few drawbacks associated with it when applying it to surface tension dominated flows in microchannels. Hoang et al. (Hoang et al., 2013) indicated that VOF does not resolve the interface location with sub-grid resolution, therefore the interface tracking of the thin lubricating film that forms near the walls is resolved at a substantial numerical cost presenting difficulties in understanding the physics at the exact point of break-up. In addition, unwanted currents disseminated from the calculation of the curvature as a result of the imbalance between the discrete surface tension force and pressure gradient terms which can be alleviated by introducing a filter(Lafaurie et al., 1994). Raeini et al. (Raeini et al., 2012) employed a Gaussian filter to smooth spurious velocities which enables the stable simulation of two-phase flow. Resolving the capillary equation independently of the dynamic pressure enables the filtration of capillary forces thus avoiding numerical errors and instabilities.

### 3.5.2 The Level set method

In this interface capturing method, the interface is said to be defined by a level set function, expressed by $\varphi$ (Osher and Sethian, 1988), the interface is represented by the zero level of $\varphi$. The function is initialised as a specific distance from the interface such that it is positive on one side of the interface and negative on the other. Material properties such as density,

viscosity, heat capacity and thermal conductivity are updated locally based on $\varphi$ (Lakehal et al., 2007). These methods have shown to be relatively simple to implement and yield accurate results if the interface is advected parallel to the coordinate axis (van Sint Annaland et al., 2006).

Lin (Lin, 2013) adapted a conservative level set model to simulate the electrohydrodynamic effects on a droplet upon application of a steady electric field. They observed good agreement with experimental results and suggested that this methodology can extend to simulating other electrohydrodynamic phenomena such as the formation of Taylor cones and electro-coalescence in the presence of AC electric fields. Bashir et al. (Bashir et al., 2014) describe that by using the level-set method, pressure variations in the dispersed phase $(P_d)$ were observed. These findings differ from those of Garstecki et al. (Garstecki et al., 2006), which suggested that the $(P_d)$ remains constant during the formation of droplets. The former, emphasised that important advances in understanding of the underlying physics of droplet formation will capacitate control and precision over droplet formation in the laboratory.

## 3.6. Interpolation schemes

### 3.6.1 First order upwind scheme

First order upwind schemes are first order accurate(Brooks and Hughes, 1982) and are established linear and stable methods for the numerical approximation of linear transport problems(Boyer, 2011). This numerically stable scheme is used to express $\varphi$ at the face of the cell, *e*. In this scheme, the upstream grid point is used, so $\varphi$ equals either $\varphi_{T1}$ or $\varphi_{T2}$ depending on the direction of flow at the cell face *e*:

$$\varphi_e^{UP} = \begin{cases} \varphi_{T1} \; if \; v_e^n > 0 \\ \varphi_{T2} \; if \; v_e^n < 0 \end{cases} \tag{3.36}$$

Although this is easy to implement in code and eradicates the presence of any oscillations(Langtangen, 2013, Tamamidis and Assanis, 1993), the drawbacks include diffusion, which grows larger when the flow being studied is of high Reynolds Numbers. This in turn compromises the overall accuracy of the solution by generating false dissipation. Brandt and Yavneh (Brandt and Yavneh, 1991) added that excessive artificial viscosity in the numerical scheme and course grids also contribute to erroneous solutions. Therefore higher order schemes are recommended in order to reduce numerical errors and (Hardt and Schönfeld, 2003).

### 3.6.2 Power law scheme

The Power law scheme(Patankar et al., 2002) is based on the analytical solution of the one-dimensional convection-diffusion equation(Carroll et al., 2010). This finite differencing scheme is equivalent to the first-order upwinding scheme for convection when the grid Peclet numbers are approximately greater than 6 (Leonard and Mokhtari, 1990). The Peclet number is a dimensionless parameter, defined as the ratio between the convective velocity to the diffusive velocity(Bhattacharya and Hwang, 1997).

Wang et al(Wang et al., 2003) utilised power law correlations to acquire a solution in the presence of more than two variables under a variety of conditions. However, in practical three dimensional cases with coarser meshes, the actual grid Peclet number is larger than 6 throughout the bulk of the flow domain. Therefore, this indicates that power law scheme operates as the first-order upwind scheme everywhere in the flow-field except at a very small fraction of the grid-points near the boundaries and in regions of stagnation where the convective velocities are small. This introduces cross-stream false diffusion when the grid lines and stream lines are not coincident, therefore necessitating higher order schemes to mitigate this issue.

## 3.7 Second order schemes

### 3.7.1 Second order upwind scheme

Second order schemes are incorporated in numerical schemes in order to alleviate spurious oscillations prevalent in first order schemes(Warming and Beam, 1976). False diffusion arises as a result of numerical approximations for advective terms in the governing differential equations. They tend to have truncation errors that can artificially increase the diffusive transport of species in the numerical solution, suppressing sharp gradients and also over estimating the degree of mixing(Bailey, 2017). Bailey (Bailey, 2017) underlines the fact that higher order upwind schemes have superseded first order upwind schemes by reducing false diffusion. They offer a balance between solution accuracy and complexity, computational time and issues regarding stability.

Shyy et al.(Shyy et al., 1992) observed such interpolation scheme provide satisfactory results in the context of three dimensional turbulent flow computations. Atias et al (Atias et al., 1977) employed the second order upwind scheme to study the driven cavity flow and the problem of an impinging jet on a normal flat plate and achieved promising results. Li et al.(Li and Zhong, 2015) conducted a comparative study between the first order upwind, second order upwind, Quadratic Upwind Interpolation for Convective Kinetics (QUICK) discretisation and third-MUSCL (Monotonic Upstream-Centred Scheme for Conservation Laws) discretisation schemes to study the gas-liquid-solid three phase flow dynamics in bubble columns . They observed that the second order upwind scheme had the lowest magnitude of errors in the radial and axial directions.

Conversely, Vanka (Vanka, 1987) argued that second order upwind scheme still does not display satisfactory performance in terms of both numerical accuracy and computational stability. Similarly, Zhou et al(Zhou et al., 2016) highlights that second-order upwind interpolation still introduces excessive numerical dissipation especially in passive transport.

### 3.7.2 Central differencing scheme

As opposed to the First-Order Upwind Schemes, Central Differencing offers 2nd order accuracy. Upwind methods have gained substantial criticism due to the artificial diffusion they introduce, therefore much attention has been given to solutions based on central differences (Brooks and Hughes, 1982) . Tamamidis et al (Tamamidis and Assanis, 1993) reported that higher order schemes may lead to unphysical, oscillatory behaviour in the presence of steep gradients.

In the conventional second-order accurate central difference scheme, convective derivatives for quantity $\varphi$ are evaluated between two points $T_1$ and $T_1$ (ESI-Group, 2013) :

$$\varphi_e^{CD} = \gamma_e \varphi_{T1} + (1 - \gamma_e)\varphi_{T2} \qquad (3.37)$$

The central differencing scheme tends to reduce false diffusion substantially, however at large grid or Peclet numbers is prone to oscillations(Li and Tao, 2002), It is of course intuitive to ensure stability and to eliminate such spurious oscillation by reducing grid cell size (which results in lower local Peclet numbers), however this is not always possible, since reducing cell size may result in prohibitive mesh sizes and computational costs. To prevent oscillations, yet maintain an acceptable level of accuracy and manageable messes, sometimes a blending factor $(\alpha)$ is incorporated, and the equation becomes:

$$\varphi_e = \alpha \varphi_e^{UP} + (1 - \alpha)\varphi_e^{CD} \qquad (3.38)$$

Blending works by obtaining the flux value from a lower-order scheme such as the upwind scheme $(\varphi^{UP})$ (ESI-Group, 2013, Papadakis and Bergeles,

1995) and combining it with the flux obtained from the central difference scheme, represented by the right hand side of the equation.

Mao et al. (Mao and Koser, 2006) employed the central differencing scheme to iteratively calculate the magnetic field strength inside a ferrofluid as well as the flow and spin velocities of the magnetic particles in closed channel geometries. There was good correlation with their experimental results.

Reshadi et al. (Reshadi et al., 2016) demonstrated using the central differencing scheme in their numerical model that they were able to ascertain that in polymer electrolyte solutions with large Debye lengths. The secondary flow pattern and the shape of vortices are generally reliant on width-to-height ratio of the microchannels. The numerical model they developed provided important quantities that are of high practical importance in the design of microfluidic devices to manipulate viscoelastic fluids. Similarly, Yan et al. (Yan et al., 2004) were able to obtain important electric quantities that induce secondary flows which contribute to heat transfer in electrohydrodynamic enhanced nucleate boiling for renewable energy applications. Lami et al. (Lami et al., 1997) added that electric field components at each node can be evaluated leading to good accuracy without any interpolation. Shim et al. (Shim et al., 2007) emphasised that finer grids need to be utilised in order to use this scheme for non-linear problems.

## 3.8 Linear solvers

### 3.8.1 Conjugate Gradient Squared (CGS)

The Conjugate Gradient Squared (CGS) method is an iterative method for solving non-symmetric linear systems of equations. It requires no additional user specified parameters (Youssef and University, 2007), and is popular for its simple implementation (Geschke et al., 2006).

In this solver, the coefficient matrix is treated like a minimisation problem and preconditioning facilitates convergence. Besides requiring a small constant number of vectors as the memory overhead, it is also relatively simple to parallelise. However, the CGS solver is burdened with longer computational time when fine meshes are used. Furthermore, it generates large intermediate residuals affecting its overall accuracy and convergence of the solution (Fokkema et al., 1996).

Shuttleworth et al.(Shuttleworth et al., 2011) used the CGS solver along with a preconditioner to obtain a solution for the fluid mixing within their microfluidic device. Zhao et al. (Zhao et al., 1991) observed that the quality of the CGS method depends on the preconditioner. It is common practice to use CGS methods in conjunction with preconditioners to improve the rate of convergence(Reijns and Luo, 1992). Preconditioning conditions a specific problem into a form that can be resolved more efficiently in an iterative manner(Langtangen, 1989).

Garg et al. (Garg et al., 2015) employed the CGS with a preconditioning solver to acquire velocity, enthalpy and other scalar variables to improve the accuracy of the CFD simulations of flow in microreactors. Shamsi et al. (Shamsi et al., 2016) developed a model to investigate the separation efficiency of blood plasma in microfluidic analytical chips. They used a preconditioned bi-conjugate solver to obtain solutions to the discretised equations which displayed good convergence and reasonable correlation with experimental results.

However, the fundamental limitation of the conjugate-gradient method is that it takes a substantial number of cycles to reach convergence (Tronrud, 1992). It is generally preferred to have a solver that reaches the minimisation requirement in the shortest duration of time.

### 3.8.2 Algebraic Multigrid Solver (AMG)

There are two main multigrid approaches – Geometric and Algebraic. In geometric multigrid, the geometry of the problem is used to define the

various multigrid components. Algebraic multigrid (AMG) methods use only the information available in the linear system of equations and are therefore suitable to solve problems on more complicated domains and unstructured grids (Yang, 2006). This solver achieves convergence by utilising both coarse and fine grids (Sertel and Volakis, 2000): it works by coarsening the grid in all directions, achieving solutions that reduce longer wavelength errors and injecting/interpolating those back to the finer meshes. These are subsequently smoothed by the solver until a desired residual tolerance is achieved. The solution process involves relaxation to supress high-frequency components of the error, transfer of residuals from fine to coarse grids, and interpolation of corrections from coarse to fine levels. The short wavelength errors are effectively reduced on the finest meshes, whereas the long-wavelength errors rapidly decay on the coarsest meshes.

Yang(Yang, 2006) describes that the central idea behind AMG solvers is to eliminate errors at multiple wavelengths simultaneously. More specifically, this is achieved by solving the equation $\boldsymbol{Au} = \boldsymbol{f}$ for a coarser grid(Cleary et al., 1998), where $|\boldsymbol{A}|$ is an $n\ x\ n$ matrix with entries $a_{ij}$. $u_i$ denotes the value of $u$ at point $i$, the corresponding grid is represented by $\Omega = \{1,2, \ldots., n\}$. The central idea is to eradicate the error, $e$ after relaxation by coarse grid correction. This can be achieved by solving the residual equation $\boldsymbol{Ae} = \boldsymbol{r}$ on a coarser grid, then interpolating the corresponding error to the fine grid to correct the error by $u \leftarrow u + e$. Since this process is solely based on the algebraic equations, solution is not dependent on the grid or the geometry (Cleary et al., 1998, Stuben, 2012). AMG offers two significant advantages over the CGS solver in that:

a) The increase in solver time is solely dependent on the number of unknowns in the equations;
b) It offers a faster convergence.

In order to solve equations that govern the electro-osmotic flow in a microfluidic reactor, Comandur et al. (Kaushik Arumbuliyur et al., 2010)

employed AMG solver within a Multiphysics suite (ESI-CFD Inc., Huntsville, AL) to calculate the velocity, applied electric field and concentrations of the reacting samples and the product in the flow domain. Palaniappan et al. (Sethu et al., 2006) modelled their microfluidic device as a fluidic circuit with discrete elements. Using the aforementioned solver, they were able to obtain residual convergence to at least 4 orders of magnitude within ~1000 iterations, indicating its robustness as a solver. It also enabled them to investigate modifications on existing devices with the prospect of optimising them. The drawback of AMG solvers is the slight complexity in terms of model set-up especially in micro-scale geometries, where the generation of a coarse mesh with a few grid points might not be feasible(Kickinger, 1998). Another disadvantage is that it can be expensive in terms set-up time particularly for three dimensional problems (Iwamura et al., 2003), and also has higher computer memory requirements (Stuben, 2012, Iwamura et al., 2003).

# Chapter 4

## Experimental details

### 4.1 Introduction

This chapter describes the materials and systematic procedures used for the experimental section of this thesis. The construction of the apparatus from individual components is one of the most important aspect of this research. There are two experimental configurations developed in this work, both including an amplifier to superimpose an AC electric field onto a DC electric field. The individual connections to the peripheral components are discussed. Both set-ups are used in conjunction with a T-junction device fitted with a stainless steel capillary to generate the microbubbles, which is also explained in detail. All the equipment was calibrated to ensure that the electric potential values being supplied to the input of the amplifier are the same as the one being supplied at the load. All experiments were conducted using the novel apparatus.

### 4.2 Materials

The main material used for the initial experiments in order to evaluate the effect of superimposed electric fields on microbubble formation was a solution of aqueous glycerol combined with the surfactant polyoxyethylene glycol 40 stearate (PEG 40S). For the experiments conducted to investigate the effect of varying the mixing geometry and electric field strength on microbubbles, Bovine Serum Albumin (BSA) of two different concentrations

were used. The materials used for the experiments are shown in tables 1 and 2.

### 4.2.1 Glycerol

Glycerol with 99% purity ($C_3H_8O_3$, density 1261 kg m-3, molecular weight 92.09, viscosity 1.4 Pa s Sigma Aldrich, U.K.) was diluted with distilled water. Aqueous glycerol solutions are widely used in experimental studies of flow phenomena. Experiments conducted with glycerol solutions facilitate investigation of flows in a wide range of Reynolds numbers (Cheng, 2008).

### 4.2.2 Polyethylene glycol 40-stereate

Polyethylene Glycol-40-Stearate (Sigma Aldrich,UK) is a non-ionic/neutral surfactant used to reduce surface tension and facilitate bubble formation. It is biocompatible and is approved by the FDA for use as excipients or as a carrier in different pharmaceutical formulations, foods, and cosmetics (Shan, 2004, Xing et al., 2010).

### 4.2.3 Bovine serum albumin

Bovine serum albumin (BSA, molecular weight 66,430 Da, Sigma Aldrich, UK) is a well characterised biological protein (Wen et al., 1999). BSA has shown to help regulate to colloid osmotic blood pressure and contributes to the transport of various metabolites(Hossain et al., 2011). It is a preferred material to develop echo contrast agents (Grinstaff and Suslick, 1991, Avivi et al., 2003) and in drug delivery due to its abundance, low cost and ease in purification(Elzoghby et al., 2012). They have also shown promise as a shell material for theranostic agents to enhance thrombolysis in the presence of

fibrin clots(Yan et al., 2017). Due to the homology between BSA and human serum albumin, it has also been used as a model drug(Kurrat et al., 1997).

## 4.3 Characterisation of the solutions

This section details the methods employed to characterise the various solutions that were utilised in this research.

### 4.3.1 Viscosity

An Ostwald Viscometer, also known as U-tube viscometer (Schott Instruments, GmbH, Mainz, Germany) was used to determine the kinematic viscosity of the solution as shown in figure 15.

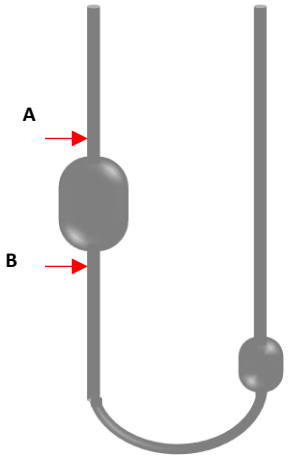


*Figure 15: Ostwald Viscometer.*

The dynamic viscosity $m\ Pa\ s$ is calculated by:

$$\eta_s = \eta_w \frac{t_s \rho_s}{t_w \rho_w} \qquad (4.1)$$

Where, $\eta_s$ and $\eta_w$ are the dynamic viscosities of the solution and water respectively. Water is used as the calibration fluid as all its physical properties are well known. $\rho_s$ and $\rho_w$ are the densities of the solution and

water respectively. The time taken for a liquid to pass from point A to B was obtained for $t_w$ (time taken for water to travel from A to B) and $t_s$ (time taken for solution to travel from A to B in seconds). The mean of five trials was obtained and reported in this thesis.

### 4.3.2 Density

The density of the solutions used in the experiments were measured using a 25 ml DIN ISO 3507- Gay-Lussac type standard density bottle (VWR International, Lutterworth, UK). The mass of the empty bottle and the mass of the bottle filled with solution were obtained using an electronic balance (AND HF-1200G A&D Instruments Ltd., Japan). The density ($\rho$) was calculated by employing the following protocol:

The mass of the empty density bottle = $W_b$ (g) (4.2)

The mass of the density bottle filled with liquid /solution = $W_l$ (g) (4.3)

Therefore, the mass of the solution =$(W_l - W_b)$ (g) (4.4)

Therefore, the density of liquid /solution = $\frac{(W_l - W_b)}{25}$ (g cm-3) (4.5)

The series of calculations were repeated five times and the mean value calculated was taken as the density of the solutions used in this work. The measurements were taken at an ambient temperature (~22-25°C)

### 4.3.3 Surface tension

The surface tension of the solution was measured using a Kruss Tensiometer K9 (Kruss, GmbH, Hamburg, Germany) (Wilhelmy's Plate method), this device has a metal plate suspended above a platform. The metal plate is slowly submerged into the solution, and slowly withdrawn until the contact

angle is zero, thus the force exerted on the plate is displayed. To minimise errors, five trials were taken for each sample and the plate was washed thoroughly with ethanol and distilled water between trials to prevent erroneous results.

### 4.3.4 Electrical conductivity

The electrical conductivity was measured using a Jenway 3540 conductivity meter (Bibby Scientific, Staffordshire, UK). This was done by submerging the electrode into the solution for 10 minutes and obtaining the reading from the gauge, similar to the other characterisation techniques described above, the average value of five trials was taken as the electrical conductivity.

## 4.4 Preparation of solutions

### 4.4.1 For the novel preparation of monodisperse microbubbles by integrating oscillating fields with microfluidics

50% wt. Glycerol of 99% purity was diluted with distilled water, 1% wt. PEG-40-S was added to the solution in order to reduce the surface tension, stabilise the interfaces and to promote bubble formation. This was left to stir on an electric stirrer for 24 hours before the experiment was conducted to ensure a homogenous solution is formed.

The physical properties for the solution were measured five times, and the average values obtained are shown in table 1. Compressed nitrogen was the gas chosen as the dispersed phase.

| **Solution** | **Viscosity / mPa s** | **Surface Tension /mN $m^{-1}$** | **Electrical Conductivity/ µS $m^{-1}$** |
|---|---|---|---|
| **50% wt. Glycerol, 1% wt. PEG-40-S** | 8 | 54 | 2.0 |

*Table 1: Measured values of viscosity, surface tension and electrical conductivity.*

### 4.4.2 For the study of the effect of the mixing region and collector distance on microbubble formation coupled with AC-DC electric fields

Solutions comprising bovine serum albumin (BSA) (Sigma Aldrich, Poole, UK, molecular weight: 66000 $g\,mol^{-1}$ were dissolved with distilled water. Solutions of two different BSA concentrations were prepared - $10\,\%\,wt.$ and $15\,\%\,wt.$ and left to stir for 24 hours before the experiments were conducted in order to ensure complete dissolution. The physical properties shown in table 2 were obtained by calculating the average of five consecutive measurements.

### 4.4.3 For the study of the effect of optimised parameters on microbubble generation

This experiment was conducted using a $10\,\%\,wt.$ BSA solution; the preparation is described in section 5.4.

| Solution | Viscosity (mPa s) | Surface Tension (mN $m^{-1}$) | Electrical Conductivity ( µS $m^{-1}$) | Relative permittivity at 25.3°C | Density (kg $m^3$) |
|---|---|---|---|---|---|
| **10% wt. BSA** | 1.0 | 56 | 5.00 x $10^6$ | 67.3 | 1065 |
| **15% wt. BSA** | 1.6 | 51 | 6.44 x $10^6$ | 81.5 | 1070 |

*Table 2: Measured values of viscosity, surface tension, electrical conductivity, relative permittivity and density.*

## 4.5 Capillary embedded T-junction

The T-junction geometry used in this work comprising of two Teflon Fluorinated Ethylene Polypropylene (FEP) capillaries (Upchurch Scientific, Oak Harbour, USA) with fixed internal diameters of $100\ \mu m\ (0.1mm)$ and outer diameters of $1.6mm$ were inserted perpendicularly into a

polydimethylsiloxane (PDMS) block of dimensions(100x100x10). These form the inlet channels for the T-junction device. A third stainless steel capillary of same dimensions was arranged coaxially with the gas inlet capillary forming the outlet channel of the T-junction. A schematic of this arrangement is presented in figure 16.

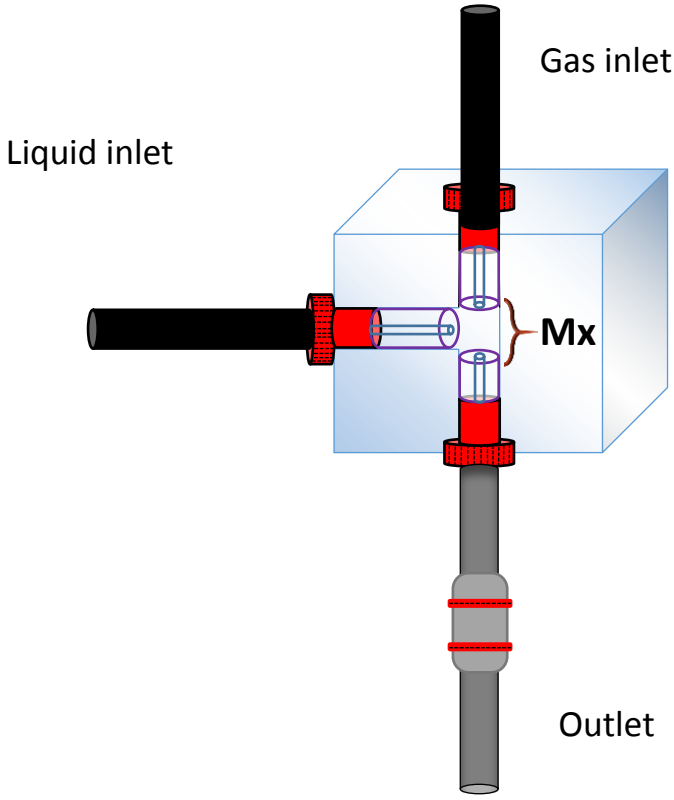


*Figure 16: Schematic of T-junction device indicating inlet and outlet channels. Mx represents the mixing region distance.*

The gap between the gas inlet and outlet was initially set to $200\ \mu m$ for the initial experiments which is referred to as the mixing region $(M_x)$ herewith. $(M_x)$ is varied in the study of the effect of the mixing region on the formation of microbubbles. The gas inlet was connected to a gas regulator which was fitted to a pressurised gas tank containing compressed nitrogen. The gas was supplied to the junction at a constant pressure $(P_g)$ via a 6mm diameter tubing connected to the gas inlet.

A digital manometer was connected to the pipe in order to monitor and measure the in-line gas pressure. The liquid inlet capillary is connected to a

20ml stainless steel syringe (KD Scientific, Holliston, Massachusetts, USA) which acts like a reservoir for the solution. The bubble formation is described in detail in section 4.6.

## 4.6 Microbubble formation

The bubble formation mechanism remains constant across both experimental configurations. The solution was infused into the system at a fixed volumetric flow rate of 100µl/min at a fixed pressure of $256\ k\ Pa$ for all the experiments using a Harvard Syringe pump PHD-4400 (Harvard Apparatus Ltd., Edenbridge, UK).

The fluids meet at the junction area, where the formation of the bubbles occur, which then traverse through the outlet capillary and collected on a glass slide. In order to introduce the electric potential, the high voltage output is connected to the stainless steel outlet, which acts as a conducting surface. In each experimental configuration, the high voltage output is connected to the stainless steel outlet, and the circuit is completed by connecting the ground platform to the high voltage return pin on the amplifier.

## 4.7 Experimental set-up

There are two different experimental configurations presented in this thesis each consisting of a power amplifier delivering the amplified voltage output at the load (Kothandaraman et al., 2017). The amplifiers employed differ in terms of power and frequency output. A signal is generated from a waveform generator is used to drive the input of the power amplifier. An oscilloscope is integrated to the set-up in order to track the waveform that is sent to the amplifier. This section provides detailed descriptions of both experimental configurations (figures 17 and 24) and the peripheral components associated with them.

## 4.8 Specific experimental details for the novel preparation of monodisperse microbubbles by integrating oscillating electric fields with microfluidics

This experimental set-up consisted of two Teflon FEP (Fluorinated Ethylene Polypropylene) capillaries arranged perpendicularly in a Polydimethylsiloxane (PDMS) block to represent the liquid and gas inlets. A third stainless steel capillary was embedded in the polymer block coaxially with the gas inlet ensuring that the distance between both capillaries is $200\ \mu m$ creating a junction for both phases to meet $(M_x)$. The solution in table 1 was pumped at a steady volumetric flow rate into the junction, where it meets the discontinuous fluid medium (nitrogen gas).

Each capillary was fastened securely using a combination of High Performance Liquid Chromatography (HPLC) connectors and ferrules that act as washers, thus prevent any leaks or gas from escaping. All capillaries were rinsed with distilled water and inspected for leaks or blockages prior to conducting the experiments.

An offset with a superimposed waveform of a particular frequency was set on the waveform generator which is used to drive the input pins of the high voltage amplifier. The amplifier then amplifies an input of $(0 - 10\ V)$ to $(0 - 20\ kV)$, the HV output cable is connected to the stainless steel capillary by means of an alligator clip. The circuit was completed by connecting the ground platform to the return port of HV by means of an 'O' connector. The low voltage power supply unit (PSU) delivers a voltage of $24\ V$ required to power up the amplifier. The oscilloscope allows us to view the waveforms entering and exiting the HVA (figure 17).

The purpose of this study was to investigate the effect of superimposed fields on the generation of microbubbles. Firstly, the effect of superimposed AC on microbubble formation ranging between $2 - 4\ kV_{P-P}$ was reported, followed by the effect of frequency between $100 - 2200\ Hz$, which is the maximum frequency output achievable with the Ultravolt amplifier.

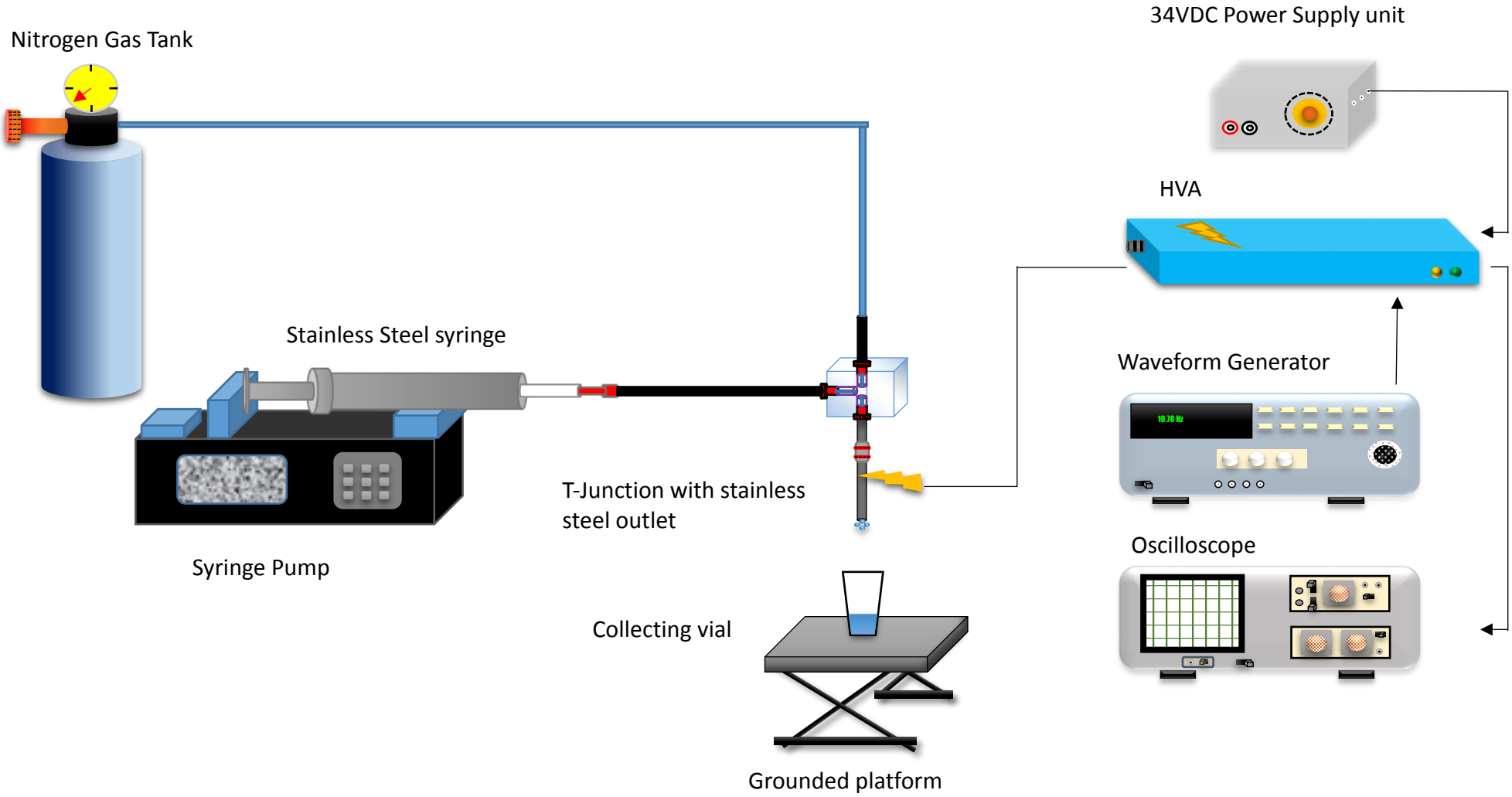


*Figure 17: Schematic of experimental set-up used to superimpose AC on a DC electric field.*

### 4.8.1 Description of equipment

A comprehensive description of each component of the experimental set up is presented in this section. Each component is individually wired to the pins present on the female d-type connector to form a plug, a detailed explanation to each of these connections is provided in the next section.

#### 4.8.1.1 High voltage amplifier

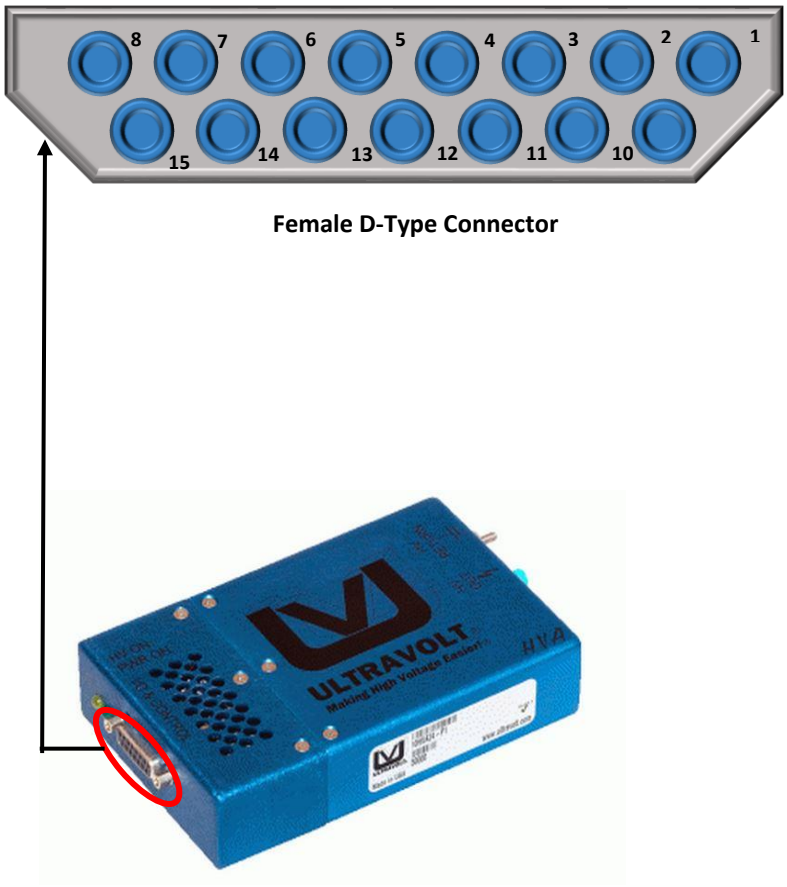


*Figure 18 a) 15-pin female D-type connector displaying the pin arrangement.*

A High Voltage amplifier (HVA)(20HVA, 24-BP2, 2W, Ultravolt, New York, USA) is used to amplify a low voltage input to a high voltage output, it is a crucial component of this experimental set-up. This unit is fitted with a

differential operational amplifier which generates an amplified output of the difference between two input voltage signals(Kitchin and Counts, 2004).

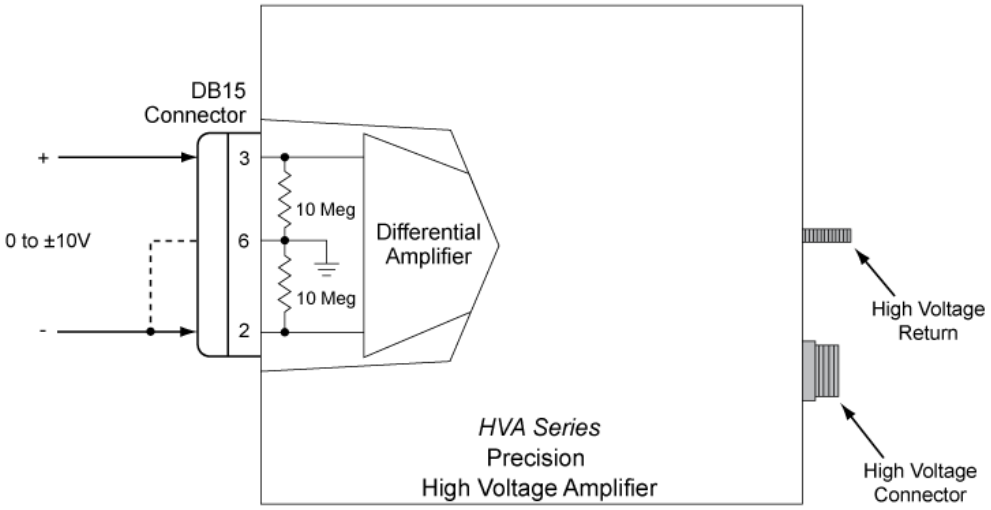


*Figure 19: Inbuilt differential amplifier of the HVA.*

Figure 19 is extracted from the technical notes of the HVA unit, and represents the pin connection to generate a positive differential output. The positive (+) or live terminal from the voltage source is connected to the positive (+) pin of the Voltage programming pin (V2) and negative (-) pin is connected to ground. Therefore, the output voltage can be expressed as:

$$V_{out} = V_2 - V_1 \qquad (4.6)$$

Each pin has a separate function, and allows the connection of various peripheral appliances depending on the intended application. These pins are either input, output or redundant pins, redundant pins are isolated from the main internal circuitry and are indicated by N/C indicating 'No connection'. There are numerous D-Type connector configurations such as 9 pin, 15 pin, and 29 pin, therefore if the functionality of the connector is limited to 13

pins, 2 additional pins are added to avoid an odd pin arrangement. The D-type connector in this unit has 15 pins in total including 2 N/C pins.

Wires with a cross sectional area of $0.28\,mm^2$ (PVC, 23 AWG, RS components, Corby, United Kingdom) were soldered onto a Male D-type Connector plug, and each open ended wire was connected to the peripheral devices using terminal block connectors. The wires were insulated using heat shrink tubing (TE connectivity, $1.2\,mm$, Stanmore, UK) which also provides strain relief at the point of connection. A description of the function of each pin and their connection is provided in figure 20.

The output is then connected to the T-junction outlet capillary by means of an alligator clip as shown in figure 17.

| Pin | Description | Function | Connection |
|---|---|---|---|
| 1 | + 10V Reference voltage | This is an internally generated voltage of +10V, which can be used to drive other inputs of the HVA. | The wire from pin 1 is connected to Pin 11, in order to enable the HV |
| 2 | Voltage Programming (-) | 0 to - 10 volt signal to generate full output voltage | Connected to pin 6 (signal ground), as a negative signal is not used in this study. |
| 3 | Voltage Programming (+) | 0 to + 10 volt signal to generate full output voltage | Connected to Channel 2 of the waveform generator |
| 4 | Voltage Monitor | 0 to ± 10V to View full output voltage | Connected to channel 2 of oscilloscope which in turn displays the waveform. |

| | | | |
|---|---|---|---|
| 5 | N/C | This terminal is not connected to the internal circuit of the HVA, but an open wire. | N/C |
| 6 | Signal Ground | All control signals are referenced here | Channel 2 Ground terminals from the oscilloscope and frequency generator along with the negative voltage programming pin (pin 2) are connected to this pin |
| 7 | Input Power | Input power of +24VDC required to power the HVA up. | The 36VDC Power Supply unit supplies the +24V required to power up the HVA from the +ve terminal, by applying a constant DC voltage. |
| 8 | Input power | Additional Power pin | Connected to pin 10. |
| 9 | Power Ground | Input power return | The -ve terminal of the PSU is referenced to ground |
| 10 | Power Ground | Input Power Return | Chassis ground of the VDC and additional Input Power (pin 8) are connected to this terminal. |
| 11 | Enable | Composed of Transistor-Transistor Logic (TTL) design, whereby the bipolar transistor in the device acts upon direct | Pin 1 provides a voltage of 10V when connected to this pin, thus enabling |

| | | | |
|---|---|---|---|
| | | pulses. (based on binary logic). 0-0.08V = Disable (logic 0). 2.5-10v = Enable (logic 1) | the HV, to provide an output to the load. |
| 12 | Current Monitor | 0 to ± 10V to View full output voltage | Connected to channel 1 of the oscilloscope to display the current passing through the unit. |
| 13 | Current Limit Adjust | 0-10V sets the current limit 0 to +10V sets current from 0 to full output current | Connected to pin 1 to enable full current usage |
| 14 | N/C | No Connection | N/C |
| 15 | Signal Ground | All control signals are referenced here | Ground terminals from channel 2 of the oscilloscope and pin 13 are connected to this pin. |

*Figure 20: Functional description of each allocated pin number and their respective connections.*

#### 4.8.1.2 Waveform generator

A waveform generator (Wavestation 2012, Teledyne Lecroy, Chestnut Ridge, New York) is integrated into the circuit to produce periodic signals. Modern waveform generators such as the unit used in this work can produce conventional waveforms such as sinusoidal waves, extending to more complex ones such as square, sawtooth, pulse and noise.

The output from the waveform generator is used to drive the voltage programming pins on the HVA. The output from the unit is connected to the oscilloscope and the HVA using a T-Junction BNC connector, such that the input signal can be viewed. Various important parameters to be modulated include amplitude, frequency, and offset.

## Amplitude

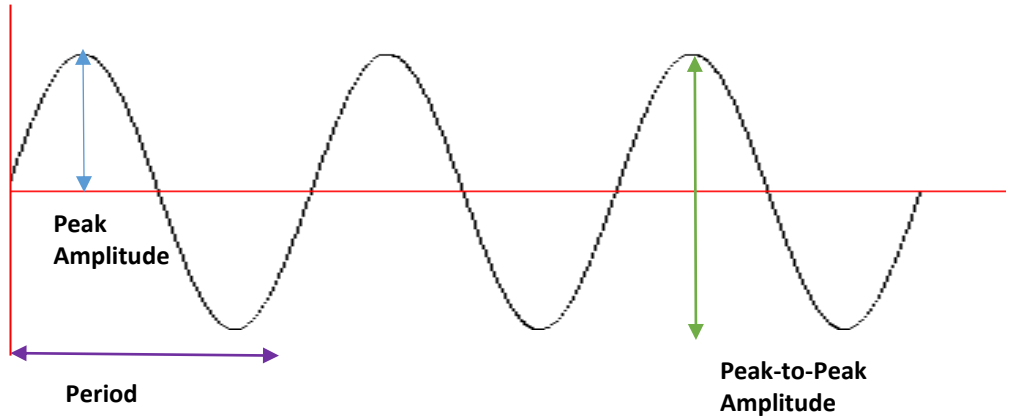


*Figure 21: Schematic of waveform characteristics such as the peak amplitude, period of the waveform, peak-to-peak amplitude and frequency.*

The amplitude of a wave is defined as the maximum height that can be reached by the crest of the waveform. The peak amplitude $V_p$ represents the voltage from the 0 marker to the crest of the waveform. The amplitude can also be described as a peak-to-peak $V_{p-p}$ value, which is the range between trough till the crest of the waveform as shown in figure 21.

## Frequency

This is defined as how often a cycle/wave occurs in a given time interval. The unit of frequency is Hertz $(Hz)$.

## Period

The period of a wave is defined as the number of cycles per second and is related to frequency by:

$$P = \frac{1}{f} \qquad (4.7)$$

**Offset**

The DC offset control is an essential feature of the signal generator in this work. Normal AC fields tend to oscillate between the positive and negative regions of the baseline. This oscillation cab be modulated to occur above the 0 baseline using this function. For example, setting the offset value as $5\ kV$, essentially makes $5\ kV$ the new baseline for the waveform, and setting the amplitude to $4kV_{P-P}$ oscillates the resultant waveform between $3\ kV$ and $7\ kV$ i.e. an AC field of $4kV_{P-P}$has been superimposed onto a DC field of $5\ kV$.

#### 4.8.1.3 Oscilloscope

An Oscilloscope (WaveAce 2002, Teledyne Lecroy, Chestnut Ridge, New York) is used plot the graph of the voltage vs time. It enables the waveform that is sent to the HVA to be tracked and allows important features of the wave to be analysed such as frequency, amplitude, phase and period. The output from the frequency generator and the voltage monitoring output from the HVA are connected to the oscilloscope such that the input and output signals can simultaneously be viewed and assessed for coherence.

**Explanation of oscilloscope Plots**

The time base provides a scalar way of reading the x-axis. Figure 22 displays a sinusoidal wave with an offset of $500\ V$, a superimposed AC voltage of $1\ kV_{P-P}$ at a frequency of $20\ Hz$. The period of the wave equates to 0.05s. There are 18 divisions on the screen, and the time base is set to 25ms/division, therefore the time base will reach 0.45s (18 x 0.025s). Dividing 0.45s by the period of the signal yields the number of cycles of the signal, which in this case is 9.

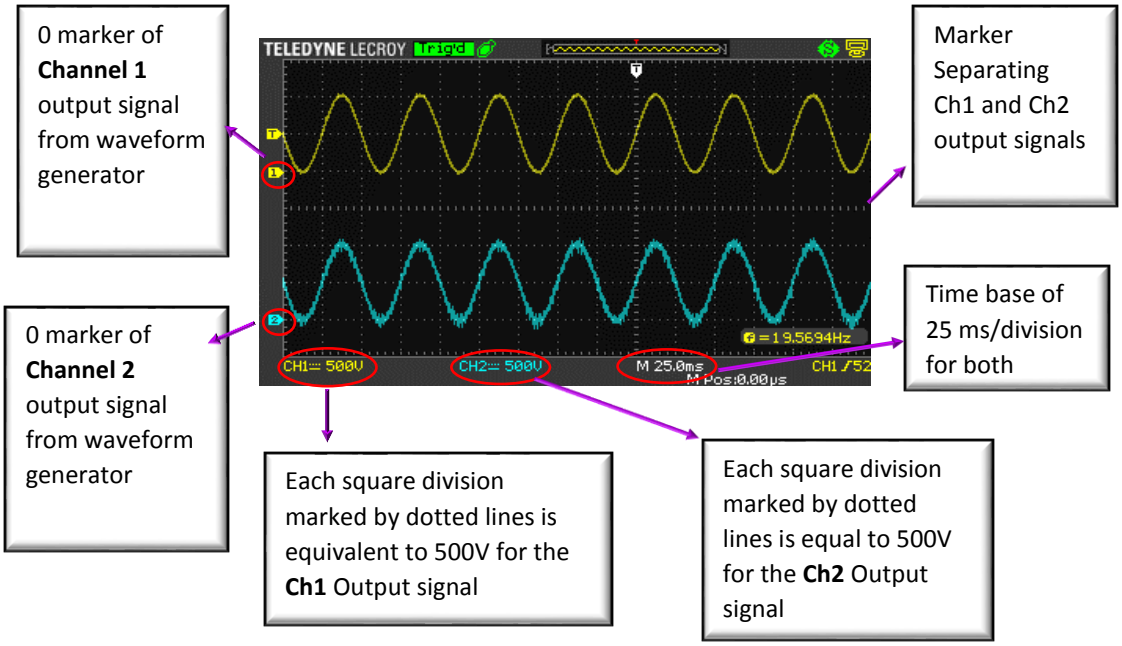


*Figure 22: Explanation of oscilloscope plots.*

#### 4.8.1.4 Low voltage power supply unit (PSU)

A low voltage PSU is used to power up the HVA (36Vdx, Z+ series, Z+36-6, TDK-Lambda America Inc.). This is a $36\ VDC$ supply, hence the voltage is set to $24\ V$, as this is the potential difference required to drive the power inputs of the HVA. The chassis ground of the unit is connected to the power ground pins of the HVA.

### 4.8.2 Calibration of equipment

#### 4.8.2.1 Calibration of HVA

In order to verify that the voltage being supplied by the HVA is the same as the one being supplied to the load, a High Voltage Probe (Fluke,80k-40, Everett, Washington) embedded with $10\ \mathrm{M}\Omega$ resistor which acts as a 1000:1 potential divider. It was connected to a digital multimeter (Fluke, $10A$ AC, $1000V$ AC). The high impedance HV probe essentially steps-down the measured voltage by a factor of $1000\ V$, i.e. a measurement of $2\ kV$ was recorded as $2\ V$ on the multimeter. The AC component was also checked, by

changing the setting on the multimeter. It was recorded as an $rms$ voltage, this was converted into a P-P voltage by:

$$V_{rms} = \frac{V_0}{\sqrt{2}} \tag{4.8}$$

where $V_0$ represents the peak voltage of the waveform.

#### 4.8.2.2 Calibration of input and output signals

The signal that drives the inputs of the HVA was verified against the output signal from the HVA. The waveform generator was directly connected to channel 1, using a BNC T-connector piece, from which the second connection was made to the input of the HVA. A direct connection was made from the monitoring pin on the HVA, to view the output signal. From figure 23 in can be seen that the signals are relatively in phase, apart from a marginally distorted output signal (due to noise prevalent in the amplifier), which consequently generates a harmonic distortion (Rijns, 1996).

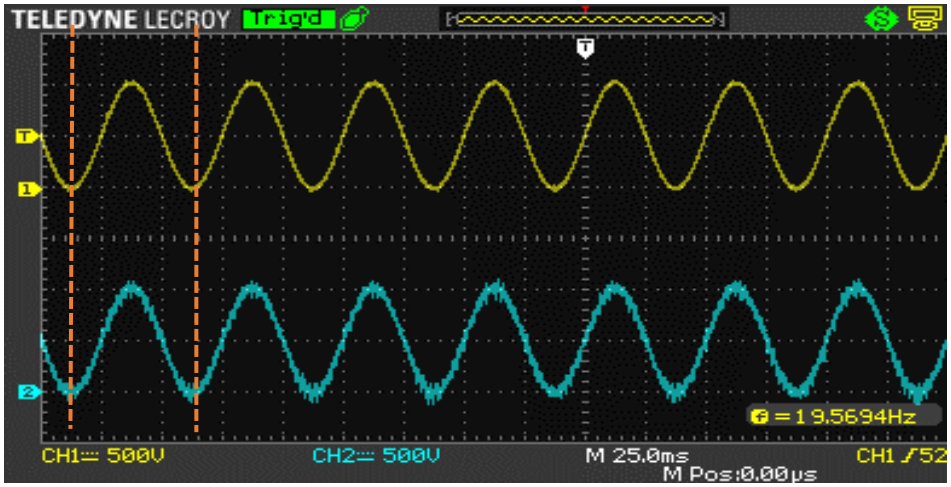


*Figure 23: 1kV DC, 2kV P-P, each division is 500V, frequency of 20Hz.*

## 4.9 Experimental details for the study of the effect of the mixing region and collector distance on microbubble formation coupled with AC-DC electric fields

Analysis of effect of AC voltage magnitude and frequency on the microbubble size indicated that frequency is an important factor in the microbubble size reduction. These findings suggest that higher frequencies can facilitate the formation of smaller microbubbles. The Ultravolt amplifier was replaced by a Trek amplifier (Trek 10/10B-HS, 464W, Lockport, New York, USA) in order to achieve higher frequencies to prove the hypothesis formulated in the initial investigation. The apparatus is schematically represented in figure 17.

One of the goals of this experiment was to vary the mixing region geometry denoted by $M_x$, and understand its role in the formation of microbubbles. In order to achieve this, $M_x$ was varied from $100\mu m - 200\mu m$, and the superimposed field was applied at the nozzle tip at a constant frequency and superimposed AC.

The experiments focusing on the mixing region geometry were conducted without the application of an electric field at the stainless steel outlet. Two different concentrations of Bovine Serum Albumin (BSA) were investigated as the liquid phase as shown in table 2.

Secondly, the effect of the electric field strength was investigated by altering the distance between the nozzle tip and grounded platform which will be referred to as $D_x$ herewith. The experiment was conducted using different values of $D_x$ ranging from $20 - 100\,mm$. The FEP and stainless steel capillaries were aligned in the aforementioned manner.

The junction gap size was set to $100\ \mu m$ as a significant reduction in bubble diameter was recorded when the junction area dimensions were the same as the inner diameters of the inlet and out capillaries owing to an increase in shear forces experienced at the junction area.

The experiments were conducted at $6\,kV\ DC$ and $8\,kV\ DC$ where the greatest microbubble size reduction and monodispersity was observed in the previous set of experiments. The superimposed AC voltage was retained at $2\ kV_{P-P}$. The frequency used was the optimal frequency from the first set of experiments that facilitated microbubble size reduction ( $2.2\ kHz$). The high voltage output from the amplifier is connected to the stainless outlet as shown in figure 20 by means of an alligator clip. The solution used for the experiments was a $10\ \%\ wt.$ solution of BSA as the occurrence blockages was lower, as opposed to the $15\ \%\ wt.$ solution which is of a higher viscosity thus requires the capillaries to be cleansed/replaced more frequently.

### 4.9.1 Description of equipment

The novelty of this experimental set-up is the amplifier incorporated which has a higher power output, therefore greater frequencies can be achieved by replacing the previously used amplifier in the experimental configuration.

A connection is made from the voltage input on the HVA to the frequency generator using a BNC connector. The signal is sent from the frequency generator to the amplifier whereby an input voltage of $0-10V$ is amplified to $0-10\ kV$. This input signal can be observed by connecting the voltage monitor output to the oscilloscope.

#### 4.9.1.1 High voltage amplifier

This experimental configuration is very similar to the previous described one; the Ultravolt amplifier is simply replaced by a Trek Amplifier (Trek 10/10B-HS, 464W, Lockport, New York, USA). This amplifier does not require an external low voltage power supply to drive the power inputs of the amplifier, as this is done internally.

This amplifier has a higher power output, therefore able to deliver higher frequency outputs at the load. Connections to the peripheral components

are made via BNC connectors therefore making this configuration simpler to connect and use than the previous experimental set-up.

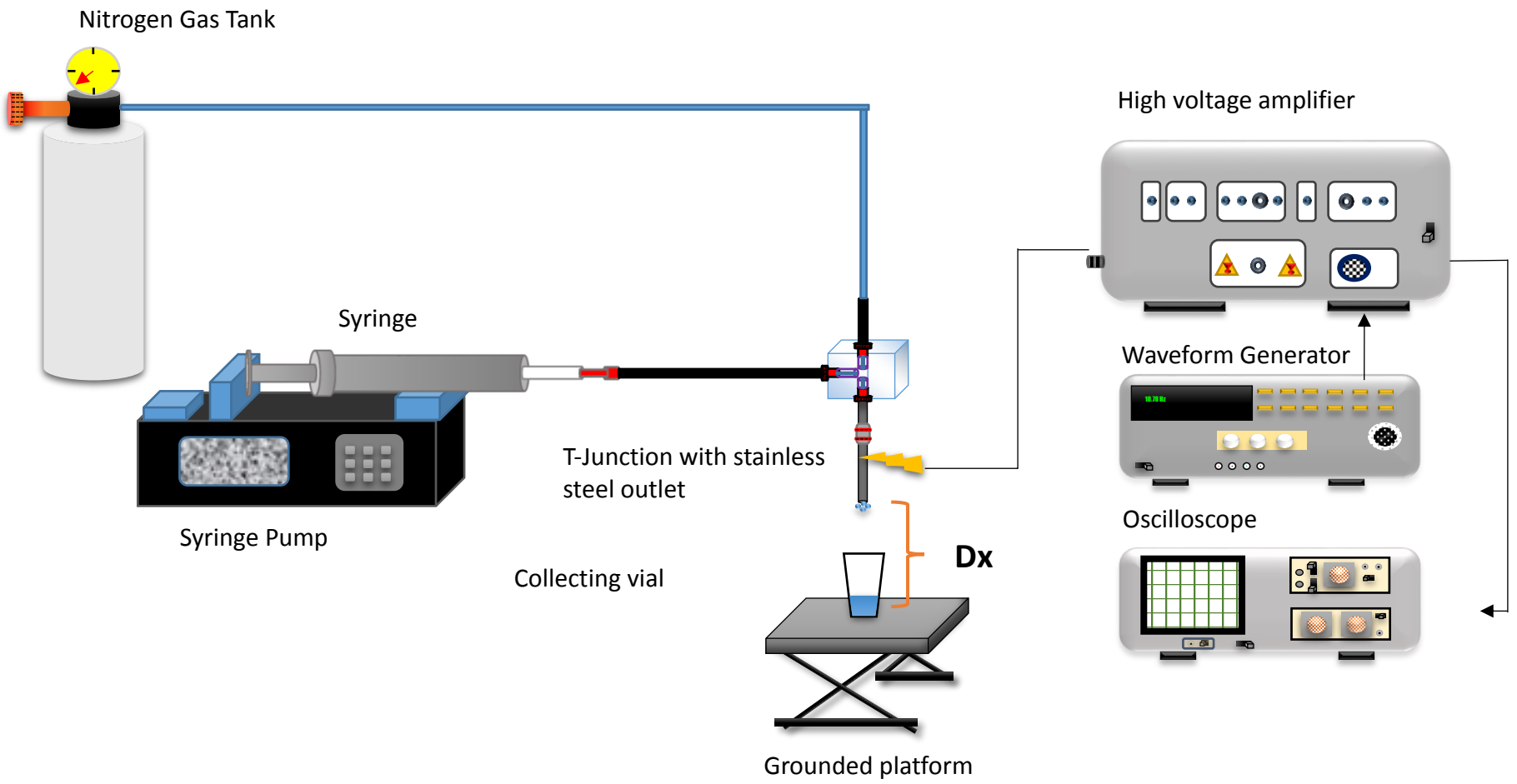


*Figure 24: Experimental set-up to superimpose AC on DC electric field using a HVA with a higher power rating, Dx indicates the distance between the nozzle tip and the collector.*

# 5.0 Experimental details for the study of the effect of the mixing region and collector distance on microbubble formation coupled with AC-DC electric fields

The purpose of this investigation was to harness the optimal processing parameters based on the results attained in sections 4.8 and 4.9 thus modify the geometrical configuration to facilitate the formation of uniform bubbles and achieve further control over the microbubble diameter. The experimental set-up used for this work is shown in figure 24. The T-Junction was arranged using two FEP tubes and a stainless steel capillary, $M_x$ was set to $100\ \mu m$ and $D_x$ was maintained at $400{,}000\ V/m$. A $10\ \%\ wt$. BSA solution was pumped into the junction at a constant volumetric flow rate, and Nitrogen was infused at a constant pressure. The effect of increasing the frequency with the optimised parameters was observed by increasing the frequency of the signal from $0 - 10\ kHz$ at $6\ kV\ DC$ and $8\ kV\ DC$. The superimposed AC voltage was set at a constant value of $2\ kV_{P-P}$ throughout the experiment. The results from the experiments conducted are discussed in detail in Chapter 5 of this thesis.

## 5.1 Characterisation of generated microbubbles

### 5.1.1 Optical microscopy

Microbubbles were collected on glass slides and observed immediately under an optical microscope (Nikon Eclipse ME 600, Nikon, Japan), it was fitted with a camera (JVC KY-F55B) to capture the micrographs. This arrangement was retained for the investigations described in chapter 5. The measurements were carried out using Image J digital imaging software (ImageJ 1.46r, National Institute of Health, Maryland, USA). The diameters of 50 bubbles were measured from the captured images for analysis.

### 5.1.2 High speed camera

The bubble formation is exemplified by obtaining high resolution videos using a high speed camera (Photron SA1.1, full frame resolution of 1024x1024 pixels). Three consecutive sets of videos were taken to observe the effect of the superimposed field on the forming meniscus. Videos of the meniscus at various applied DCs, superimposed AC and frequency were acquired. Steady coning of the jet was observed which is characteristic of electrohydrodynamic arrangements.

## 5.2 Integration between the numerical and experimental methods

Chapter 4 has discussed the various experimental configurations that have been developed and employed in this research, in addition, details regarding the solutions have also been discussed. A 2D computational model of the T-Junction employed in this work was constructed in order to investigate the hydrodynamic and electrohydrodynamic interactions in the presence of superimposed electric fields. The numerical methodology described in chapter 3 is employed by the CFD software to obtain contour plots that illustrate the phenomenon inside the junction, as a result of superimposed AC on DC electric fields. The experimental results are presented in chapter 5, followed by the numerical results in chapter 6.

# Chapter 5

## Experimental results and discussion

## 5.1 Novel preparation of monodisperse microbubbles by integrating oscillating electric fields with microfluidics.

### 5.1.1 Introduction

Microfluidics and electrohydrodynamics have been used separately to prepare microbubbles, and also in combination with AC or DC electric fields. Superimposed AC on DC fields have been used for the formation of droplets in electrohydrodynamic configurations however, to the best of the author's knowledge, the combination of superimposed AC on DC electric fields with microfluidics has not been reported in the literature.

There has been intense interest in microfluidic platforms in the past decade due to advancements made in developing economical and simple fabrication techniques such as soft lithography and wet etching (Ziaie et al., 2004). A major drawback of devices manufactured in this manner is the constant blockages of the flow channels especially when liquids of higher viscosity are infused into the channels necessitating an expensive cleaning process or rendering the device unusable such that a replacement is required (Parhizkar et al., 2013). Compared to these methods, the device utilised in this work offers an effective way to generate bubbles, providing the luxury of easily replacing capillaries in the event of a blockage.The main goal of this work was to develop a novel experimental setup to introduce a superimposed AC on DC electric field to a capillary embedded T-Junction and determine the effect of the variables such as AC and frequency on the

microbubble formation. Researchers (Parhizkar et al., 2014, Pancholi et al., 2008b) have combined microfluidic and electrohydrodynamic arrangements to prepare bubbles and particles, by solely utilising DC electric fields. The main limitation observed in these arrangements was that high voltages up to $20\ kV$ were required to facilitate the disintegration of microbubbles. A threshold voltage was identified beyond which did not contribute to the bubble break up or size reduction.

Aqueous glycerol solutions were chosen for the liquid phase as they have been widely used in experiments regarding flow phenomena (Glawdel et al., 2012, Christopher et al., 2009). It is shown that high AC voltage increase the bubble size, probably due to heating effects whereas subjecting a bubble to high frequencies close to its resonance frequency could accelerate bubble break-up.

### 5.1.2 Influence of superimposed AC on microbubble formation

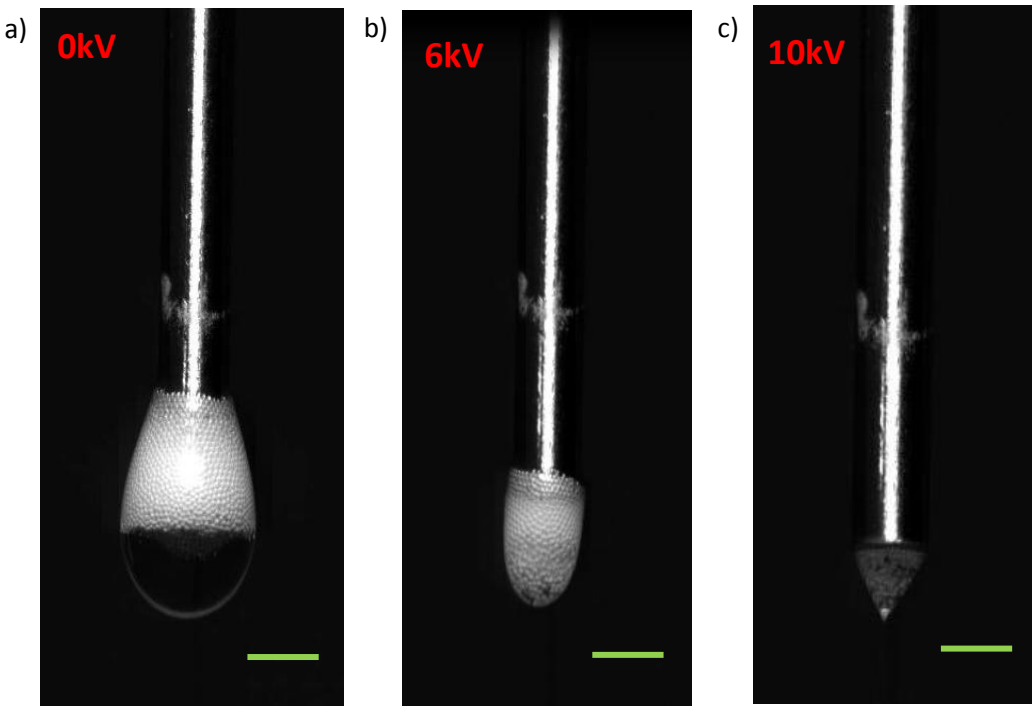


*Figure 25: High speed camera images of the microbubbles formed at the tip of the nozzle with a constant applied AC voltage of 2kVP-P, 10Hz at applied DC voltages of a) 0kV, b) 6kV, and c) 10kV . The scale bar is equivalent to a length of 1.6mm.*

Superimposing an AC field to a DC one, introduces three new parameters which are: (i) the waveform type, (ii) AC P-P Voltage and (iii) frequency. The effect of these parameters on the formation of microbubbles was investigated to develop an understanding regarding their effect on bubble diameter.

The first series of experiments were conducted by testing two different applied AC voltages – $2\ kV_{P-P}$ and $4\ kV_{P-P}$. For $2\ kV_{P-P}$, the waveform oscillates $1\ kV$ either side of the zero marker, and for $4\ kV_{P-P}$, the wave oscillates $2\ kV$ from $0$ to peak, and $0$ to trough. High speed camera images of the effect of the superimposed electric field on the liquid meniscus are shown in figure 25.

In the absence of an electric field, the droplet can be seen emerging from the tip of the capillary (figure 25a). This hemispherical shape is attributed to the surface tension of the liquid exceeding the weight of the droplet. Upon application of the oscillating field, the interface becomes polarised resulting in the deformation of the meniscus as observed in figure 25b. Increasing the applied voltage further to $10\ kV$ results in meniscus forming a conical shape as observed in figure 25c commonly referred to as a Taylor cone (Taylor, 1964). As the applied voltage is further increased, the surface tension is unable to retain the hemispherical structure and the liquid it encompasses. This results in the formation of a thin jet at the tip of the cone, which subsequently breaks into a jet of smaller bubbles as the tangential electric forces overcome the surface tension. In this experimental set-up, the formation of a stable Taylor cone and jet was initiated at $8\ kV$.

For the following experiments, a sinusoidal waveform with a frequency of $500\ Hz$ was used. The AC was modulated by varying the applied P-P voltage on the waveform generator. Once the P-P AC was set, the DC voltage was increased from $2\ kV$ up to $10\ kV$ by increasing the DC offset. Figure 26 shows optical micrographs of microbubbles obtained by progressively increasing the applied DC voltage. It can be seen that increasing the DC voltage at this superimposed AC voltage causes a drop in bubble diameter.

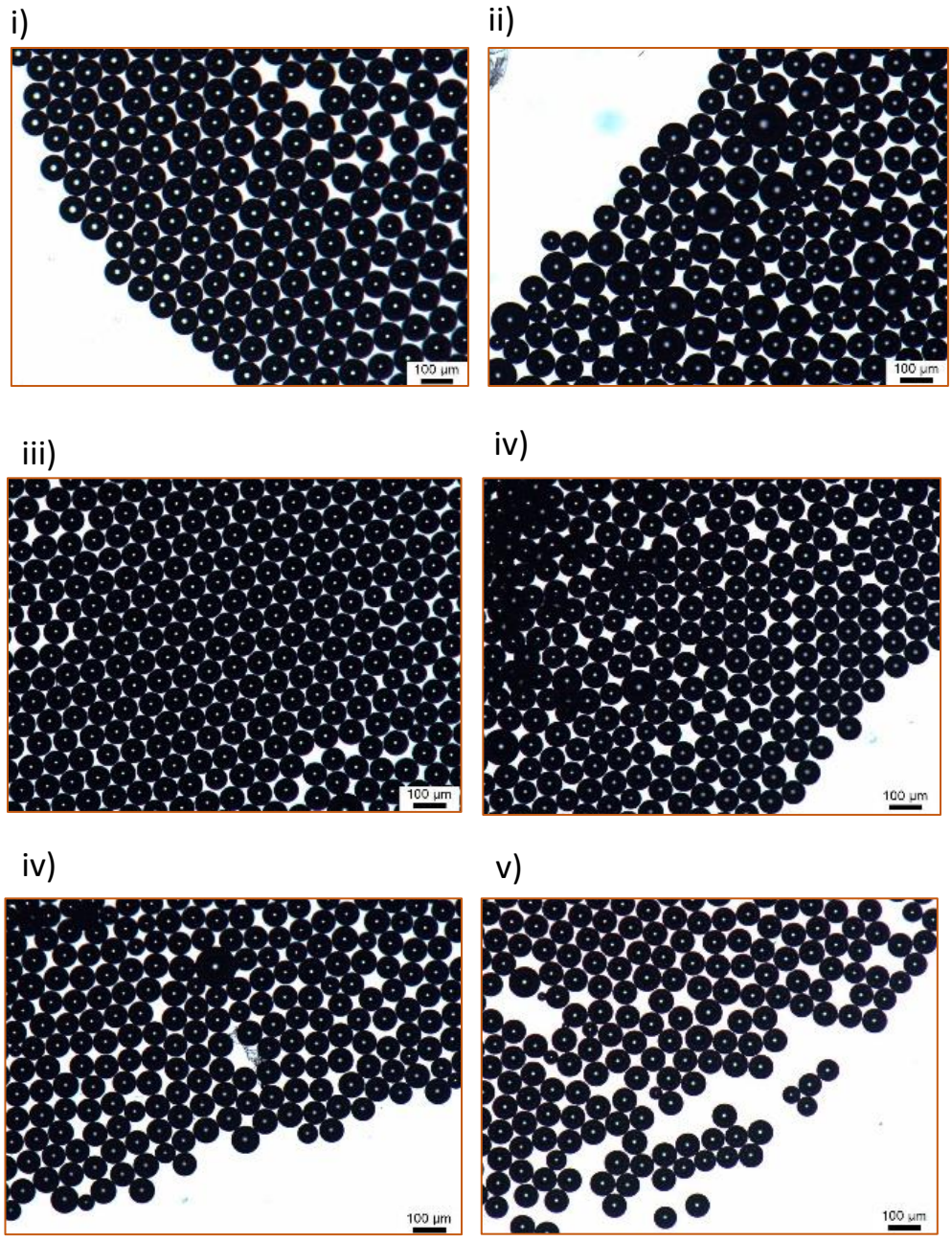


*Figure 26: Optical micrographs of bubbles obtained at a frequency off 500Hz, superimposed AC voltage of 2kV$_{P-P}$ at DC voltages of i) 0V, ii) 2kV, iii) 4kV, iv) 6kV, v) 8kV, vi) 10kV.*

On the other hand, increasing the AC voltage to $4\ kV$ (i.e, for an applied DC voltage of $8\ kV$, the waveform will oscillate between $6\ kV$ and $10\ kV$) , had the opposite effect on the bubble diameter as shown in figure 27 which suggests that the relationship between the bubble diameter to applied AC voltage is directly proportional. This phenomenon could be due to the prolonged exposure of the bubble to high AC fields combined with high frequency, which can ultimately result in the superheating of the bubble as reported by Cheng and Chaddock (Cheng and Chaddock, 1985). In their work

they describe that bubbles tend to grow under ambient conditions as a result of evaporation at the gas-liquid interface. Spheroidal structures tend to have a higher surface area than spherical ones, hence heat is conducted across the boundary of the bubble effectively.

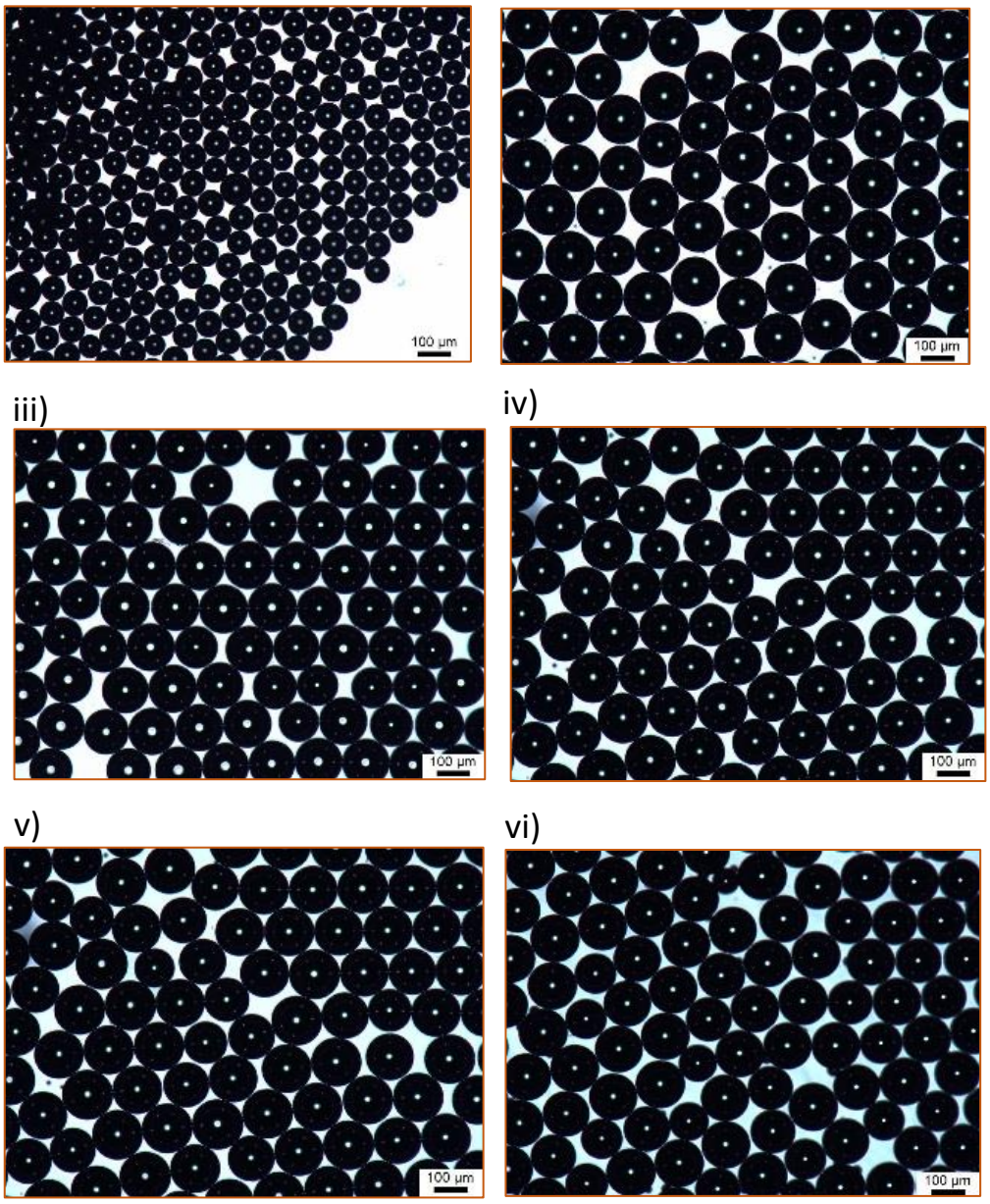


*Figure 27: Optical micrographs of microbubbles obtained at a frequency of 500Hz, superimposed AC voltage of 4kV P-P at DC voltages of i) 0kV, ii) 2kV, iii) 4kV, iv) 6kV, v) 8kV, vi) 10kV.*

Quan et al.(Quan et al., 2011) note that deformation of any kind, coalesence or bursting are caused by disturbances on the liquid/vapour boundary layer induced by the bubble oscillation caused by high AC fields. Kweon et al.

(Kweon et al., 1998) observed the effect on bubble dynamics when a high AC field was applied, and showed that rapid oscillations and subsequent droplet detachment ensued. They revealed that these rapid oscillations at high applied AC fields promoted electrohydrodynamic convection across the bubble surface.

Heat generated by high AC fields may have also contributed to heating effects which increase the overall bubble growth time. Gao et al.(Gao et al., 2013) verified that at a higher flux, the amount of time for the bubble to expand increases at the same applied voltage. In this work, it can be observed that lower AC voltages are optimal for the bubble formation as the overall bubble growth time is decreased. The effect of a superimposed AC is summarised in figure 28 suggesting that a lower superimposed AC voltage of 2kVP-P is optimal for this work.

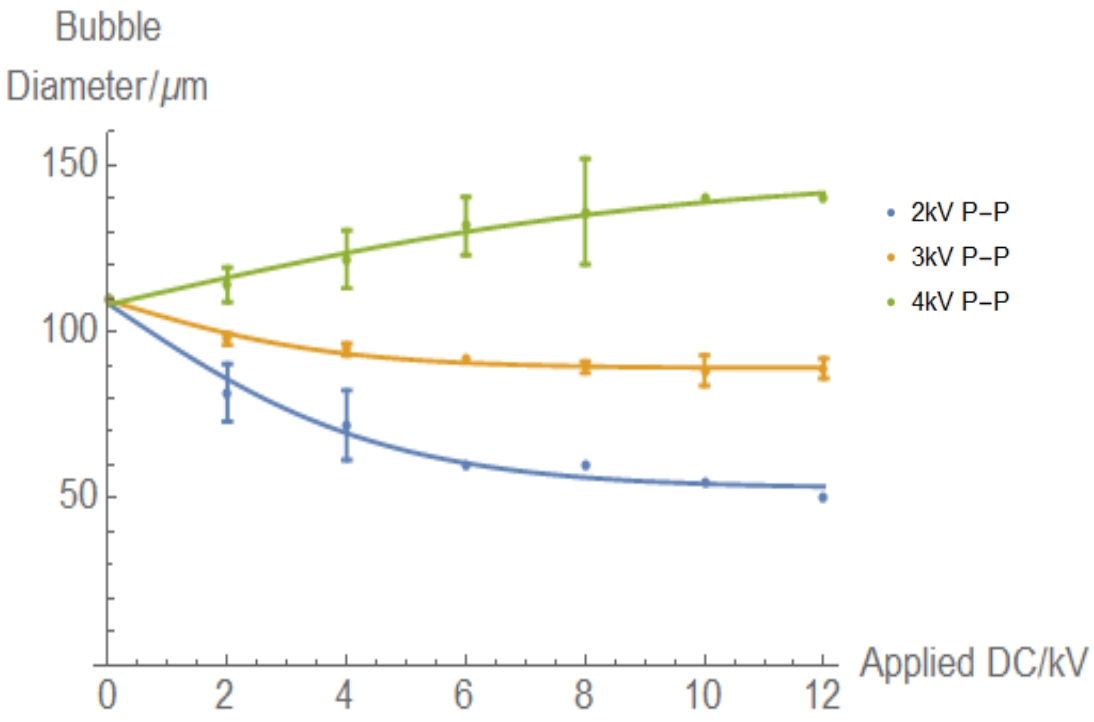


*Figure 28: Variation of microbubble diameter with applied DC voltage at different P-P AC voltages, error bars represent three standard deviations, estimated from repeat experiments. Curves represent a fit to a simple analytic function.*

### 5.1.3 Effect of applied frequency on microbubble dimeter

Figure 29 shows typical microbubbles obtained at a specific frequency at a constant superimposed AC voltage. Frequencies of $100\,Hz$, $500Hz$ and $600\,Hz$ were tested. Based on the results acquired for the effect of superimposed AC voltage on bubble diameter, an AC voltage of $2\,kV_{P-P}$ was maintained for all the experiments.

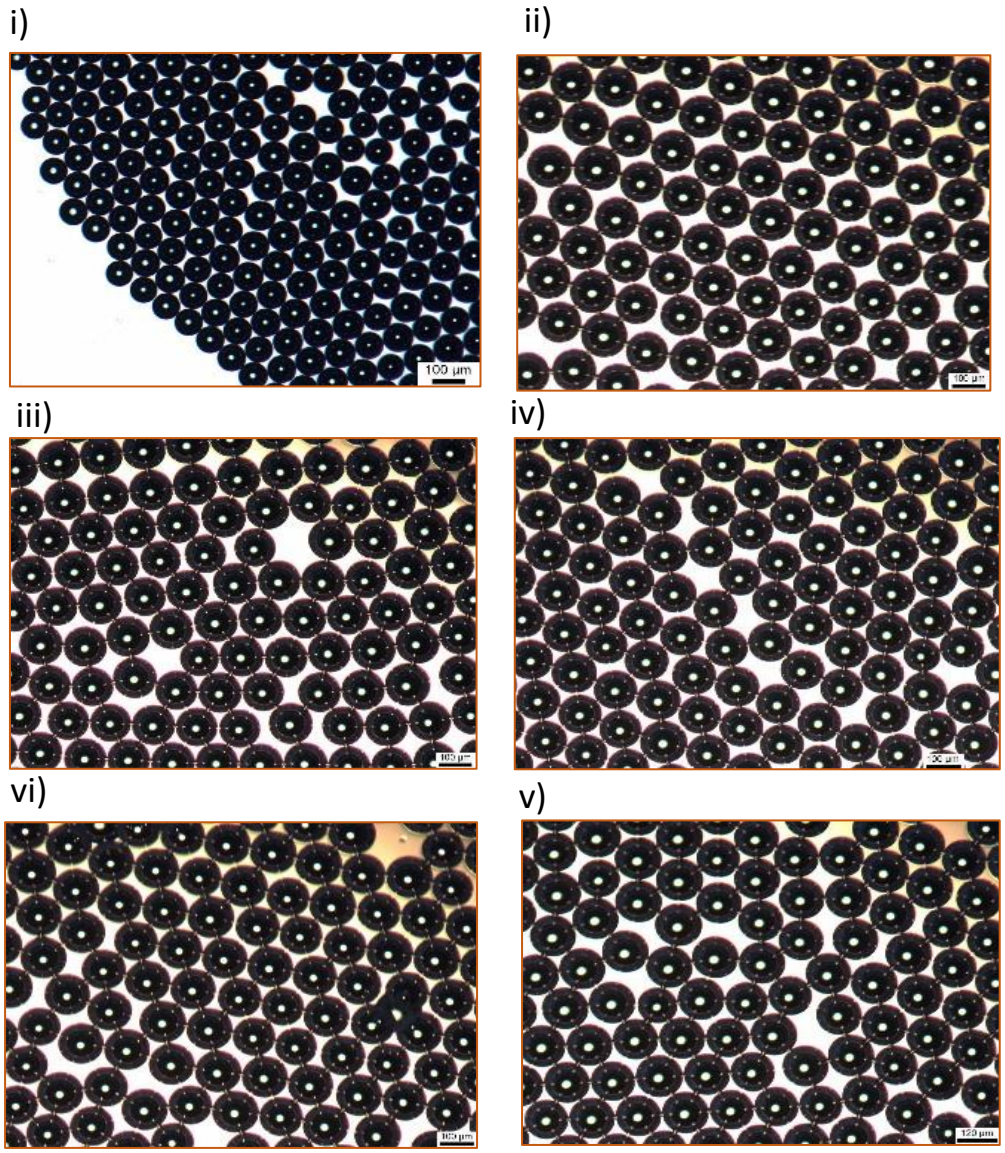


*Figure 29: Optical micrographs of bubbles obtained at a superimposed AC voltage of 2kV$_{P-P}$, 100Hz at applied DC voltages of i) 0V, ii) 2kV, iii) 4kV, iv) 6kV, v) 8kV, vi) 10kV.*

When a low frequency of $100\,Hz$ was utilised, the bubble diameter dropped

from $110\ \mu m$ to $100 \pm 0.60\ \mu m$ as the applied DC voltage was increased in increments of 2 -12 $kV$.

Increasing the applied frequency to $500\ Hz$ (figure 30) resulted in a drop in bubble diameter from $110\ \mu m$to $55 \pm 1.15\ \mu m$ when the applied DC voltage was increased from $0 - 12\ kV$ in steps of $2\ kV$. Microbubbles acquired at $6\ kV$ (figure 30 iv) displayed near-perfect monodispersity.

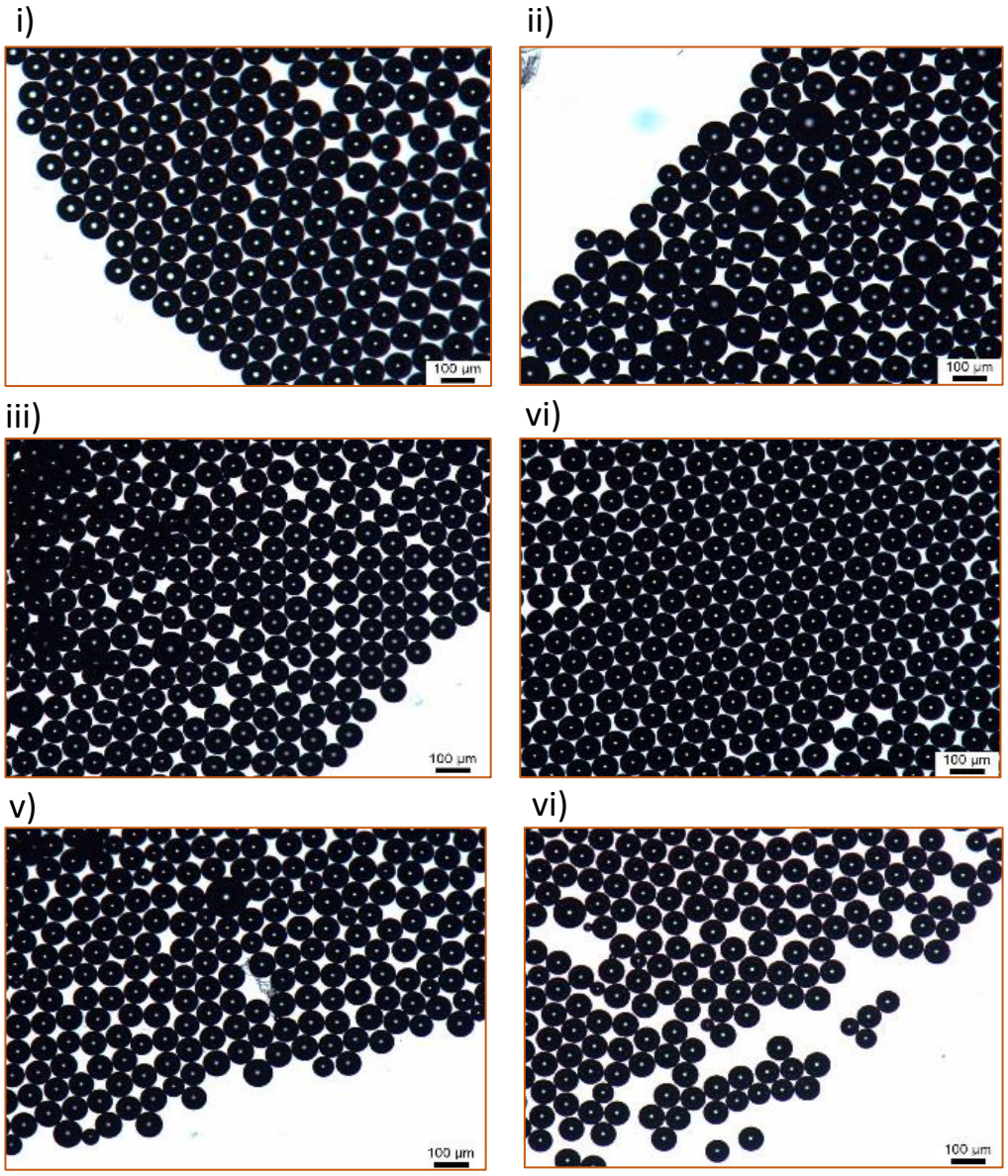


*Figure 30: ) Optical micrographs of bubbles obtained at a superimposed AC voltage of 2kVP-P, 500Hz at applied DC voltages of i) 0V, ii) 2kV, iii) 4kV, iv) 6kV, v) 8kV, vi) 10kV.*

Increasing the frequency to $600\ Hz$ displayed interesting results, at an applied DC voltage of $8\ kV$(figure 31 v), the bubble size was recorded to be $38 \pm 1.15\ \mu m$, but increasing the voltage further past this point resulted in

a foam-like cluster as shown in figure 31vi). This coalescence is likely to be due to the effects of heating in the presence of high electric fields as pointed out by Gao et al. (Gao et al., 2013).

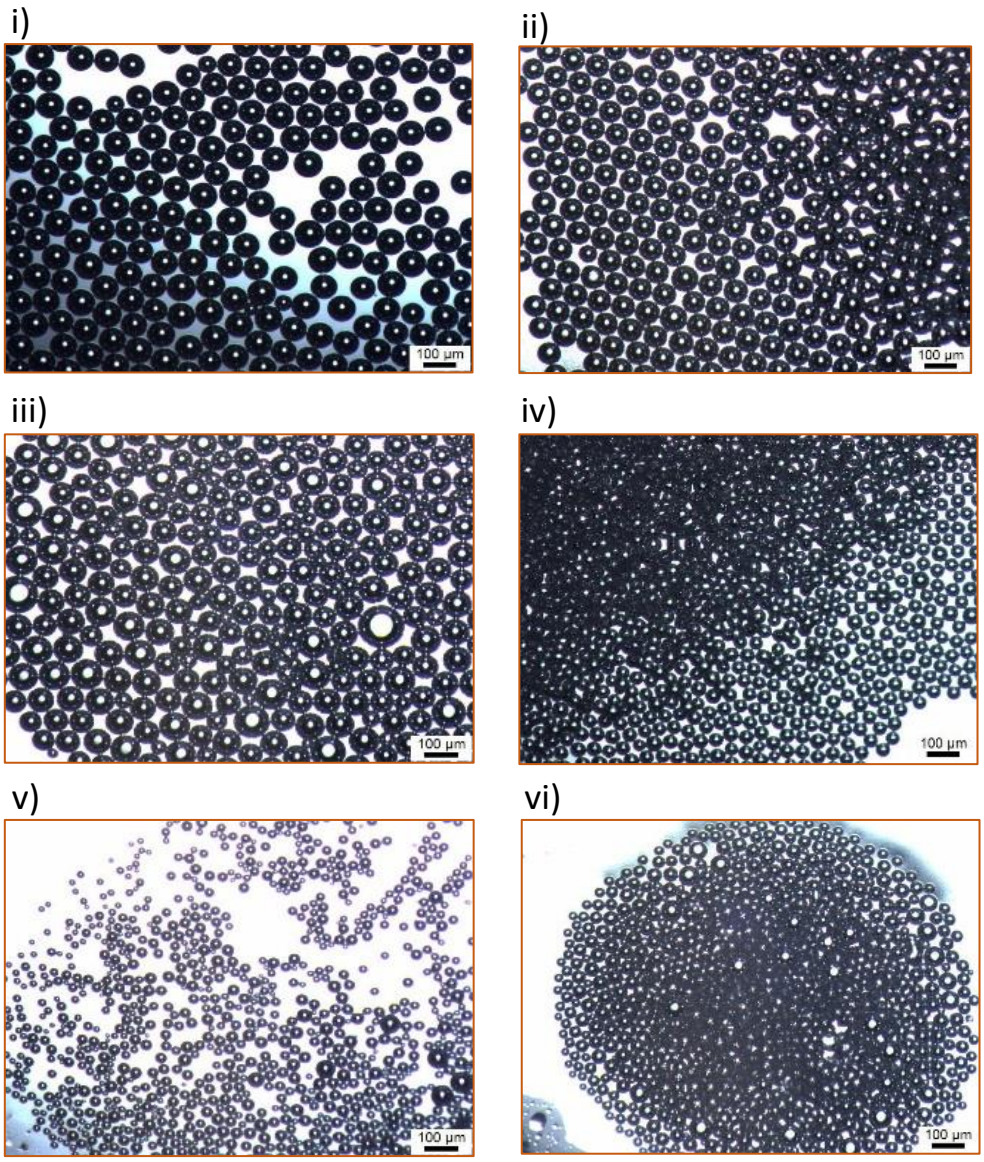


*Figure 31: Optical Micrographs of bubbles obtained at a superimposed AC voltage of 2kV P-P, 600Hz at applied DC voltages of i) 0V, ii) 2kV, iii) 4kV, iv) 6kV, v) 8kV, vi)10kV.*

From the results presented, it can be seen that frequency is a key parameter in these studies. As the frequency is increased, there is a clear and significant decrease in microbubble diameter by $\sim 50\%$, as shown in figure 32. We investigated this phenomenon in greater detail by increasing the frequency

to $2.2\ kHz$. $6\ kV\ DC$ displayed consistent bubble reduction and monodispersity, hence was chosen as a constant for this experiment.

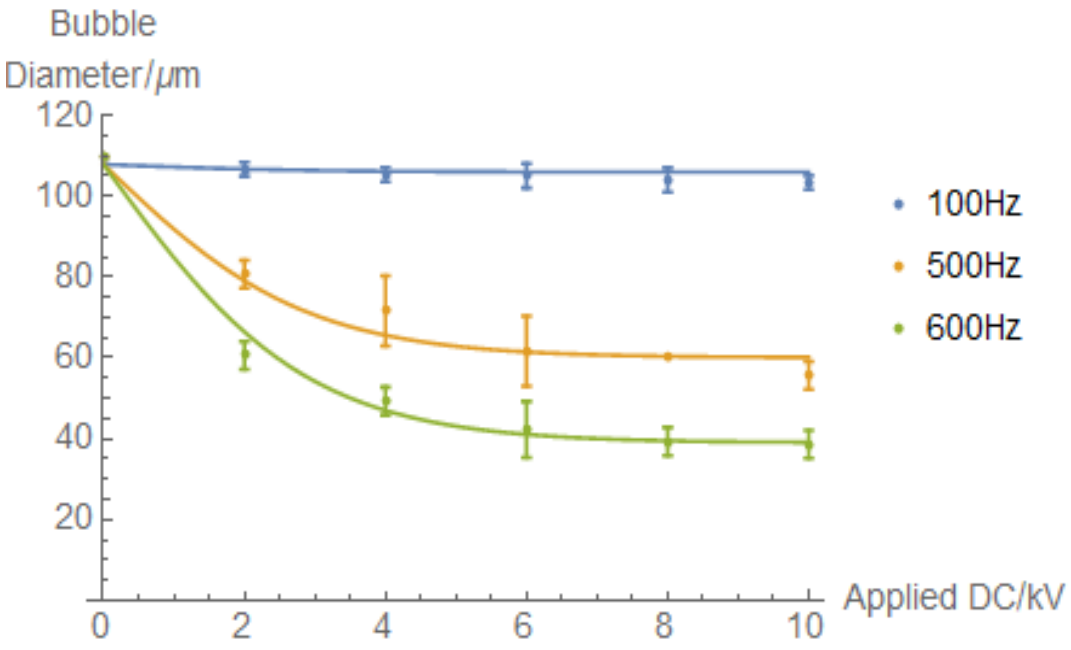


*Figure 32: Effect of applied AC electric field frequencies on the microbubble diameter. Error bars represent tree standard deviations, estimated from repeat experiments. Curves represent a fit to a simple analytic function.*

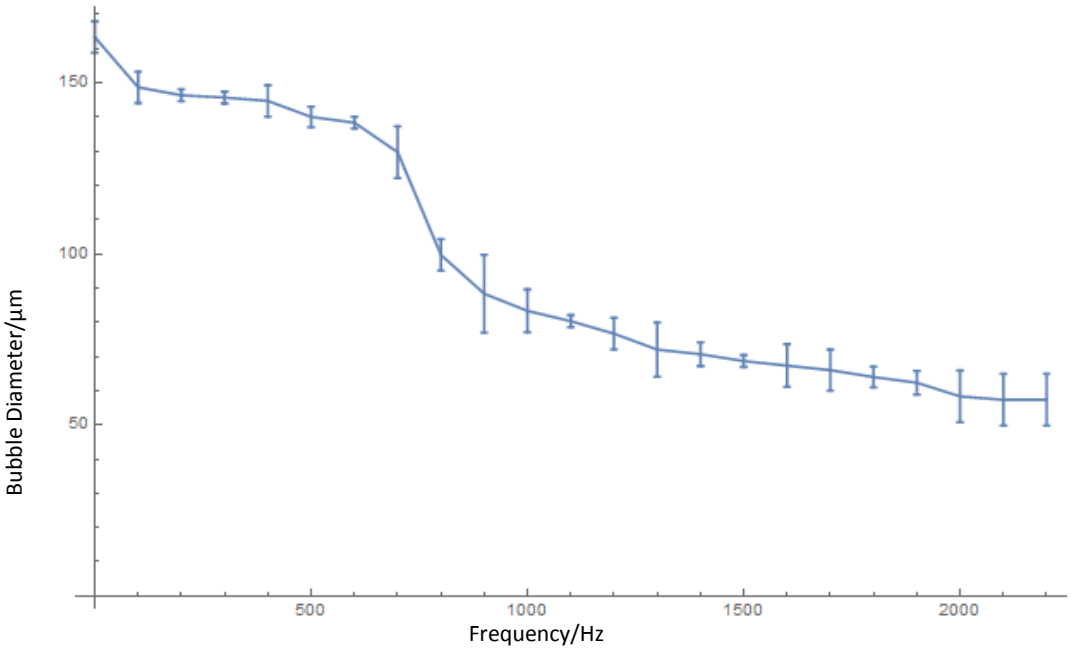


*Figure 33: Variation of microbubble diameter as a function of frequency at 2kV P-P AC voltage, 6kV DC Voltage, error bars represent three standard deviations, estimated from repeat experiments. Measured points are connected by straight line segments as a guide to the eye.*

From figure 33, it can be observed that the applied frequency results in the decline of microbubbles as it is increased to $2.2\,kHz$. A microbubble diameter reduction of $170 - \ 138 \pm 0.58\ \mu m$ was observed between $100 - 600\ Hz$. A decline in bubble size from $138 \pm 0.58\ \mu m - 99 \pm 1.53\ \mu m$ was observed between $600 - 800\ Hz$ and $99 \pm 1.53\ \mu m\ - 57 \pm 2.51\ \mu m$ was observed between $800 - 2200\ Hz$. These results are indicative of a complex system which is subjected to various parameters that are non-linear in nature. The sudden drop in bubble diameter observed in figure 33 between $600 - 900\ Hz$ can be possibly attributed to the resonance of the bubble of that diameter as a result of the applied frequency. When in the presence of a sound field, a bubble has been shown to vibrate or resonate non-linearly. For example, in order to reduce the bubble to size $2\ \mu m$, a frequency of the order of $10\,MHz$ may be required (Lastow and Balachandran, 2007), this is very similar to the resonance frequency of a microbubble of that size. The resonance frequency is given by Minnaerts' theory (Leighton, 2012):

$$f_M = \frac{1}{R_0 2\pi}\sqrt{\frac{3\gamma p_0}{\rho}} \qquad (5.1)$$

where $f_M$ is the Minnaert resonance frequency, $\rho$ the density of surrounding liquid, $\gamma$ is the polytrophic constant, $p_o$ is the hydrostatic pressure outside bubble and $R_0$ is the equilibrium bubble radius. However this is neglecting the effect of surface tension which is an important contributor to microcapillary flow. Plesset and Prosperetti (Plesset and Prosperetti, 1977) developed a more accurate expression taking to consideration the effects of surface tension on the flow:

$$f_0^2 = \frac{1}{2\pi^2}\left[3\gamma\frac{p_0}{\rho R_0^2} - \frac{2\sigma}{\rho R_0^3}\right] \qquad (5.2)$$

where $f_0$ is the resonance frequency, $p_o$ is the equilibrium pressure and $\sigma$ is the surface tension. Although this equation acknowledges the effect of surface tension, it cannot be utilised to provide an accurate correlation of the system documented in this work without an electrohydrodynamic source term in the expression. However, what can be deduced from this expression is that the resonance frequency is inversely proportional to the bubble radius, therefore a reduction in bubble size consequently increases the resonance frequency of the bubble. The applied DC voltage causes the elongation of the fluid stream, and the AC excitation facilitates bubble break-up.

### 5.1.4 Summary

A novel experimental set-up was developed in order to superimpose an AC electric field onto a DC electric field. This introduces new variables such as applied AC and frequency which were investigated in detail. The experimental set-up allows the superimposition of an AC on DC by adjusting the offset on the waveform generator. It was observed that increasing the applied AC results in the formation of larger microbubbles possible due to heating effects. On the other hand, increasing the frequency resulted in a decrease in microbubble diameter. The distinctive drop in bubble diameter observed in figure 33 between $600 - 900\ Hz$ is possibly attributed to the resonance of a bubble of that diameter as a result of the applied frequency, as suggested by Minnaert's theory for resonance. The results acquired suggest that the bubble size can potentially be further reduced by utilising higher frequencies, allowing for better control over the microbubble size.

## 5.2 Effect of the mixing region geometry and collector distance on the microbubble formation coupled with AC-DC electric fields.

### 5.2.1 Introduction

The effect of solution properties and various processing parameters have been investigated on bubble formation such as gas pressure and liquid flow rate. This has been conducted with respect to both microfluidic and electrohydrodynamic configurations, however not much relevance has been given to mixing region where both fluid media interact. Literature has implied that bubble break up is facilitated by the shear forces experienced at the junction (Garstecki et al., 2006). In this study we aim to investigate the effect of the mixing region geometry on the microbubble which can be achieved by reducing the surface area at mixing region.

In electrohydrodynamic arrangements such as electrospraying and electrospinning, the tip-to-collector distance plays a significant role in the morphology of the fibres, particles or droplets that are formed (Ding et al., 2002, Zheng et al., 2006). One of the reasons for this occurrence is that varying the distance between the ground and the point where the electric potential is applied influences the strength of the electric field. To the best of the author's knowledge, the effect of the electric field strength on the formation of microbubbles in the presence of oscillating electric fields has not been reported in the literature.

Bovine Serum Albumin (BSA) of two different concentrations were prepared for the experiments discussed in the following sections. BSA has been used for various biomedical avenues such as echo contrast agents and in drug delivery as it benefits from low cost and similarity to human serum albumin and is available in abundance (Grinstaff and Suslick, 1991, Elzoghby et al., 2012, Kurrat et al., 1997). These attributes justify the suitability of BSA for the experiments detailed below.

Based on the parameters that facilitate the reduction in microbubble diameter, the experimental set-up was optimised to elucidate the parameters that are required to tailor the bubble diameter as desired.

### 5.2.2 Effect of the mixing region geometry on microbubble formation

The mixing region geometry $M_x$ was varied by altering the distance between the top inlet and the stainless steel capillary between $100\ \mu m - 200 \mu m$. The effect of varying $M_x$ on the bubble diameter was investigated using two different concentrations of BSA. The first series of experiments were conducted using $15\ \%\ wt.$ concentration of BSA. A constant gas pressure of $106.7\ kPa$ and a liquid flow rate of $130\ \mu l/min$ was retained for all values of $M_x$.

Figure 34 depicts optical micrographs of microbubbles collected at various $M_x$ values using a 15% wt. BSA solution; it can be observed that there is a constant and progressive decrease in diameter with decreasing $M_x$. The microbubbles produced at an $M_x$ distance of $200\ \mu m$ were $128\ \pm 3.05\ \mu m$, when $M_x$ is reduced to $160\ \mu m$, the bubble size was reduced to $98 \pm 1.52\ \mu m$. Setting the gap distance to $100\ \mu m$, in line with the inner diameter of all the tubes facilitates the size reduction, yielding microbubbles of $71\ \pm 4.04\ \mu m$. However, due to the higher viscosity of the solution, blockages within the FEP tubes occurred frequently. Therefore, requiring regular replacement of the FEP tubes. .

The experiments were repeated using a $10\ \%\ wt.$ BSA solution, the optical micrographs obtained at different values of $M_x$ are shown in figure 35. Similar to the trend displayed in figure 34, a solution of $10\ \%\ wt.$ displays a more refined and steady decrease in bubble size as shown in figure 35. When $M_x$ is reduced from $200\ \mu m$ to $140\ \mu m$, a microbubble diameter reduction from $128 \pm 2.64 \mu m$ to $108\ \pm 1.00 \mu m$ is observed. Setting the gap size to $100\ \mu m$, promotes a further descent in bubble diameter to $88\ \pm 5.65 \mu m$.

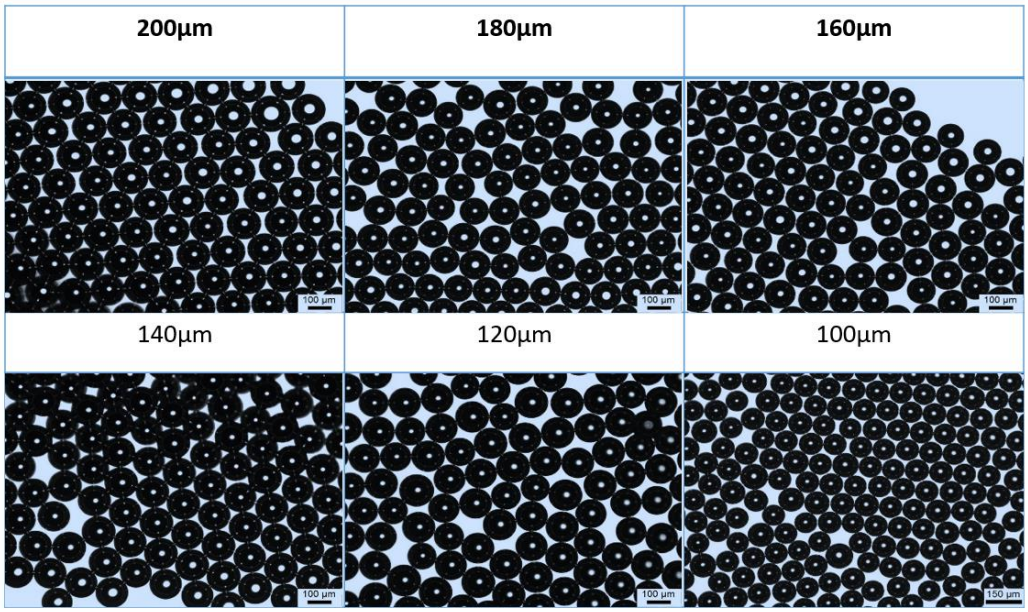


*Figure 34: Optical Micrographs of bubbles of 15% BSA obtained at Mx of a) 200µm, b) 180µm, c) 160µm, d) 140µm, e) 120µm, and f) 100µm.*

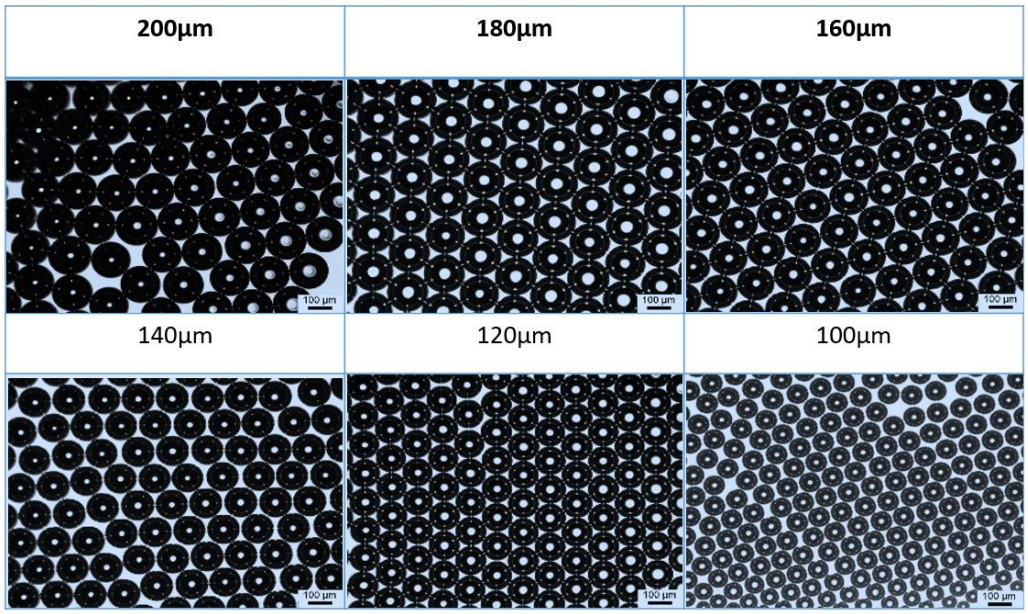


*Figure 35: Optical Micrographs of bubbles of 10% BSA obtained at Mx of a) 200µm, b) 180µm, c) 160µm, d) 140µm, e) 120µm, f) and 100µm.*

Parhizkar et al.(Parhizkar et al., 2013) suggested that a greater decrease in microbubble diameter when a solution of a higher viscosity was used as the liquid phase was due to the relative increase in the shear force over the capillary force at the channel junction. Microflows are characterised by low Reynolds numbers (Garstecki et al., 2006) for the liquid:

$$Re = \frac{Q_l \rho_l}{\mu_l D} \quad (5.3)$$

And for the gas:

$$Re = \frac{Q_g \rho_g}{\mu_g D} \quad (5.4)$$

where $Q_l$, $\rho_l$, $\mu_l$, $Q_g$, $\rho_g$, $\mu_g$ and $D$ are the volumetric flow rate of the liquid, liquid density, dynamic viscosity of the liquid, volumetric flowrate of the gas, gas density, dynamic viscosity of the gas and the hydraulic diameter of the capillaries respectively), hence the flow is laminar and the fluid flow is governed by viscous forces rather than inertial forces. This indicates that altering either gas pressure or liquid flow rate will have an impact on the bubble size.

The FEP tubes utilised in these experiments have a hydraulic diameter of 100µm, Garstecki et al.(Garstecki et al., 2006) elaborated that flows through microchannels of these dimensions typically have very low capillary numbers ( $Ca < 10^{-2}$):

$$Ca = \frac{\mu u}{\gamma} \quad (5.5)$$

where $u$ is the average velocity of the continuous phase and $\gamma$ is the interfacial tension); therefore the size of the bubbles produced is governed by the pressure balance between the gas and the liquid. The emerging droplet/slug occupies the entire channel geometry leading to an increase of pressure upstream, which consequently leads to bubble growth and a

generation of a neck where the bubble is trying to pinch off from the continuous phase. Baroud et al. (Baroud et al., 2010) added that droplet break-up occurs when the viscous shear stress overcomes the surface tension that retains the curvature of the emerging bubble.

This suggests that an increase in viscosity further increases this shear force at the junction area, thus resulting in the formation of smaller bubbles. Based on these theories, decreasing the value of $M_x$, consequently reduces the surface area which also results in an increase of the shear force across the mixing region in the junction contributing the formation of smaller bubbles. A summary of the bubble size with different values $M_x$ for both concentrations of solution is shown in figure 36.

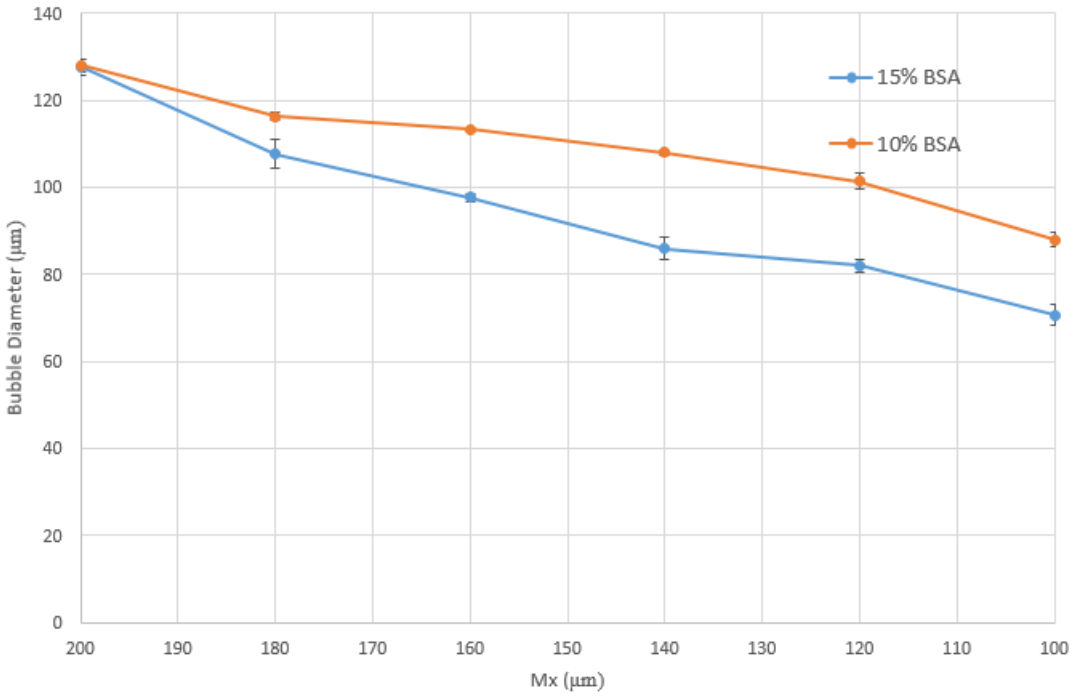


*Figure 36: Graph of Bubble Diameter versus Mx for 15% wt. and 10% wt. BSA Solutions.*

### 5.2.3 Effect of electric field strength on microbubble formation

Bubble size reduction experiences limitations in experimental configurations without external electric fields. Electrohydrodynamic techniques have also been used to generate microbubbles using a dual needle configuration called coaxial electrohydrodynamic atomisation (CEHDA) (Ahmad et al.,

2008). This allows the formation of multi-layered bubbles, particles and capsules. Electrohydrodynamic theory encompasses the behaviour of a liquid stream when subjected to an electric field (Zeleny, 1914). When the liquid stream reaches the nozzle, the hemispherical meniscus is held together by interfacial tension which Zeleny (Zeleny, 1914) described by the following equation:

$$\sigma = \frac{rh\rho g}{2} \tag{5.6}$$

where $r$ is the radius of the nozzle, $h$ is the height of the liquid required to cause the hemispherical shape of the meniscus and $g$ is the acceleration due to gravity. When an electric field is applied at the nozzle, the liquid is gradually charged up, and the electric field intensity $(f)$ experienced at the liquid surface is given by:

$$f = \sqrt{8\pi x\rho g} \tag{5.7}$$

where $x$ is the length of the liquid column whose hydrostatic pressure counteracts the elongation caused by the electric field acting on the liquid surface. Once the electric field overcomes the interfacial tension, the meniscus releases a thin jet to produce fibres or breaks up to form fine droplets.

Introducing an electric field in the form of a steady state DC constrained the parameter manipulation to only variation of the applied DC voltage (Parhizkar et al., 2014). In that case, Parhizkar et al. (Parhizkar et al., 2014) observed significant bubble reduction at very high voltages of $12\ kV$. This may be due to the fact that the distance between the ground collector was

$100mm$ generating a lower electric field strength($120{,}000\ V/m$), therefore requiring very high DC voltages to compensate for this.

Figure 37 displays optical micrographs of microbubbles obtained at $6\ kV\ DC$, $2\ kV_{P-P}$, $2\ kHz$. The bubble size was observed to reduce with decreasing $D_x$. Reducing $D_x$ from $100\ mm$ to $80\ mm$ results in the average microbubble diameter decreasing from $111 \pm 1.53\mu m$ to $101.67 \pm 2.88\mu m$, which further decreases to $\sim 86.33 \pm 1.53\mu m$ when the DC electric field strength is $300{,}000\ V/m$ ($D_x = 20mm$).

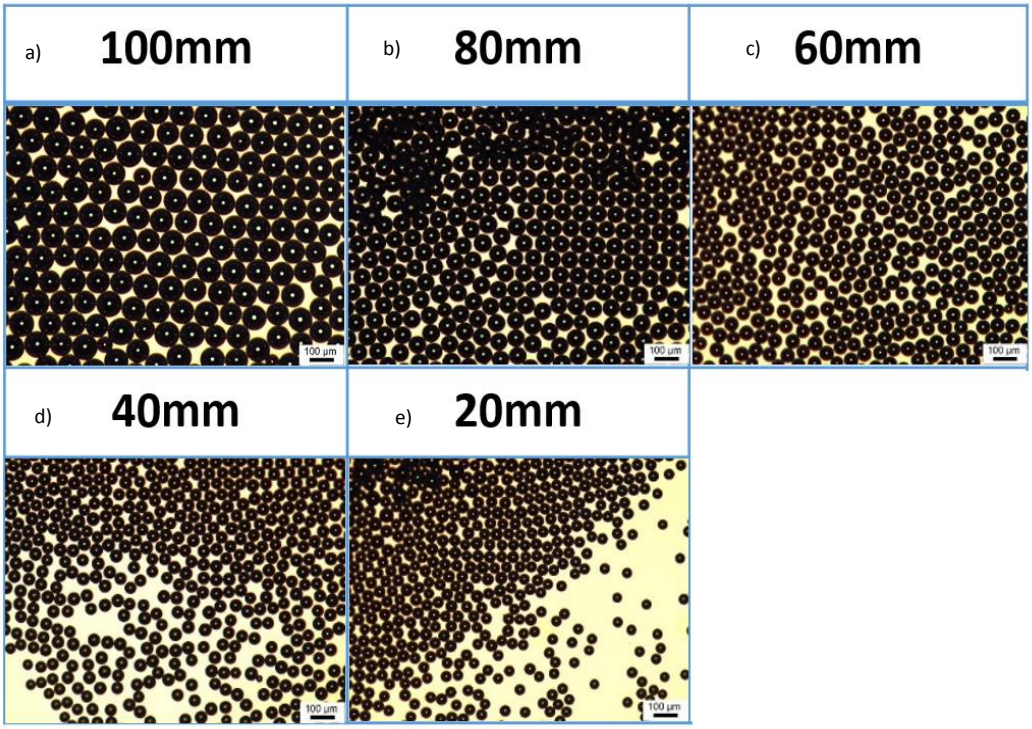


*Figure 37: Effect of varying Dx at 6kV DC, 2kV AC P-P, 2kHz. A 10% BSA solution was used in the experiments, and Dx values are a) 100mm, b) 80mm, c) 60mm, d) 40mm, e) 20mm.*

A similar phenomenon was observed when the applied DC was increased to 8kV DC (figure 38) keeping the other parameters constant. The microbubble size decreased from $111.33 \pm 1.53\mu m - 97.33 \pm 2.08\mu m$ at a $D_x$ value of $20\ mm$. A roughly similar drop in bubble diameter was recorded at a $D_x$ value of $80\ mm$ when a DC voltage of $6\ kV$ was employed. The results for $6\ kV\ DC$ and $8\ kV\ DC$ are summarised in figure 39.

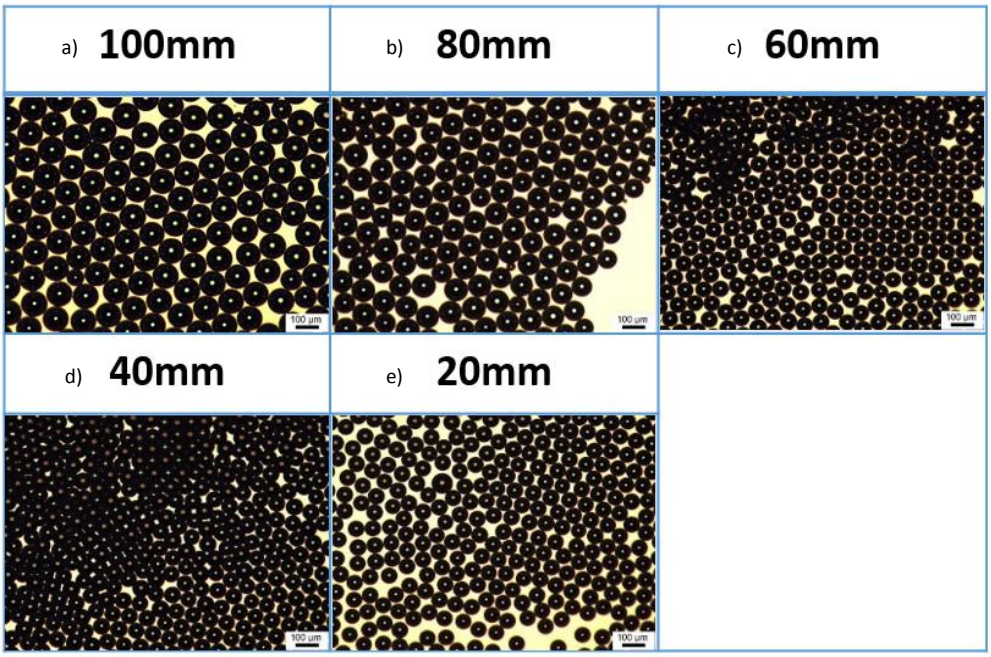


*Figure 38: Effect of Dx at 8kV DC, 2kV AC P-P, 2kHz. A 10% BSA solution was used in the experiments, and Dx values are a) 100mm b) 80mm c) 60mm d) 40mm e) 20mm*

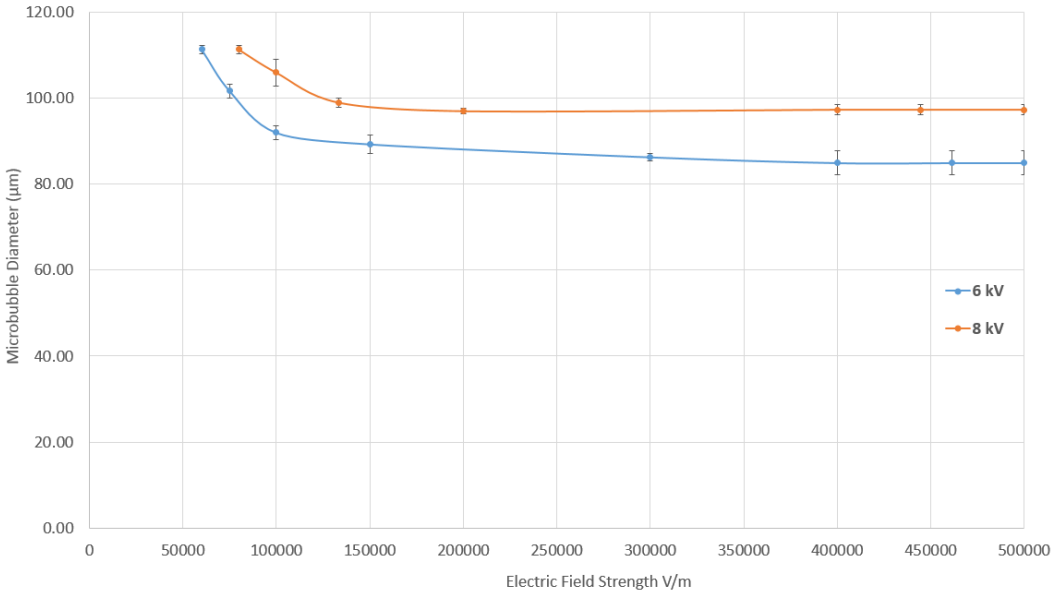


*Figure 39: Graph summarising the effect of the electric field at 6kV DC and 8kV DC at 2kV AC P-P, 2 kHz for 10%wt. BSA Solution*

A DC electric field strength of $100{,}000\ V/m$ can be achieved at $6\ kV$ and $8\ kV$ by setting the tip-collector distance at $60mm$ and $80mm$ respectively. The microbubble diameter decreased from $111.33 \pm 1.53\mu m$ to $92.00 \pm$

$2.64\mu m$, displaying a $17.36\%$ reduction in size with an absolute DC voltage magnitude of 6kV. On the other hand, a decrease in size from $111.33 \pm 1.53\mu m$ to $106.00 \pm 5.29\mu m$ was recorded at a DC voltage magnitude of $8\ kV$ displaying a $4.29\%$ decrease. Similarly, at an e-field strength of $500{,}000\ V/m$, requires $D_x$to be $12mm$ and $16mm$ at $6kV$ and $8kV$ respectively. A $23.65\%$ decrease in the MB diameter was observed at $6\ kV$ and a $12.58\%$ decrease at $8kV$. These observations indicate that the variation in bubble size is influenced partly by the applied absolute DC voltage magnitude and the DC electric field strength. Smaller bubble sizes can be achieved at lower absolute DC voltage magnitudes by adjusting the tip-to-collector distance to increase the electric field strength.

### 5.2.4 Effect of the optimised parameters on microbubble formation

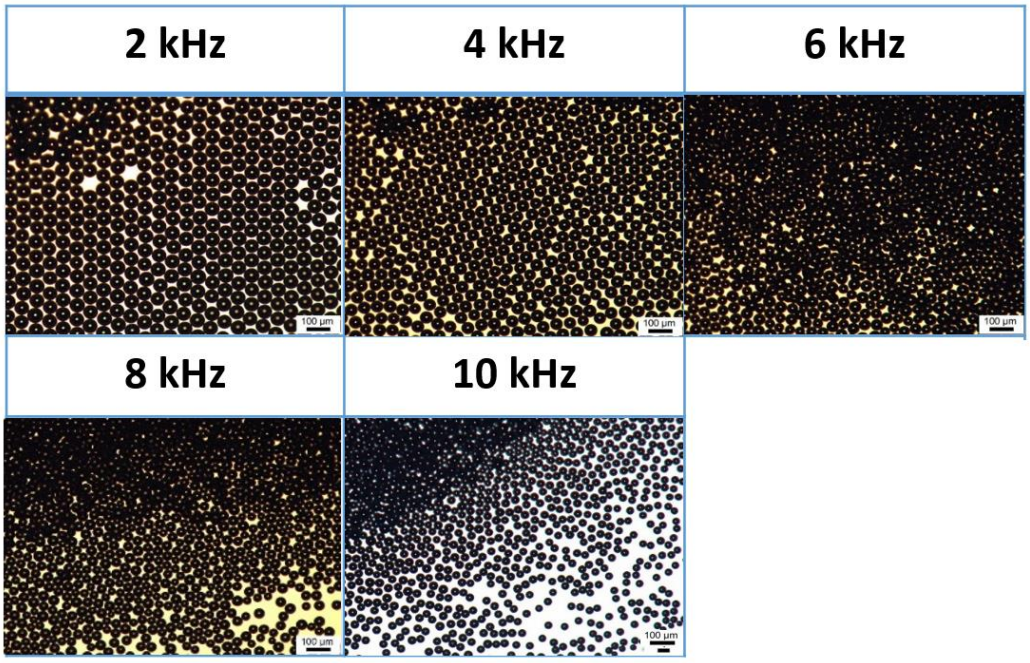


*Figure 40: Optical Micrographs at 6kV at frequencies of a) 2 kHz b) 4kH c) 6kHz d) 8kHz and e) 10kHz*

From figure 39, it can be observed that the greatest reduction in microbubble diameter was at $400{,}000V/m$. The ideal parameters for microbubble reduction obtained in the previous invesitigations, were

incorporated for the next set of experiments using $10\ \%\ wt.$ BSA, $M_x = 100\mu m$ and $D_x = 400{,}000\ V/m$. The experiments were conducted at a constant applied AC voltage of 2kV (P-P) and varying the frequency between $1\ kHz - 10\ kHz$ at an applied DC voltage of $6\ kV$. The corresponding optical micrographs obtained are presented in figure 40. It can be observed by incorporating the optimised parameters and steadily increasing the applied frequency further causes a reduction of $111 \pm 1.53\mu m$ to$18 \pm 2.08\mu m$). This is presented in figure 41.

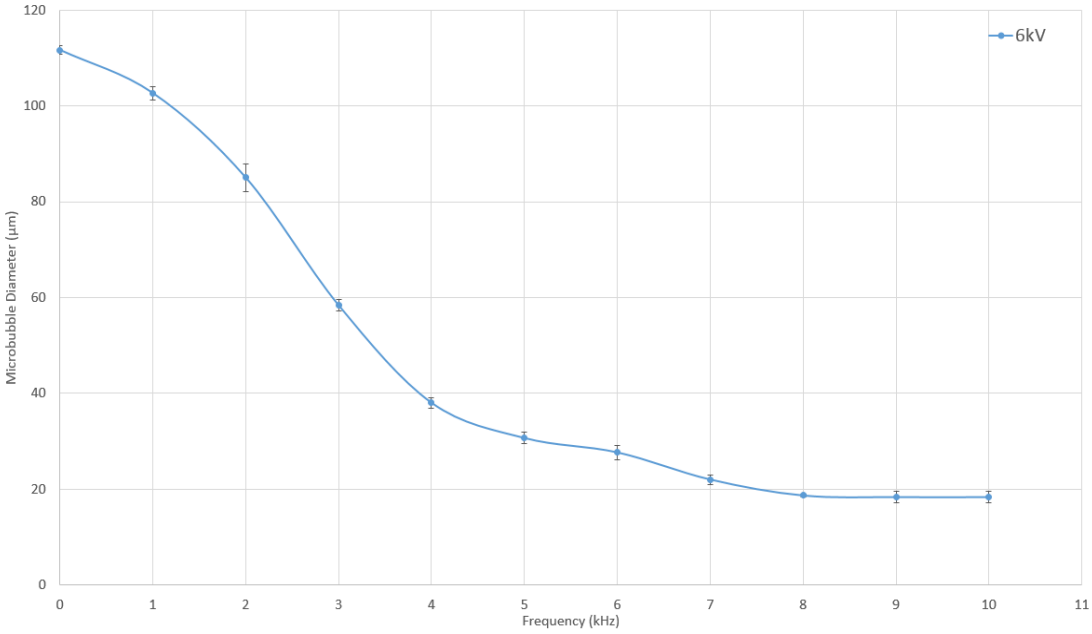


*Figure 41: Graph summarising the effect of frequency on microbubble diameter with optimised parameters of Mx= 20mm, Dx= 400,000 V/m, 2kV AC P-P at 6kV DC*

There is similarity in the behaviour of the microbubbles observed in this work in comparison with other electrohydrodynamic procedures such as electrohydrodynamic forming. Doshi and Reneker (Doshi and Reneker, 1993) observed in their work on electrospinning, that the jet diameter decreased with increasing nozzle-to-collector distance displaying and inversely proportional relationship. Hekmati et al. (Hekmati et al., 2013) recorded that reducing the nozzle-to-collector distance also contributed to jet instability and an increase in the polydispersity of the fibres produced,

which could be due to incomplete solvent evaporation and also the increase in the field strength when the applied electric field is constrained to a smaller gap, where the latter contributed to the formation of smaller bubbles in the research entailed in this thesis.

Henriques et al. (Henriques et al., 2009) suggested that apart from incomplete solvent evaporation, larger nozzle-to-collector distances sustain weaker electric field strength. Ghelich et al. (Ghelich et al., 2013) recorded a similar occurrence of incomplete solvent evaporation as the aforementioned authors. At a distance of $80\ mm$, fibres formed were not fine and residual fluid was present at the collector indicating incomplete solvent evaporation; increasing the distance to $100\ mm$ generated fine fibres without any influence on the fibre diameter from the sample collected at $80\ mm$. However, further increasing the distance between the nozzle and collector to $150\ mm$ had a pronounced effect on fibre diameter increase owing to the reduction of electrostatic field strength hindering the stretching of the fibres.

In this work, it is to be noted that there was no specific attempt to study bubble stability as only a simple BSA-water model system was used, however the monodisperse microbubbles prepared were stable (I.e. no diameter range) for at least 60-90 minutes.

### 5.2.5 Summary

Two major lines of investigation were conducted in this work in order to understand additional factors that enable further control over microbubble size. Firstly, varying the $M_x$ between the coaxially aligned channels had a pronounced effect in bubble size reduction, especially at $M_x = 100$ . A decrease in bubble diameter from $128 \pm 3.05\ \mu m$ to $71 \pm 4.04\ \mu m$ was observed when $15\%\ BSA$ was used as the continuous fluid medium. Bubble break up occurs when viscous shear overcomes the surface tension, as the $M_x$ is reduced, the surface area of the junction region also reduces thus elevating the shear forces experienced at the junction, hence facilitating the

break-up of bubbles into smaller bubbles. Finally, it was observed that constraining the electric field to a smaller area by decreasing $D_x$ resulted in a reduction in microbubble diameter from $111.33 \pm 1.53\mu m - 97.33 \pm 2.08\mu m$ . This is due to an increase in electric field strength suggesting that very high voltages need not be utilised to facilitate bubble break-up, but constraining the electric field to a smaller region, can potentially promote bubble break up as the effect of the electric field on the fluid stream is intensified. An optimised set-up employing the parameters from the previously discussed investigations enabled formation of microbubbles with diameters of $18.00 \pm 2.08\mu m$.

# Chapter 6

## Numerical results and discussion

### 6.1 Overview

Computational fluid dynamics (CFD) simulations are widely deployed to supplement experimental studies (Patrachari et al., 2012), offering a great degree of control over the systems being tested. They allow for the characterisation of fluid flows and for analysis of the effect of various fluid dynamics parameters such as velocity, shear stress, strain, pressure etc. have. Over the last few years, numerical investigations of T-junctions to model various aspects contributing to droplet formation have gained substantial interest. Adeosun et al.(Adeosun and Lawal, 2009) employed ANSYS FLUENT, a pressure correction, finite volume solver as well, to study the mixing characteristics in a T-junction. For a similar study, Gobby et al.(Gobby et al., 2001) utilised the same class of methodologies, as implemented in CFD-ACE+.

### 6.2 Numerical simulation of microbubble formation with and without the superimposed electric field

#### 6.2.1 Introduction

CFD offers the great advantage of a fully controlled environment, which is a challenge when it comes to practical experiments. For example, it is significantly more difficult to prepare a solution of a particular capillary

number in the laboratory, whereas CFD permits the user to set specific variables including wetting angles of material surfaces and external conditions such as temperature and humidity do not influence the bubble formation. On the same note, in experimental studies, the presence of impurities in the solution or debris in the capillaries can cause inconsistencies in the acquired results, which is not an issue in computational modelling (unless explicitly introduced). The benefit of running multiple test cases simultaneously (subject to processing power) have been a further attractive feature of CFD packages, which economises on time and allows the user to obtain parametrised data about different quantities with ease.

Santos et al.(Santos and Kawaji, 2010) modelled the influence of flow rates on various parameters; these authors elucidated that the pressure drop in micro channels is a common difficulty encountered in microfluidic systems. Their simulations provided them with exact values for the static pressure along the microchannels; the data collected not only provides a better understanding of the pressure distribution along the capillary channel but may also offers ideas on how to optimise the T-Junction geometry such that the pressure drop along channels can be minimised.

Brown et al. (Brown et al., 2012) implemented the CFD-ACE+ Mutliphsyics suite to study the dynamics of fluid ejection during the Blister-Actuated laser-Induced Forward Transfer (BA-LIFT) printing technique. Similar pinch-off occurs when a droplet of ink is ejected from the swelling blister as in the 'squeezing' regime, which was justified as due to the development of a Rayleigh-Plateau instability.

In this work, we present numerical simulations of the microbubble formation without an electric field and under the influence of a superimposed AC on DC electric field, followed by an investigation on the detachment of the bubbles in the mixing region. Results of a grid independence study are presented, followed by a comparison of the simulation results obtained with experimental results.

### 6.2.2 Numerical model

A numerical model to study the hydrodynamic and electrohydrodynamic interactions is created, based on a structured two-block 2D grid consisting of the two inlet channels that pump the liquid and gas into the junction and a stainless steel outlet capillary where the formed bubbles traverse. The fluids in both phases are assumed Newtonian and incompressible. The outlet capillary is polarised with a specific electric field. The geometrical configurations of the T-junction conform to the inner channel diameters of the coaxially aligned capillaries.

The walls were set to a no-slip , no-flux boundary condition (velocity at the walls is zero), the electric field is applied along the walls of the outlet capillary and the gas and liquid flow rates were set to the values used in the experiments. The mass, momentum and electric field equations are discretised and applied on a structured mesh using the finite volume method (FVM). The gas/liquid interface is resolved using the Volume of Fluid (VOF) method. The conservation equations are solved in a fully implicit manner by means of the Crank-Nicholson time-marching method (i.e. second order in time). To ensure second order accuracy in space and to acquire properly resolved results, the central differencing scheme was employed for all spatial derivatives and interpolations. An auto-time step is selected with a fixed yet conservative Courant-Fredrichs-Lewy (CFL) (Courant et al., 1967, Hawker and Ventikos, 2012) number of 0.5 which regulates the maximum advancement of the fraction of the cell occupied by the fluid within one time-step and ensures that results display minimal dependence on the temporal resolution. The AMG solver was preferred over the CGS to iteratively resolve the series of algebraic equations due to its accuracy and extensive usage in the literature (Kickinger, 1998, Yang, 2006, Cleary et al., 1998). The solution used for the liquid and gas phase are BSA and nitrogen respectively, with corresponding physical and electrical properties. Details regarding the solution properties can be found in chapter 4.

### 6.2.3 Formation of microbubbles

Three main tests were conducted in this section: (i) to simulate the T-junction without the application of an electric field, followed by (ii) application of a DC field along the capillary outlet walls, and (iii) superimposing an AC on a DC electric field. The formation of microbubbles under these conditions is shown in figure 42, using the VOF method, whereby in this case, f=1 represents a cell occupied by gas and f=0 represents a cell occupied by liquid. From figure 42a, it can be observed that as the gas enters the main fluid channel, its volume begins to grow until it breaks off forming a uniform bubble. Applying a DC field of 6kV along the walls of the outlet capillary results in smaller bubbles, however also in an increase in their polydispersity, as shown in figure 42b. The gas stream is observed to traverse further into the outlet channel before retracting back towards the junction. Introducing an oscillating field results in a steady stream of smaller bubbles which are more homogenous in size (figure 42c).

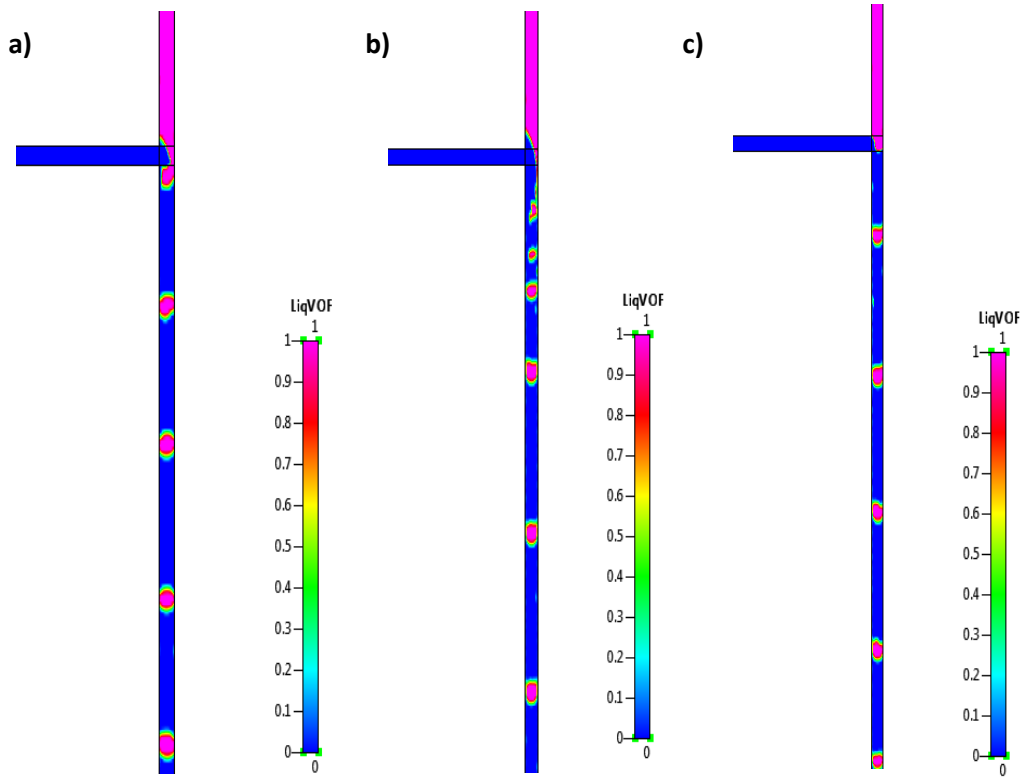


*Figure 42: Microbubble formation in the T-Junction a) Without an electric field b) DC electric field of 6kV DC and c) AC on DC of 6kV, 2kHz*

This steady formation can be attributed to the fact that the application of a frequency generates a regular disturbance at the liquid interface (Balachandran et al., 1992). Figure 43 displays the velocity vectors around the bubble without an application of an electric field and under the influence of electrical stresses. In the absence of an electric field, the velocity vector distributions display slight perturbations as the bubble traverses along the outlet channel, and forming microbubbles of $115\ \mu m$. Similar results were observed in figure 43b) upon application of a DC electric field, where the bubble diameter was recorded to be $108\ \mu m$ .

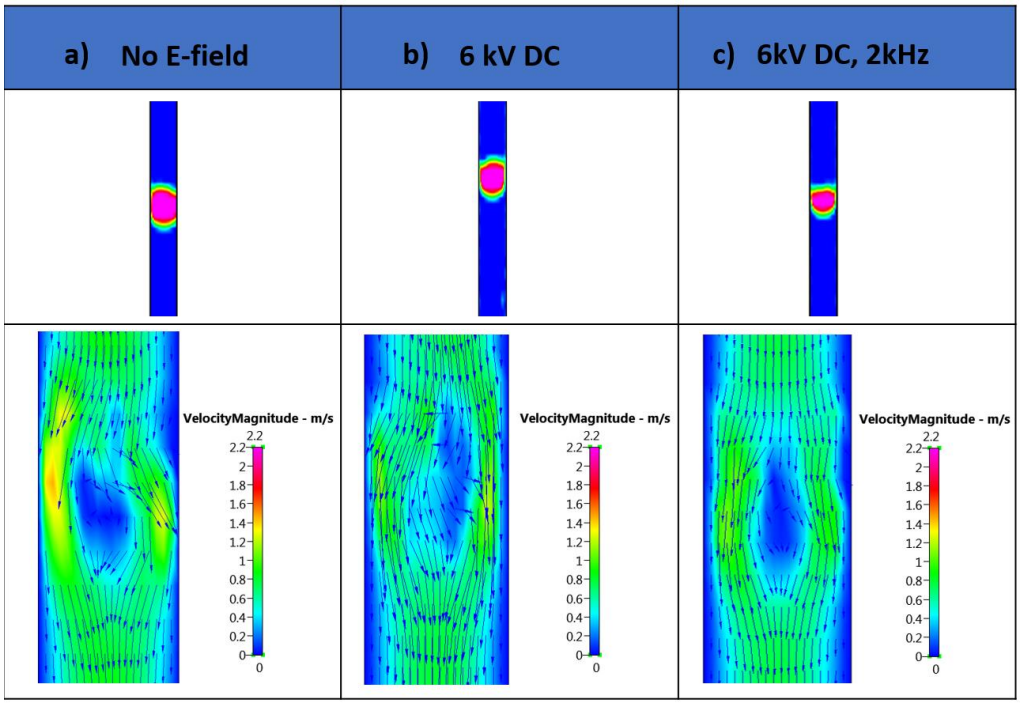


*Figure 43: Velocity magnitude vector plots of the microbubble with a) No electric field b) 6kV DC c) 6kV DC, 2kHz*

On the other hand, in the presence of a superimposed field, there is a uniform velocity field distribution along the bubble (figure 43c) which contributes to the controlled detachment of the emerging microbubble. Increasing the frequency from $0 - 5kHz$ results in the decrease in microbubble diameter from $115\ \mu m$ to $60\ \mu m$. Utilising the same parameters, the experimental results resulted in a decrease in microbubble diameter from $111 \pm 5.26\ \mu m$ to $31 \pm 2.08\ \mu m$. This is summarised in figure 44.

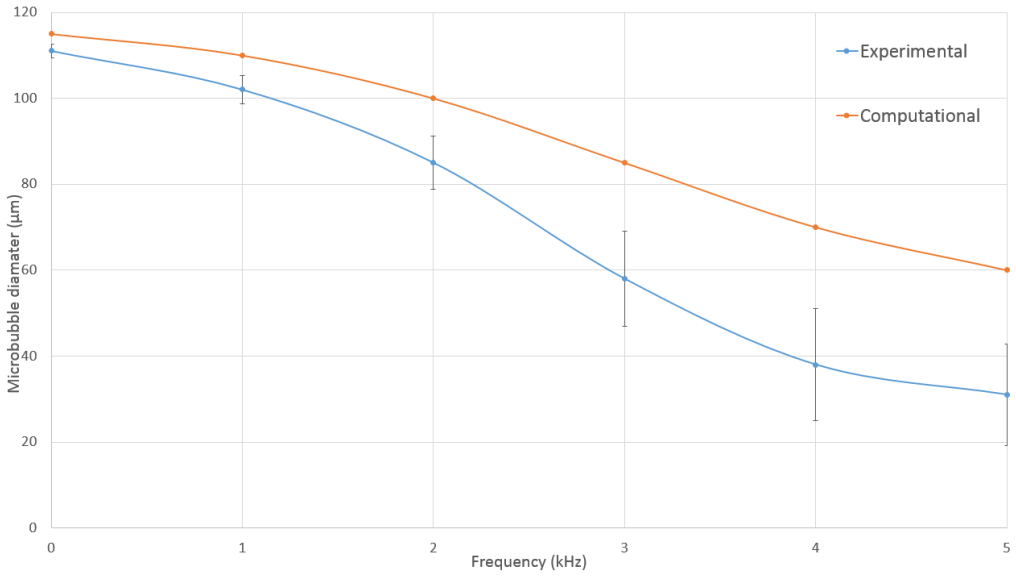


*Figure 44: Comparison of microbubble diameter at frequencies 0-5 kHz obtained experimentally and computationally*

### 6.2.4 Numerical Investigation of microbubble detachment

As described in detail chapter 2, flow in the microchannels is represented by low Reynolds numbers, as the flow is dominated by viscous stresses and surface tension forces. Figure 45 presents images of the gas column approaching the mixing region and the corresponding velocity magnitude vector fields observed at the mixing zone.

Just before gas column enters the mixing region, recirculation is observed possibly due to the disturbance in the laminar flow caused by the two fluid media coming in contact (figure 45iii). As the gas column enters the mixing region the vortex cuts through the gas stream and pushes the gas-liquid interface towards the edge of the junction until the neck breaks and forms a bubble. This phenomenon is shown in figures 46i-46iii .

Similar flow dynamics was observed by Guo et al. (Guo and Chen, 2009) in their numerical investigations on Taylor bubble formation in a microchannel using the VOF method. These authors attributed this circulation as a feature of the 'squeezing regime', which has been reported in great detail by Garstecki et al.(De Menech et al., 2008).

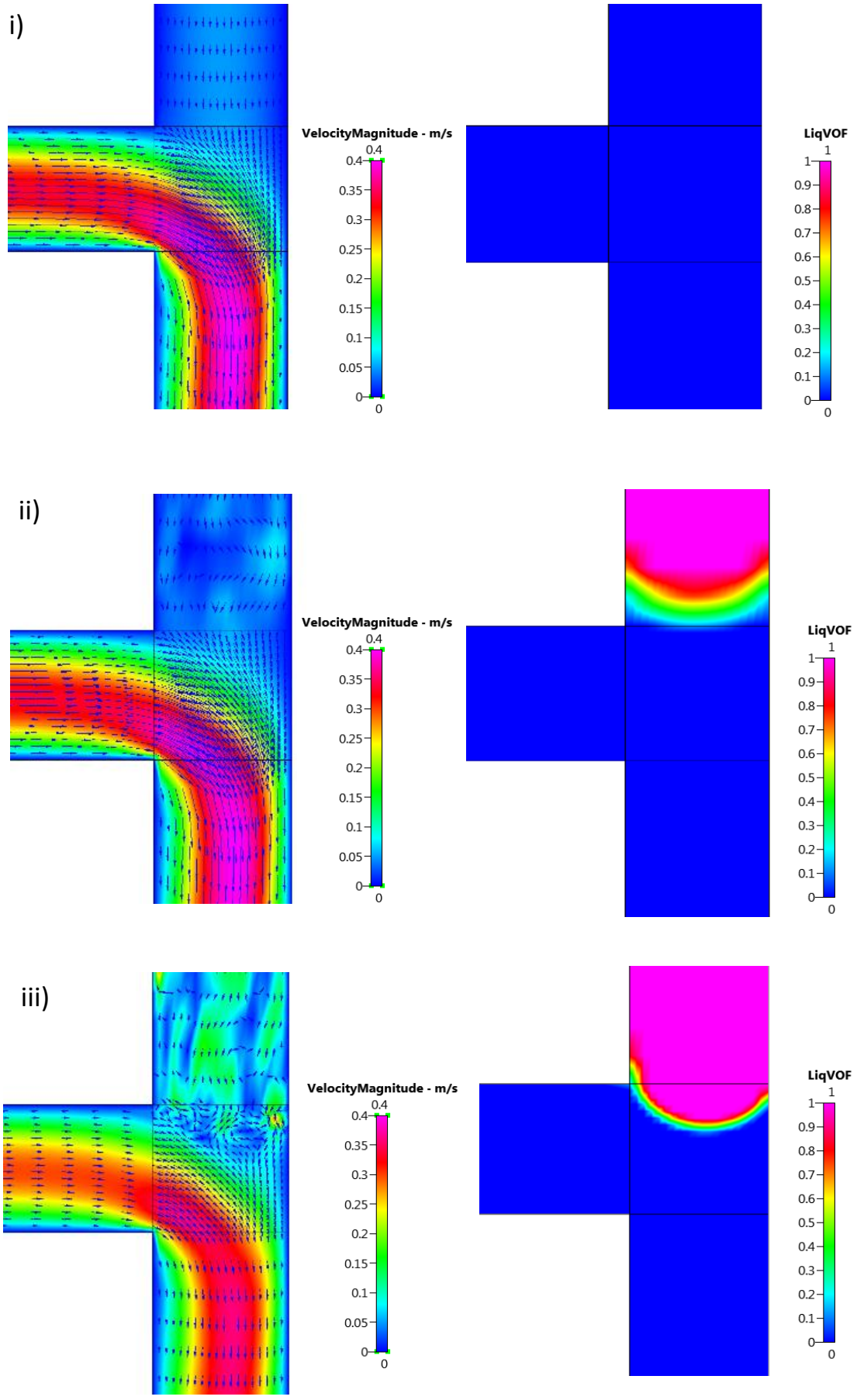


*Figure 45: Velocity magnitude plots corresponding to VOF simulations at various stages of the gas column approaching the mixing region without application of the electric field.*

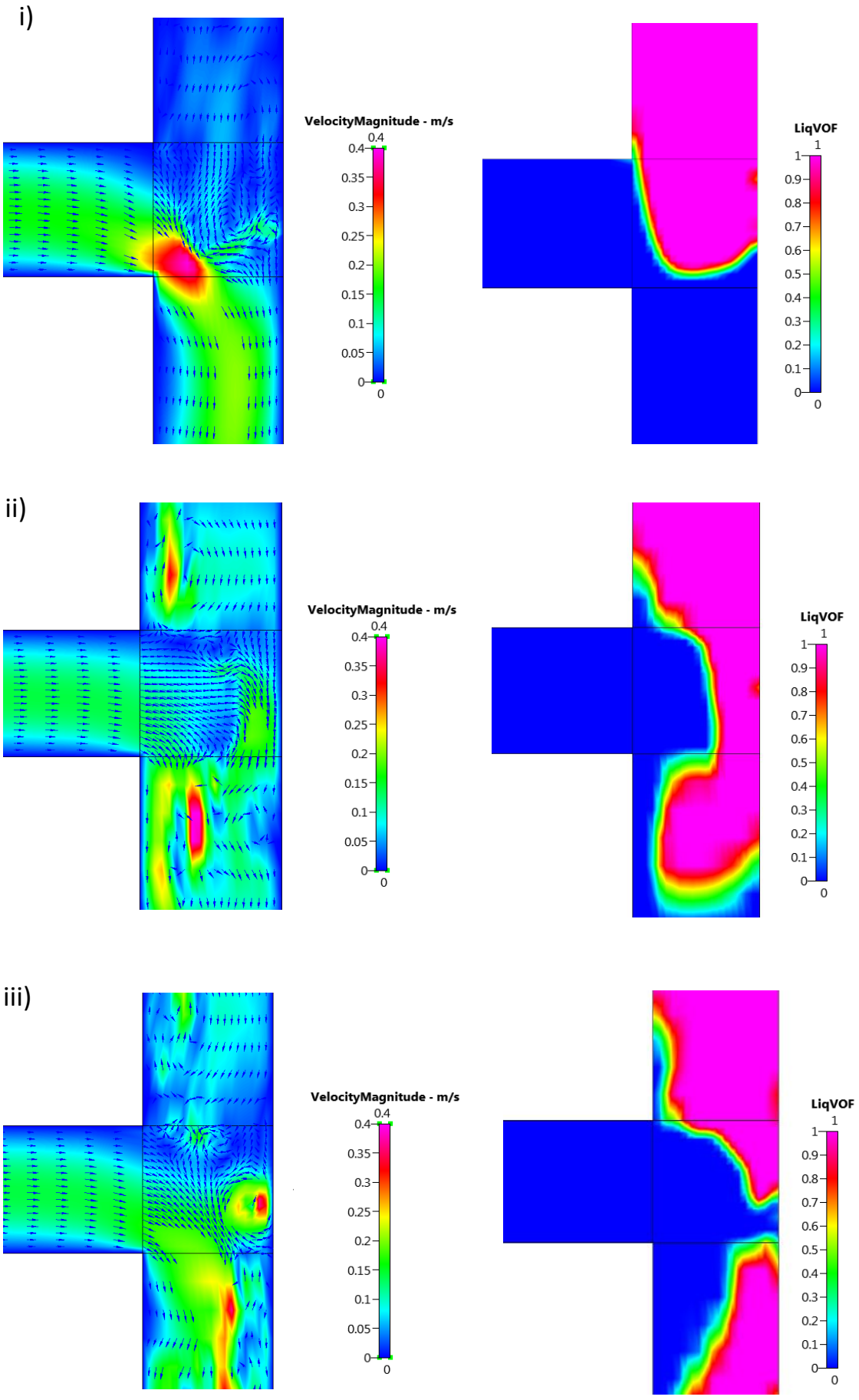


*Figure 46: Velocity magnitude contours corresponding to the VOF simulation results displaying the bubble detachment and gas column retracting back into the inlet.*

Beyond the squeezing stage, the diameter decreases rapidly and the liquid rushes to fill the volume of around the neck as shown by the velocity vectors in figure 46ii. This result shows good agreement with the research conducted by van Steijn et al. (van Steijn et al., 2007). From the velocity plots it can be seen that as the gas column occupies the junction, there is a distinctive drop in velocity upstream, suggesting a build-up of pressure which facilitates narrowing of the neck.

The recirculation observed after the stream breaks up is due to the recoiling of the gas column and the surface tension pulling the tail of droplet to form the equilibrium shape (Sivasamy et al., 2011, Soh et al., 2016). It can be elucidated that the vortex observed in the simulation results contribute to the bubble detachment process.

### 6.2.5 Comparison of simulation results with optical micrographs

Microbubbles formed in the simulations and micrographs were scaled and measured using ImageJ and compared with the optical micrographs obtained in the experiments. Smaller bubbles have higher internal pressure and release gas to dissolve under pressure into the surrounding under-saturated solution, whereas larger bubbles grow by taking up gas from a supersaturated solution. The underlying reason behind this phenomenon is that smaller microbubbles shrink as a result of their high Laplace pressure, and thus create areas of supersaturation in the local environment. This causes larger bubbles to grow via a process called Ostwald Ripening (Talu et al., 2006). Elevated levels of pressure were recorded in the smaller microbubbles generated using a superimposed AC on DC electric field, as opposed to the larger microbubbles produced in the absence of any electric fields. It should be noted that the Ostwald Ripening process is not modelled in our simulations.

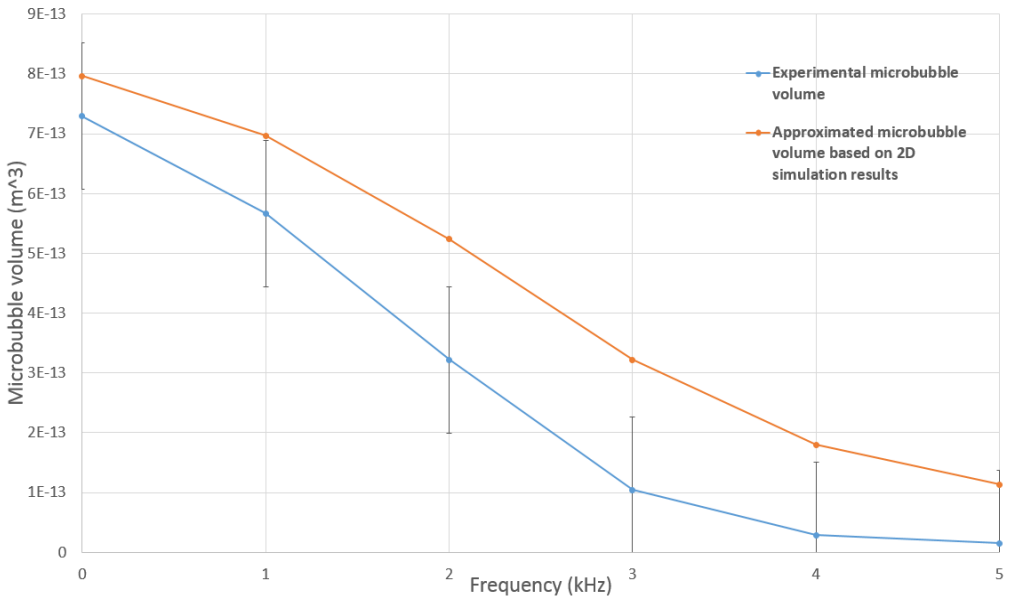


*Figure 47: Comparison of calculated microbubble volume from experiments and approximated microbubble volume based on the 2D simulation results at 6kV DC, 2kV P-P between 1-5 kHz.*

Figure 47 presents a graph of the volume of the microbubbles obtained via the experiments against the approximated volume from the 2D simulation results. A good trend between the results can be seen, the discrepancy between the two curves attributes from the uncertainty in the VOF boundary condition, as only 2D simulations were computed as part of this thesis. This also suggests the need for a finer grid in order to resolve the boundaries more accurately, which will be conducted as part of the further work.

### 6.2.6 Grid independence study

In order further improve the 2D model developed, a grid independence was conducted in order to attain the most accurate grid for future work. Three different grids were generated using CFD-GEOM (ESI Group, Paris) and simulations were conducted without the application of an electric field to examine the level grid independence of the study. The bubbles produced under the same conditions were measured and plotted as a function of the

number of elements in the respective mesh (figure 48). We can define an acceptable tolerance for the grid independence study as a 1% variation in the solution as the residual approaches 0. Although it is clear that full grid independence has not been achieved, we can see that the difference between the second and third finer mesh is significantly smaller than the difference between the first and the second mesh, therefore a trend towards convergence is confirmed.

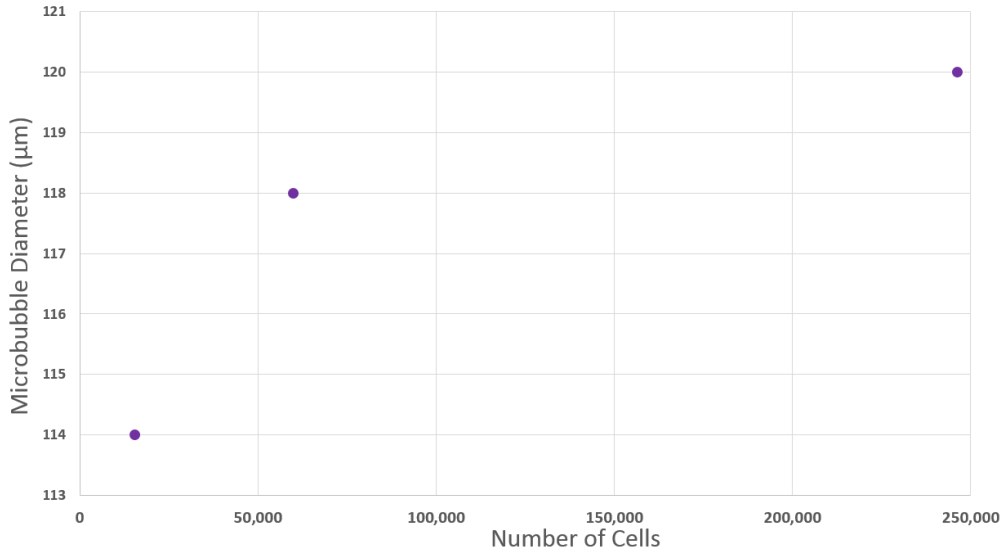


*Figure 48: Grid independence study of the 2D T-Junction*

### 6.2.7 Summary

A 2D CFD model was developed to simulate the T-Junction under the influence of various electric fields. Numerical simulations of the microbubble formation and detachment were presented with and without an electric field. Disturbances in the flow field were observed in the microbubbles formed, in the absence of an electric field. On the other hand, we recorded a more stable flow field along the bubble interface when a superimposed field was applied, combined with the formation of smaller microbubbles.

The flow analysis of the microbubbles emerging from the junction is presented and compared with the literature. Recirculation is recorded just before the gas column enters the mixing region. This is possibly due to the

disruption in the laminar flow caused by the two fluid media coming in contact at the junction. As the gas column enters the mixing region the liquid stream cuts through the vortex and pushes the gas-liquid interface towards the edge of the junction until the neck breaks and forms a bubble via the 'squeezing regime'.

The vortex behaviour recorded in the simulation results contribute to the bubble detachment process. The microbubbles generated in the simulations were compared with the optical micrographs attained in the experiments and the pressure along the cross section of the bubble was plotted. A grid independence study was conducted, showing a converging trend for the meshes tested.

# Chapter 7

## Conclusions and future work

## 7.1 Conclusions

The main contribution of the research described in this thesis is the development of a novel experimental apparatus combining two widely established techniques to prepare microbubbles – microfluidics and electrohydrodynamics. An AC electric field was superimposed on a DC electric field and applied to the nozzle of a T-Junction microfluidic device as a viable technique for preparing microbubbles with specific size distributions. This study aimed to investigate the effect of the frequency, AC magnitude, mixing region geometry and the tip-to-collector distance on the formation of microbubbles in order to provide the user with further control over the size and homogeneity of the bubbles and tailor them to suit specific applications.

This objective was fulfilled via two main investigations; firstly, the influence of the AC magnitude and frequency were tested. It was observed that these two parameters had a notable effect on the monodispersity of the microbubbles. . Secondly, the effect of the mixing region was altered in order to understand its effect on the microbubble size, followed by investigating the effect of the electric field strength by varying the tip-to-collector distance.

A computational model was developed observe the hydrodynamic and electrohydrodynamic interactions occurring within the T-Junction device.. The CFD-ACE+ Multiphysics suite was used to construct a 2D model of the T-

junction utilised in this work. The main simulations that were conducted involved bubble formation under the three main conditions – (i) without an electric field, (ii) with a DC field only and, (iii) a superimposed AC on DC electric field. This was followed by an analysis of the bubbles formed under each of the aforementioned stress fields and investigating the dynamics behind the detachment of the newly formed bubble. Finally, a comparison between the experimental and numerical results is presented. The main conclusions drawn from this work are expanded further in the sections below.

### 7.1.1 Novel experimental set up to prepare monodisperse microbubbles using superimposed AC-DC electric fields.

An AC superimposed on a DC electric field was applied to the nozzle of a capillary embedded T-Junction device. In order to achieve this, a waveform generator was utilised to drive the inputs of a high voltage amplifier, which outputs an amplified voltage at the load. The applied DC can be varied by adjusting the offset on the waveform generator. The high voltage output was connected to the T-Junction outlet to deliver the superimposed voltage. This novel apparatus successfully generates monodisperse and stable microbubbles.

Two main experiments were carried out in order to investigate the effect of the applied AC voltage magnitude and frequency at various applied DC voltages. The solutions used comprised of glycerol and distilled water which acted like a model system.

Firstly, the effect of the superimposed AC was carried out at $2\ kV_{P-P}$, $3\ kV_{P-P}$ and $4\ kV_{P-P}$. $3\ kV_{P-P}$ and $4\ kV_{P-P}$ resulted in the formation of larger bubbles possibly due to prolonged exposure to high voltage AC fields. The bubbles tend to expand due to electrohydrodynamic convection across the surface leading to bubble growth.

Increasing the frequency resulted in the formation of smaller bubbles. A distinctive drop in bubble diameter of $138 \pm 0.58\ \mu m - 99 \pm 1.53\ \mu m$ was observed between $600 - 900\ Hz$. These results are indicative of a complex system which is subjected to various parameters that are non-linear in nature. The sudden drop in bubble diameter observed in figure 4B between 600-900Hz can be possibly attributed to the resonance of the bubble of that diameter as a result of the applied frequency.

The results acquired suggest that the bubble diameter is strongly influenced by the frequency of the AC electric field and that there is potential to achieve bubbles of smaller sizes at higher frequencies.

### 7.1.2 Effect of electric field strength and mixing region geometry coupled with AC-DC electric fields

Two major lines of research were undertaken in this study in order to understand the additional factors that can provide the user further control over the process and the microbubble size. An amplifier capable of delivering higher frequencies was integrated into the apparatus to replace the previously utilised amplifier.

Firstly, the distance between the coaxially aligned channels, $M_x$, was varied for two different solution concentrations of BSA. An $M_x$ value of $100\ \mu m$ reduced the microbubble diameter from $128 \pm 3.05\ \mu m$ to $88 \pm 5.65 \mu m$ with $10\%$ BSA. Similarly, a reduction of $128 \pm 3.05\ \mu m$ to to $71 \pm 4.04\ \mu m$ was recorded when a 15% BSA solution was used. Reducing $M_x$, causes a consequent reduction in surface area at the junction where both fluid phases meet, therefore elevating the shear stresses that are experienced at the junction. This, in turns facilitates the formation of smaller bubbles which occurs when the shear stresses overcome the surface tension forces.

The effect of varying the tip-to-collector distance $D_x$ was also presented. Decreasing the distance between the tip and collector increases the electric

field strength, such that the electric forces are confined to a smaller area thus have a greater effect on the bubble break up. The two different DC voltages used were $6\ kV$ and $8\ kV\ DC$ which produced ideal results in the previous investigation along with a frequency of $2200\ Hz$ which facilitated the rapid disintegration in the previous study. Significant reduction in microbubble diameter was observed at $6\ kV\ DC$ , where decreasing $D_x$ from $100\ mm$ to $20\ mm$ results in the average microbubble diameter reducing from $111 \pm 1.53\mu m$ to $86.33 \pm 1.53\mu m$ suggesting that very high voltages need not be used to achieve smaller microbubbles.

Finally, an optimised experimental set up was configured employing the following ideal parameters based on all the experimental studies presented in this work: electrical parameters of $6\ kV\ DC$, $2\ kV_{P-P}$; BSA 10% wt. concentration, $M_x$ of $100\ \mu m$ and $D_x$ of $400{,}000\ V/m$. Using these parameters, the effect of the frequency was reported. $6\ kV\ DC$ generated a bubble size reduction from $111 \pm 1.53\mu m$ to$18 \pm 2.08\mu m$)

The results achieved in this study suggest that a unique combination of parameters can be employed to achieve particular bubble sizes to suit various applications. This novel apparatus presents a viable and innovative methodology to prepare monodisperse microbubbles with precision and provides the user with control over the bubble diameter and over process.

### 7.1.3 Numerical simulation of microbubble formation with and without the superimposed electric field

A 2D CFD model was executed to simulate the T-Junction under the influence of various electric fields.

Numerical simulations of the microbubble formation and detachment were presented in the absence of an electric field, a DC electric field and a superimposed electric field.

Applying a DC voltage of $6\ kV$ along the walls of the outlet capillary resulted in smaller bubbles with an increase in their polydispersity. The gas stream

traverses further into the outlet channel before retracting back towards the junction.

An oscillating field results in a steady stream of smaller bubbles which are homogenous in nature. This steady formation can be attributed to regular axisymmetric disturbance an oscillating field generates at the interface.

Analysis of the flow fields were presented in the absence of an electric field, the velocity vector distributions display slight perturbations as the bubble traverses along the outlet channel. A uniform velocity field distribution along the bubble was recorded with a superimposed electric field contributing to the controlled detachment of the emerging microbubble. Increasing the frequency from $0 - 5kHz$ results in the decrease in microbubble diameter from $115\ \mu m$ to $60\ \mu m$. Utilising the same parameters, the experimental results resulted in a decrease in microbubble diameter from $111 \pm 5.26\ \mu m$ to $31 \pm 2.08\ \mu m$.

### 7.1.4 Numerical investigation of microbubble detachment

The bubble detachment process was investigated, and the flow fields were analysed. Recirculation is present prior to the gas column entering the junction, possibly due to the disturbance in the laminar flow caused by the two fluid media coming in contact. As the gas column occupies the junction, a distinctive drop in velocity is observed upstream. This suggests an increase in pressure, which facilitates narrowing of the neck which eventually leads to the detachment of the microbubble. The vortex cuts through the gas stream and pushes the gas-liquid interface towards the edge of the junction until the neck breaks and forms a bubble. The recirculation present in the simulations occurs during the widely reported 'squeezing regime'(Garstecki et al., 2006).

### 7.1.5 Comparison of simulation results with optical micrographs

The outer diameter of the microbubbles generated in the simulations were measured using the ImageJ software (ImageJ 1.46r, National Institute of Health, Maryland, USA). and were compared with the optical micrographs attained in the experiments. . – The experiments and the simulations displayed a good trend. The slight variation between the two curves can be attributed a to the uncertainty in the VOF boundary condition as the calculations were based on a 2D grid. This can be alleviated in the further work by generating a fine grid such that the boundaries are captured more clearly.

A novel experimental set up that successfully combined microfluidics and superimposed AC on DC fields was presented. The experimental study generated highly monodisperse microbubbles in a single step, with a high level of control over their size with the new parameters such as frequency and applied AC that are introduced using the robust apparatus which benefits from low power requirements of 1.2W. The optimised set up described paves way to construct a portable machine based on the concepts detailed in this thesis, where the user has the controlled ability to tailor the microbubble diameter to suit specific applications.

## 7.2 Future work

Microbubbles should possess the following features: high stability and uniform size. The technique chosen for their preparation should be able to generate these features in an economical and scalable way. T-junction microfluidic processing techniques are a versatile tool for the generation of uniform bubbles for a plethora of applications. As it was shown in this thesis, the microfluidic technique can be improved by introducing an oscillating

electric field to provide further control over their size and the overall process. The results acquired have established a framework for further research which are recommended below:

1) The dimensions of the capillaries utilised in this study were fixed at $100\ \mu m$, nevertheless microbubbles prepared using this apparatus were smaller than the channel dimensions. Bubbles of smaller diameters can be obtained by employing capillaries of internal diameters of <100µm which can be investigated in conjunction with the apparatus described in this work.

2) Since higher frequencies displayed favourable results in terms of size reduction, it would be beneficial to explore the effect of frequencies beyond $10\ kHz$ by replacing the existing amplifier with equipment that has higher frequency capabilities to potentially reduce the microbubble diameter further. In order to target biomedical applications such as ultrasound contrast agents, the acceptable size range is approximately 2-10µm, without compromising the production rate or stability of the microbubbles.

3) The work described in this thesis only utilised the sinusoidal waveform. Further experiments can be conducted by varying the type of waveform applied at the nozzle (sawtooth, square, pulse), in order to determine whether the choice of waveform has an impact on the microbubble formation process.

4) The biomedical applications of microbubbles also require them to be highly stable and a standard deviation in microbubble diameter of less than $5\ \mu m$. In order to meet such requirements, bubbles coated with a shell of polymer or lipid are emerging as medium for drug delivery and ultrasound imaging, where the stability is much higher than uncoated microbubbles. If a

polymeric solution or a solution containing lipid can be added with a material to boost the viscosity, such that the desired small bubble size combined with a high stability profile can be manufactured.

5) The experiments can be repeated for solutions with different electrical conductivities. This can be tested by adding Sodium Chloride to the BSA solution such that the influence of the voltage supply on the microbubble increases.

6) Additional grid dependence tests must be conducted to refine the mesh in order to identify the ideal number of elements required to obtain an accurate grid using the least amount of computational resources.

7) The T-junction employed in this work consists of circular channels. Varying the mixing region geometry affects the size of the microbubbles produced. Further to this, the geometric effects of a square mixing chamber on the microbubble diameter can also be investigated.

8) Further to identifying the ideal grid, a 3D geometry of the T-Junction should be constructed to provide a complete representation of the T-junction.

9) Further CFD simulations can be conducted to vary the electric field strength and observe the behaviour of the flow fields as the intensity of the electric field is increased. The effect on reducing the mixing region geometry can be simulated in order to develop a quantities analysis of the shear stresses experienced at the junction due to a reduction in surface area of this region.

## 7.3 Commercial viability

The apparatus presented in this thesis is a robust way to generate microbubbles efficiently, in a relatively easy manner for industries such as food engineering, waste water treatment and as biosensors. Further investigation detailed in the section above will enable

Being able to parallelise the apparatus described in this work makes it favourable for the food industry where very small bubbles are not required. This methodology presents an economical way to generate novel structures with a great degree of control over size and the processing parameters. Taste and oral sensory perception plays an important role in the palatability of food being a potential industry which would benefit from the apparatus presented in this work.

Large quantities of microbubbles of $< 150\ \mu m$ are desired in waste water treatment processes such as ozonation and flotation (Jabesa and Ghosh, 2016, Wen et al., 2011) due to their high surface area to volume ratio which is essential to separate particulates from potable water. The apparatus presented in this work can be parallelised in order to generate a large quantity of bubbles this application necessitates.

Biosensors are used in food safety measurements to detect bacteria such as Escherichia Coli (E-Coli) due to their high level of sensitivity and accurate detection of harmful pathogens(Ten et al., 2017). Fine bubbles provide a large surface throughput to bacteria, ranging from $35 - 250\ \mu m$ (Mann and Krull, 2004, Mahalingam et al., 2015). Very small bubbles tend to burst more rapidly, therefore a balance in size and stability is of paramount importance. The apparatus presented in this thesis generates bubbles that are homogenous in nature which can be beneficial in the aforementioned application.

# References


ADEOSUN, J. T. & LAWAL, A. 2009. Numerical and experimental studies of mixing characteristics in a T-junction microchannel using residence-time distribution. *Chemical Engineering Science,* 64**,** 2422-2432.

AFONSO, A. M., PINHO, F. T. & ALVES, M. A. 2012. Electro-osmosis of viscoelastic fluids and prediction of electro-elastic flow instabilities in a cross slot using a finite-volume method. *Journal of Non-Newtonian Fluid Mechanics,* 179**,** 55-68.

AHMAD, B., STRIDE, E. & EDIRISINGHE, M. 2012. Calcium Alginate Foams Prepared by a Microfluidic T-Junction System: Stability and Food Applications. *Food and Bioprocess Technology,* 5**,** 2848-2857.

AHMAD, Z., ZHANG, H. B., FAROOK, U., EDIRISINGHE, M., STRIDE, E. & COLOMBO, P. 2008. Generation of multilayered structures for biomedical applications using a novel tri-needle coaxial device and electrohydrodynamic flow. *Journal of the Royal Society Interface,* 5**,** 1255-1261.

AL-MASHHADANI, M. K. H., WILKINSON, S. J. & ZIMMERMAN, W. B. 2016. Carbon dioxide rich microbubble acceleration of biogas production in anaerobic digestion. *Chemical Engineering Science,* 156**,** 24-35.

ALEXANDER, M. S., PAINE, M. D. & STARK, J. P. W. 2006. Pulsation Modes and the Effect of Applied Voltage on Current and Flow Rate in Nanoelectrospray. *Analytical Chemistry,* 78**,** 2658-2664.

ANDERSON, J. R., CHIU, D. T., WU, H., SCHUELLER, O. & WHITESIDES, G. M. 2000. Fabrication of microfluidic systems in poly (dimethylsiloxane). *Electrophoresis,* 21**,** 27-40.

ANNA, S. L., BONTOUX, N. & STONE, H. A. 2003. Formation of dispersions using “flow focusing” in microchannels. *Applied physics letters,* 82**,** 364-366.

ATIAS, M., WOLFSHTEIN, M. & ISRAELI, M. 1977. Efficiency of Navier-Stokes Solvers. *AIAA Journal,* 15**,** 263-266.

AUTHOR, A. 2008. Flow control in microfluidics: are the workhorse flows adequate? *Lab on a Chip,* 8**,** 383-387.

AVIVI, NITZAN, Y., DROR, R. & GEDANKEN, A. 2003. An Easy Sonochemical Route for the Encapsulation of Tetracycline In Bovine Serum Albumin Microspheres. *Journal of the American Chemical Society,* 125**,** 15712-15713.

BAILEY, R. 2017. Managing false diffusion during second-order upwind simulations of liquid micromixing. *International journal for numerical methods in fluids,* 83**,** 940-959.

BALACHANDRAN, W., MACHOWSKI, W. & AHMAD, C. N. Electrostatic atomisation of conducting liquids using AC superimposed on DC fields. Industry

Applications Society Annual Meeting, 1992., Conference Record of the 1992 IEEE, 4-9 Oct. 1992 1992. 1369-1373 vol.2.

BAROUD, C. N., GALLAIRE, F. & DANGLA, R. 2010. Dynamics of microfluidic droplets. *Lab on a Chip,* 10**,** 2032-2045.

BASHIR, S., REES, J. M. & ZIMMERMAN, W. B. 2014. Investigation of pressure profile evolution during confined microdroplet formation using a two-phase level set method. *International Journal of Multiphase Flow,* 60**,** 40-49.

BAYRAKTAR, T. & PIDUGU, S. B. 2006. Characterization of liquid flows in microfluidic systems. *International Journal of Heat and Mass Transfer,* 49**,** 815-824.

BECKER, H. & LOCASCIO, L. E. 2002. Polymer microfluidic devices. *Talanta,* 56**,** 267-287.

BENEVENTI, D., CARRE, B. & GANDINI, A. 2001. Role of surfactant structure on surface and foaming properties. *Colloids and Surfaces A: Physicochemical and Engineering Aspects,* 189**,** 65-73.

BERNESCHI, S., BALDINI, F., COSCI, A., FARNESI, D., NUNZI CONTI, G., TOMBELLI, S., TRONO, C., PELLI, S. & GIANNETTI, A. 2017. Fluorescence biosensing in selectively photo–activated microbubble resonators. *Sensors and Actuators B: Chemical,* 242**,** 1057-1064.

BHATTACHARYA, S. & HWANG, S.-T. 1997. Concentration polarization, separation factor, and Peclet number in membrane processes. *Journal of Membrane Science,* 132**,** 73-90.

BLANCHARD, D. C. 1975. Bubble Scavenging and the Water-to-Air Transfer of Organic Material in the Sea. *Applied Chemistry at Protein Interfaces.* AMERICAN CHEMICAL SOCIETY.

BONFIELD, W. 2006. Designing porous scaffolds for tissue engineering. *Philosophical Transactions of the Royal Society A: Mathematical, Physical and Engineering Sciences,* 364**,** 227.

BORRA, J. P., EHOUARN, P. & BOULAUD, D. 2004. Electrohydrodynamic atomisation of water stabilised by glow discharge—operating range and droplet properties. *Journal of Aerosol Science,* 35**,** 1313-1332.

BOYER, F. 2011. Analysis of the upwind finite volume method for general initial-and boundary-value transport problems. *IMA Journal of Numerical Analysis,* 32**,** 1404-1439.

BRACKBILL, J. U., KOTHE, D. B. & ZEMACH, C. 1992. A continuum method for modeling surface tension. *Journal of Computational Physics,* 100**,** 335-354.

BRANDT, A. & YAVNEH, I. 1991. Inadequacy of first-order upwind difference schemes for some recirculating flows. *Journal of Computational Physics,* 93**,** 128-143.

BROOKS, A. N. & HUGHES, T. J. R. 1982. Streamline upwind/Petrov-Galerkin formulations for convection dominated flows with particular emphasis on the incompressible Navier-Stokes equations. *Computer Methods in Applied Mechanics and Engineering,* 32**,** 199-259.

BROWN, M. S., BRASZ, C. F., VENTIKOS, Y. & ARNOLD, C. B. 2012. Impulsively actuated jets from thin liquid films for high-resolution printing applications. *Journal of Fluid Mechanics,* 709**,** 341-370.

CAMPBELL, G. M. & MOUGEOT, E. 1999. Creation and characterisation of aerated food products. *Trends in Food Science & Technology,* 10**,** 283-296.

CARETTO, L. S., GOSMAN, A. D., PATANKAR, S. V. & SPALDING, D. B. 1973. Two calculation procedures for steady, three-dimensional flows with recirculation. *In:* CABANNES, H. & TEMAM, R. (eds.) *Proceedings of the Third International Conference on Numerical Methods in Fluid Mechanics: Vol. II Problems of Fluid Mechanics.* Berlin, Heidelberg: Springer Berlin Heidelberg.

CARROLL, G. T., DEVEREUX, P. D., KU, D. N., MCGLOUGHLIN, T. M. & WALSH, M. T. 2010. Experimental validation of convection-diffusion discretisation scheme employed for computational modelling of biological mass transport. *BioMedical Engineering OnLine,* 9**,** 34-34.

CASKEY, C. F. 2017. Ultrasound Molecular Imaging and Drug Delivery. *Molecular Imaging and Biology,* 19**,** 336-340.

CASTRO-HERNANDEZ, E., VAN HOEVE, W., LOHSE, D. & GORDILLO, J. M. 2011. Microbubble generation in a co-flow device operated in a new regime. *Lab on a Chip,* 11**,** 2023-2029.

CAVALIERI, F., MICHELI, L., KALIAPPAN, S., TEO, B. M., ZHOU, M., PALLESCHI, G. & ASHOKKUMAR, M. 2013. Antimicrobial and Biosensing Ultrasound-Responsive Lysozyme-Shelled Microbubbles. *ACS Applied Materials & Interfaces,* 5**,** 464-471.

CHAKRABORTY, J., RAY, S. & CHAKRABORTY, S. 2012. Role of streaming potential on pulsating mass flow rate control in combined electroosmotic and pressure-driven microfluidic devices. *ELECTROPHORESIS,* 33**,** 419-425.

CHAN, B. P. & LEONG, K. W. 2008. Scaffolding in tissue engineering: general approaches and tissue-specific considerations. *European Spine Journal,* 17**,** 467-479.

CHE, S., GARCIA-BENNETT, A. E., YOKOI, T., SAKAMOTO, K., KUNIEDA, H., TERASAKI, O. & TATSUMI, T. 2003. A novel anionic surfactant templating route for synthesizing mesoporous silica with unique structure. *Nat Mater,* 2**,** 801-805.

CHEN, B., LI, G., WANG, W. & WANG, P. 3D numerical simulation of droplet passive breakup in a micro-channel T-junction using the Volume-Of-Fluid method. *Applied Thermal Engineering*.

CHEN, Z.-Y., LIN, Y., YANG, F., JIANG, L. & GE, S. P. 2013. Gene therapy for cardiovascular disease mediated by ultrasound and microbubbles. *Cardiovascular Ultrasound,* 11**,** 11.

CHENG, K. J. & CHADDOCK, J. B. 1985. Effect of an electric field on bubble growth rate. *International Communications in Heat and Mass Transfer,* 12**,** 259-268.

CHENG, N.-S. 2008. Formula for the Viscosity of a Glycerol−Water Mixture. *Industrial & Engineering Chemistry Research,* 47**,** 3285-3288.

CHO, S. K., FAN, S.-K., MOON, H. & KIM, C.-J. Towards digital microfluidic circuits: creating, transporting, cutting and merging liquid droplets by electrowetting-based actuation. Micro Electro Mechanical Systems, 2002. The Fifteenth IEEE International Conference on, 2002. IEEE, 32-35.

CHOI, Y., KIM, S., KIM, H., KIM, Y. & CHUNG, T. 2009. Effects of current density and electrode material on the dewaterability of the thickened activated sludge by electro-flotation. *Journal of chemical technology and biotechnology,* 84**,** 1493-1498.

CHRISTOPHER, G. F. & ANNA, S. L. 2007. Microfluidic methods for generating continuous droplet streams. *Journal of Physics D: Applied Physics,* 40**,** R319.

CHRISTOPHER, G. F., BERGSTEIN, J., END, N. B., POON, M., NGUYEN, C. & ANNA, S. L. 2009. Coalescence and splitting of confined droplets at microfluidic junctions. *Lab on a chip,* 9**,** 1102-1109.

CLEARY, A. J., FALGOUT, R. D. & JONES, J. E. 1998. Coarse-grid selection for parallel algebraic multigrid. *Solving Irregularly Structured Problems in Parallel.* Springer.

COLOMBO, P. & DEGISCHER, H. P. 2010. Highly porous metals and ceramics. *Materials Science and Technology,* 26**,** 1145-1158.

CONNELL, S. D. & STOW, P. 1986. The pressure correction method. *Computers & Fluids,* 14**,** 1-10.

COURANT, R., FRIEDRICHS, K. & LEWY, H. 1967. On the partial difference equations of mathematical physics. *IBM journal of Research and Development,* 11**,** 215-234.

CRAMER, C., FISCHER, P. & WINDHAB, E. J. 2004. Drop formation in a co-flowing ambient fluid. *Chemical Engineering Science,* 59**,** 3045-3058.

CUI, W., BEI, J., WANG, S., ZHI, G., ZHAO, Y., ZHOU, X., ZHANG, H. & XU, Y. 2005. Preparation and evaluation of poly(L-lactide-co-glycolide) (PLGA) microbubbles as a contrast agent for myocardial contrast echocardiography. *Journal of Biomedical Materials Research Part B: Applied Biomaterials,* 73B**,** 171-178.

DATE, A. W. 2003. Fluid dynamical view of pressure checkerboarding problem and smoothing pressure correction on meshes with colocated variables. *International Journal of Heat and Mass Transfer,* 46**,** 4885-4898.

DAVID, C. D., OLIVIER, J. A. S., SCOTT, T. B. & GEORGE, M. W. 1999. Rapid prototyping of microfluidic switches in poly(dimethyl siloxane) and their actuation by electro-osmotic flow. *Journal of Micromechanics and Microengineering,* 9**,** 211.

DE MELLO, A. 2002. Focus: plastic fantastic? *Lab on a Chip,* 2**,** 31N-36N.

DE MENECH, M., GARSTECKI, P., JOUSSE, F. & STONE, H. 2008. Transition from squeezing to dripping in a microfluidic T-shaped junction. *journal of fluid mechanics,* 595**,** 141-161.

DE VELLIS, A., GRITSENKO, D., LIN, Y., WU, Z., ZHANG, X., PAN, Y., XUE, W. & XU, J. 2017. Drastic sensing enhancement using acoustic bubbles for surface-based microfluidic sensors. *Sensors and Actuators B: Chemical,* 243**,** 298-302.

DEMEKHIN, E. A. & POLYANSKIKH, S. V. 2010. Stability of a viscous liquid microjet in DC and AC electric fields. *Fluid Dynamics,* 45**,** 719-733.

DEMIRDŽIĆ, I. & PERIĆ, M. 1990. Finite volume method for prediction of fluid flow in arbitrarily shaped domains with moving boundaries. *International Journal for Numerical Methods in Fluids,* 10**,** 771-790.

DI CARLO, D. 2009. Inertial microfluidics. *Lab on a Chip,* 9**,** 3038-3046.

DING, B., KIM, H.-Y., LEE, S.-C., LEE, D.-R. & CHOI, K.-J. 2002. Preparation and characterization of nanoscaled poly(vinyl alcohol) fibers via electrospinning. *Fibers and Polymers,* 3**,** 73-79.

DOSHI, J. & RENEKER, D. H. Electrospinning process and applications of electrospun fibers. Industry Applications Society Annual Meeting, 1993., Conference Record of the 1993 IEEE, 1993. IEEE, 1698-1703.

DUTTA, D., RAMACHANDRAN, A. & LEIGHTON, D. T. 2006. Effect of channel geometry on solute dispersion in pressure-driven microfluidic systems. *Microfluidics and Nanofluidics,* 2**,** 275-290.

ELSAYED, M., KOTHANDARAMAN, A., EDIRISINGHE, M. & HUANG, J. 2016. Porous Polymeric Films from Microbubbles Generated Using a T-Junction Microfluidic Device. *Langmuir,* 32**,** 13377-13385.

ELZOGHBY, A. O., SAMY, W. M. & ELGINDY, N. A. 2012. Albumin-based nanoparticles as potential controlled release drug delivery systems. *Journal of Controlled Release,* 157**,** 168-182.

EMERSON, S. & BUSHINSKY, S. 2016. The role of bubbles during air-sea gas exchange. *Journal of Geophysical Research: Oceans,* 121**,** 4360-4376.

EMERSON, S., QUAY, P., KARL, D., WINN, C., TUPAS, L. & LANDRY, M. 1997. Experimental determination of the organic carbon flux from open-ocean surface waters. *Nature,* 389**,** 951.

EMERSON, S., QUAY, P., STUMP, C., WILBUR, D. & KNOX, M. 1991. O2, Ar, N2, and 222Rn in surface waters of the subarctic Ocean: Net biological O2 production. *Global Biogeochemical Cycles,* 5**,** 49-69.

ENAYATI, M., AHMAD, Z., STRIDE, E. & EDIRISINGHE, M. 2010. One-step electrohydrodynamic production of drug-loaded micro- and nanoparticles. *Journal of The Royal Society Interface,* 7**,** 667-675.

ENAYATI, M., CHANG, M.-W., BRAGMAN, F., EDIRISINGHE, M. & STRIDE, E. 2011. Electrohydrodynamic preparation of particles, capsules and bubbles for biomedical engineering applications. *Colloids and Surfaces A: Physicochemical and Engineering Aspects,* 382**,** 154-164.

ERNST, A., MUTSCHLER, K., TANGUY, L., PAUST, N., ZENGERLE, R. & KOLTAY, P. 2012. Numerical Investigations on Electric Field Characteristics with Respect to Capacitive Detection of Free-Flying Droplets. *Sensors*.

ESI-GROUP 2013. *CFD-ACEV2013.2 User Manual Part 2,* Huntsville, AL, ESI-Group.

FAN, Y., TANG, H. & WANG, Y. 2017. Synergistic Behavior and Microstructure Transition in Mixture of Zwitterionic Surfactant, Anionic Surfactant, and Salts in Sorbitol/H2O Solvent: 1. Effect of Surfactant Compositions. *Journal of Surfactants and Detergents,* 20**,** 435-443.

FANG, C., HIDROVO, C., WANG, F.-M., EATON, J. & GOODSON, K. 2008. 3-D numerical simulation of contact angle hysteresis for microscale two phase flow. *International Journal of Multiphase Flow,* 34**,** 690-705.

FAROOK, U., STRIDE, E., EDIRISINGHE, M. J. & MOALEJI, R. 2007a. Microbubbling by co-axial electrohydrodynamic atomization. *Medical & Biological Engineering & Computing,* 45**,** 781-789.

FAROOK, U., ZHANG, H., EDIRISINGHE, M., STRIDE, E. & SAFFARI, N. 2007b. Preparation of microbubble suspensions by co-axial electrohydrodynamic atomization. *Medical engineering & physics,* 29**,** 749-754.

FEI, K., CHEN, W. H. & HONG, C. W. 2008. Microfluidic analysis of CO2 bubble dynamics using thermal lattice-Boltzmann method. *Microfluidics and Nanofluidics,* 5**,** 119-129.

FEISTAUER, M. 2007. Finite Volume and Finite Element Methods in CFD (Numerical Simulation of Compressible Flow).

FESHITAN, J. A., CHEN, C. C., KWAN, J. J. & BORDEN, M. A. 2009. Microbubble size isolation by differential centrifugation. *Journal of colloid and interface science,* 329**,** 316-324.

FLEISCH, D. 2008. *A student's guide to Maxwell's equations*, Cambridge University Press.

FOKKEMA, D. R., SLEIJPEN, G. L. G. & VAN DER VORST, H. A. 1996. Generalized conjugate gradient squared. *Journal of Computational and Applied Mathematics,* 71**,** 125-146.

FORSBERG, F., BASUDE, R., LIU, J.-B., ALESSANDRO, J., SHI, W. T., RAWOOL, N. M., GOLDBERG, B. B. & WHEATLEY, M. A. 1999. Effect of filling gases on the backscatter from contrast microbubbles: theory and in vivo measurements. *Ultrasound in Medicine & Biology,* 25**,** 1203-1211.

FRENCH, D. J., BROWN, A. T., SCHOFIELD, A. B., FOWLER, J., TAYLOR, P. & CLEGG, P. S. 2016. The secret life of Pickering emulsions: particle exchange revealed using two colours of particle. *Scientific Reports,* 6**,** 31401.

GAO, M., CHENG, P. & QUAN, X. 2013. An experimental investigation on effects of an electric field on bubble growth on a small heater in pool boiling. *International Journal of Heat and Mass Transfer,* 67**,** 984-991.

GARG, D. K., SERRA, C. A., HOARAU, Y., PARIDA, D., BOUQUEY, M. & MULLER, R. 2015. New transformation proposed for improving CFD simulation of free radical polymerization reactions in microreactors. *Microfluidics and Nanofluidics,* 18**,** 1287-1297.

GARSTECKI, P., FUERSTMAN, M. J., STONE, H. A. & WHITESIDES, G. M. 2006. Formation of droplets and bubbles in a microfluidic T-junction—scaling and mechanism of break-up. *Lab on a Chip,* 6**,** 437-446.

GARSTECKI, P., GANAN-CALVO, A. & WHITESIDES, G. 2005a. Formation of bubbles and droplets in microfluidic systems. *Technical sciences,* 53.

GARSTECKI, P., GITLIN, I., DILUZIO, W., WHITESIDES, G. M., KUMACHEVA, E. & STONE, H. A. 2004. Formation of monodisperse bubbles in a microfluidic flow-focusing device. *Applied Physics Letters,* 85**,** 2649-2651.

GARSTECKI, P., STONE, H. A. & WHITESIDES, G. M. 2005b. Mechanism for Flow-Rate Controlled Breakup in Confined Geometries: A Route to Monodisperse Emulsions. *Physical Review Letters,* 94**,** 164501.

GAUDIOSO, J. & CRAIGHEAD, H. G. 2002. Characterizing electroosmotic flow in microfluidic devices. *Journal of Chromatography A,* 971**,** 249-253.

GEORGE, J. E., CHIDANGIL, S. & GEORGE, S. D. 2017. A study on air bubble wetting: Role of surface wettability, surface tension, and ionic surfactants. *Applied Surface Science,* 410**,** 117-125.

GERLACH, D., TOMAR, G., BISWAS, G. & DURST, F. 2006. Comparison of volume-of-fluid methods for surface tension-dominant two-phase flows. *International Journal of Heat and Mass Transfer,* 49**,** 740-754.

GESCHKE, O., KLANK, H. & TELLEMAN, P. 2006. *Microsystem Engineering of Lab-on-a-chip Devices*, Wiley.

GHELICH, R., KEYANPOUR-RAD, M. & YUZBASHI, A. 2013. Study on morphology and size distribution of electrospun NiO–GDC composite nanofibers. *J. Eng. Fibers Fabr*.

GLAWDEL, T., ELBUKEN, C. & REN, C. L. 2012. Droplet formation in microfluidic T-junction generators operating in the transitional regime. I. Experimental observations. *Physical Review E,* 85**,** 016322.

GLOCKNER, P. & NATERER, G. 2006. Numerical simulation of electrokinetic flow and heat transfer in microchannels with a finite-volume method. *Numerical Heat Transfer, Part A: Applications,* 49**,** 451-470.

GOBBY, D., ANGELI, P. & GAVRIILIDIS, A. 2001. Mixing characteristics of T-type microfluidic mixers. *Journal of Micromechanics and Microengineering,* 11**,** 126.

GONZENBACH, U. T., STUDART, A. R., TERVOORT, E. & GAUCKLER, L. J. 2006. Ultrastable Particle-Stabilized Foams. *Angewandte Chemie International Edition,* 45**,** 3526-3530.

GOU, S., ZHANG, Q., MA, Y., LI, S., ZHOU, Y., FEI, Y., WU, Y. & HE, Z. 2017. Self-assembled acrylamide-based copolymer/surfactant with high-temperature resistance for enhanced oil recovery. *Journal of applied polymer science,* 134**,** 45202.

GRINSTAFF, M. W. & SUSLICK, K. S. 1991. Air-filled proteinaceous microbubbles: synthesis of an echo-contrast agent. *Proceedings of the National Academy of Sciences,* 88**,** 7708-7710.

GUNDUZ, O., AHMAD, Z., STRIDE, E. & EDIRISINGHE, M. 2013. Continuous generation of ethyl cellulose drug delivery nanocarriers from microbubbles. *Pharmaceutical research,* 30**,** 225-237.

GÜNTHER, A. & JENSEN, K. F. 2006. Multiphase microfluidics: from flow characteristics to chemical and materials synthesis. *Lab on a Chip,* 6**,** 1487-1503.

GUO, F. & CHEN, B. 2009. Numerical Study on Taylor Bubble Formation in a Micro-channel T-Junction Using VOF Method. *Microgravity Science and Technology,* 21**,** 51-58.

GUPTA, A. & KUMAR, R. 2010. Effect of geometry on droplet formation in the squeezing regime in a microfluidic T-junction. *Microfluidics and Nanofluidics,* 8**,** 799-812.

GWENAELLE, M. P. O., JUNG, J., CHOI, Y. & LEE, S. 2017. Effect of microbubbles on microfiltration pretreatment for seawater reverse osmosis membrane. *Desalination,* 403**,** 153-160.

HANOTU, J., BANDULASENA, H. C. H., CHIU, T. Y. & ZIMMERMAN, W. B. 2013. Oil emulsion separation with fluidic oscillator generated microbubbles. *International Journal of Multiphase Flow,* 56**,** 119-125.

HANOTU, J., KONG, D. & ZIMMERMAN, W. B. 2016. Intensification of yeast production with microbubbles. *Food and Bioproducts Processing,* 100**,** 424-431.

HARDT, S. & SCHÖNFELD, F. 2003. Laminar mixing in different interdigital micromixers: II. Numerical simulations. *AIChE Journal,* 49**,** 578-584.

HARTMAN, R. P. A., BRUNNER, D., CAMELOT, D., MARIJNISSEN, J. & SCARLETT, B. 1999. Electrohydrodynamic atomization in the cone–jet mode physical modeling of the liquid cone and jet. *Journal of Aerosol science,* 30**,** 823-849.

HAWKER, N. A. & VENTIKOS, Y. 2012. Interaction of a strong shockwave with a gas bubble in a liquid medium: a numerical study. *Journal of Fluid Mechanics,* 701**,** 59-97.

HEKMATI, A. H., RASHIDI, A., GHAZISAEIDI, R. & DREAN, J.-Y. 2013. Effect of needle length, electrospinning distance, and solution concentration on morphological properties of polyamide-6 electrospun nanowebs. *Textile Research Journal***,** 0040517512471746.

HENRIQUES, C., VIDINHA, R., BOTEQUIM, D., BORGES, J. & SILVA, J. 2009. A systematic study of solution and processing parameters on nanofiber morphology using a new electrospinning apparatus. *Journal of nanoscience and nanotechnology,* 9**,** 3535-3545.

HETTIARACHCHI, K., TALU, E., LONGO, M. L., DAYTON, P. A. & LEE, A. P. 2007. On-chip generation of microbubbles as a practical technology for manufacturing contrast agents for ultrasonic imaging. *Lab on a Chip,* 7**,** 463-468.

HOANG, D. A., VAN STEIJN, V., PORTELA, L. M., KREUTZER, M. T. & KLEIJN, C. R. 2013. Benchmark numerical simulations of segmented two-phase flows in microchannels using the Volume of Fluid method. *Computers & Fluids,* 86**,** 28-36.

HOHMAN, M. M., SHIN, M., RUTLEDGE, G. & BRENNER, M. P. 2001. Electrospinning and electrically forced jets. II. Applications. *Physics of fluids,* 13**,** 2221-2236.

HONG, Y. & WANG, F. 2007. Flow rate effect on droplet control in a co-flowing microfluidic device. *Microfluidics and Nanofluidics,* 3**,** 341-346.

HOSSAIN, M., KHAN, A. Y. & SURESH KUMAR, G. 2011. Interaction of the Anticancer Plant Alkaloid Sanguinarine with Bovine Serum Albumin. *PLOS ONE,* 6**,** e18333.

HUANG, J., JAEGLE, L. & JAEGLÉ, L. 2017. Wintertime enhancements of sea salt aerosol in polar regions consistent with a sea ice source from blowing snow. *Atmospheric Chemistry and Physics,* 17**,** 3699-3712.

HUNEITI, Z., BALACHANDRAN, W., MACHOWSKI, W. & ARNOLD, P. Harmonic spraying of conducting liquids employing AC-DC electric fields. Industry Applications Conference, 1995. Thirtieth IAS Annual Meeting, IAS '95., Conference Record of the 1995 IEEE, 8-12 Oct 1995 1995. 1493-1499 vol.2.

HUNEITI, Z., MACHOWSKI, W. & BALACHANDRAN, W. Excitation of electrohydrodynamic surface waves on a conducting liquid jet employing AC field. Industry Applications Conference, 1996. Thirty-First IAS Annual Meeting, IAS'96., Conference Record of the 1996 IEEE, 1996. IEEE, 1768-1774.

HUTCHISON, J. B., HARALDSSON, K. T., GOOD, B. T., SEBRA, R. P., LUO, N., ANSETH, K. S. & BOWMAN, C. N. 2004. Robust polymer microfluidic device fabrication via contact liquid photolithographic polymerization (CLiPP). *Lab on a Chip,* 4**,** 658-662.

IWAMURA, C., COSTA, F. S., SBARSKI, I., EASTON, A. & LI, N. 2003. An efficient algebraic multigrid preconditioned conjugate gradient solver. *Computer methods in applied mechanics and engineering,* 192**,** 2299-2318.

JABESA, A. & GHOSH, P. 2016. Removal of diethyl phthalate from water by ozone microbubbles in a pilot plant. *Journal of Environmental Management,* 180**,** 476-484.

JAGANNATHAN, T. K., NAGARAJAN, R. & RAMAMURTHI, K. 2011. Effect of ultrasound on bubble breakup within the mixing chamber of an effervescent atomizer. *Chemical Engineering and Processing: Process Intensification,* 50**,** 305-315.

JANIB, S. M., MOSES, A. S. & MACKAY, J. A. 2010. Imaging and drug delivery using theranostic nanoparticles. *Advanced drug delivery reviews,* 62**,** 1052-1063.

JAUREGI, P. & VARLEY, J. 1999. Colloidal gas aphrons: potential applications in biotechnology. *Trends in Biotechnology,* 17**,** 389-395.

JAWOREK, A. 2007. Micro- and nanoparticle production by electrospraying. *Powder Technology,* 176**,** 18-35.

JAWOREK, A., MACHOWSKI, W., KRUPA, A. & BALACHANDRAN, W. Viscosity effect on EHD spraying using AC superimposed on DC electric field. Industry Applications Conference, 2000. Conference Record of the 2000 IEEE, 2000. IEEE, 770-776.

JIMENEZ, C., TALAVERA, B., SAEZ, C., CANIZARES, P., RODRIGO, M., JIMNEZ, C., SEZ, C. & CAIZARES, P. 2010. Study of the production of hydrogen bubbles at low current densities for electroflotation processes. *Journal of chemical technology and biotechnology,* 85**,** 1368-1373.

KAMHOLZ, A. E. & YAGER, P. 2001. Theoretical Analysis of Molecular Diffusion in Pressure-Driven Laminar Flow in Microfluidic Channels. *Biophysical Journal,* 80**,** 155-160.

KAUSHIK ARUMBULIYUR, C., ALI ASGAR, S. B., SUBHASHISH, D., IAN, P. & RUPAK, K. B. 2010. Transport and reaction of nanoliter samples in a microfluidic reactor using electro-osmotic flow. *Journal of Micromechanics and Microengineering,* 20**,** 035017.

KELLER, M. W., SEGAL, S. S., KAUL, S. & DULING, B. 1989. The behavior of sonicated albumin microbubbles within the microcirculation: a basis for their use during myocardial contrast echocardiography. *Circulation Research,* 65**,** 458.

KICKINGER, F. 1998. Algebraic Multi-grid for Discrete Elliptic Second-Order Problems. *In:* HACKBUSCH, W. & WITTUM, G. (eds.) *Multigrid Methods V: Proceedings of the Fifth European Multigrid Conference held in Stuttgart, Germany, October 1–4, 1996.* Berlin, Heidelberg: Springer Berlin Heidelberg.

KIESSLING, F., FOKONG, S., KOCZERA, P., LEDERLE, W. & LAMMERS, T. 2012. Ultrasound microbubbles for molecular diagnosis, therapy, and theranostics. *Journal of nuclear medicine,* 53**,** 345-348.

KIM, H.-H., KIM, J.-H. & OGATA, A. 2011. Time-resolved high-speed camera observation of electrospray. *Journal of Aerosol Science,* 42**,** 249-263.

KIM, H., LUO, D., LINK, D., WEITZ, D. A., MARQUEZ, M. & CHENG, Z. 2007. Controlled production of emulsion drops using an electric field in a flow-focusing microfluidic device. *Applied Physics Letters,* 91**,** 133106.

KIM, J., OH, H. & KIM, S. S. 2008. Electrohydrodynamic drop-on-demand patterning in pulsed cone-jet mode at various frequencies. *Journal of Aerosol Science,* 39**,** 819-825.

KIM, T. N., CAMPBELL, K., GROISMAN, A., KLEINFELD, D. & SCHAFFER, C. B. 2005. Femtosecond laser-drilled capillary integrated into a microfluidic device. *Applied Physics Letters,* 86**,** 201106.

KIRBY, B. J. & HASSELBRINK, E. F. 2004. Zeta potential of microfluidic substrates: 1. Theory, experimental techniques, and effects on separations. *Electrophoresis,* 25**,** 187-202.

KITCHIN, C. & COUNTS, L. 2004. *A designer's guide to instrumentation amplifiers*, Analog Devices.

KOTHANDARAMAN, A., EDIRISINGHE, M. & VENTIKOS, Y. 2017. *Microbubbles and their generation*. PCT/GB2016/053497.

KRAUSS JUILLERAT, F., GONZENBACH, U. T., ELSER, P., STUDART, A. R. & GAUCKLER, L. J. 2011. Microstructural Control of Self-Setting Particle-Stabilized Ceramic Foams. *Journal of the American Ceramic Society,* 94**,** 77-83.

KUCUK, I., AHMAD, Z., EDIRISINGHE, M. & ORLU-GUL, M. 2014. Utilization of microfluidic V-junction device to prepare surface itraconazole adsorbed nanospheres. *International Journal of Pharmaceutics,* 472**,** 339-346.

KURRAT, R., PRENOSIL, J. E. & RAMSDEN, J. J. 1997. Kinetics of Human and Bovine Serum Albumin Adsorption at Silica–Titania Surfaces. *Journal of Colloid and Interface Science,* 185**,** 1-8.

KWAN, J. J., KAYA, M., BORDEN, M. A. & DAYTON, P. A. 2012. Theranostic Oxygen Delivery Using Ultrasound and Microbubbles. *Theranostics,* 2**,** 1174-1184.

KWEON, Y., KIM, M., CHO, H. & KANG, I. 1998. Study on the deformation and departure of a bubble attached to a wall in dc/ac electric fields. *International Journal of Multiphase Flow,* 24**,** 145-162.

LAFAURIE, B., NARDONE, C., SCARDOVELLI, R., ZALESKI, S. & ZANETTI, G. 1994. Modelling Merging and Fragmentation in Multiphase Flows with SURFER. *Journal of Computational Physics,* 113**,** 134-147.

LAKEHAL, D., LARRIGNON, G. & NARAYANAN, C. 2007. Computational heat transfer and two-phase flow topology in miniature tubes. *Microfluidics and Nanofluidics,* 4**,** 261.

LAMI, E., MATTACHINI, F., SALA, R. & VIGL, H. 1997. A mathematical model of electrostatic field in wires-plate electrostatic precipitators. *Journal of Electrostatics,* 39**,** 1-21.

LANDFESTER, K., BECHTHOLD, N., TIARKS, F. & ANTONIETTI, M. 1999. Miniemulsion Polymerization with Cationic and Nonionic Surfactants: A Very Efficient Use of Surfactants for Heterophase Polymerization. *Macromolecules,* 32**,** 2679-2683.

LANGTANGEN, H. P. 1989. Conjugate gradient methods and ILU preconditioning of non-symmetric matrix systems with arbitrary sparsity patterns. *International Journal for Numerical Methods in Fluids,* 9**,** 213-233.

LANGTANGEN, H. P. 2013. *Computational Partial Differential Equations: Numerical Methods and Diffpack Programming*, Springer Berlin Heidelberg.

LASTOCHKIN, D. & CHANG, H.-C. 2005. A high-frequency electrospray driven by gas volume charges. *Journal of Applied Physics,* 97**,** 123309.

LASTOW, O. & BALACHANDRAN, W. 2007. Novel low voltage EHD spray nozzle for atomization of water in the cone jet mode. *Journal of electrostatics,* 65**,** 490-499.

LAUGA, E., BRENNER, M. P. & STONE, H. A. 2006. Microfluidics: the no-slip boundary condition. *Perspective,* 17.

LEE, M. H., PRASAD, V. & LEE, D. 2010. Microfluidic Fabrication of Stable Nanoparticle-Shelled Bubbles. *Langmuir,* 26**,** 2227-2230.

LEIGHTON, T. 2012. *The acoustic bubble*, Academic press.

LEONARD, B. P. & MOKHTARI, S. 1990. Beyond first-order upwinding: The ultra-sharp alternative for non-oscillatory steady-state simulation of convection. *International Journal for Numerical Methods in Engineering,* 30**,** 729-766.

LI, J. & ZHANG, P. 2009. Formation and droplet size of EHD drippings induced by superimposing an electric pulse to background voltage. *Journal of Electrostatics,* 67**,** 562-567.

LI, W. & ZHONG, W. 2015. CFD simulation of hydrodynamics of gas–liquid–solid three-phase bubble column. *Powder Technology,* 286**,** 766-788.

LI, Z. Y. & TAO, W. Q. 2002. A New Stability-Guaranteed Second-Order Difference Scheme. *Numerical Heat Transfer, Part B: Fundamentals,* 42**,** 349-365.

LIMA, E. G., DURNEY, K. M., SIRSI, S. R., NOVER, A. B., ATESHIAN, G. A., BORDEN, M. A. & HUNG, C. T. 2012. Microbubbles as biocompatible porogens for hydrogel scaffolds. *Acta Biomaterialia,* 8**,** 4334-4341.

LIMA, N. C. & D'ÁVILA, M. A. 2014. Numerical simulation of electrohydrodynamic flows of Newtonian and viscoelastic droplets. *Journal of Non-Newtonian Fluid Mechanics,* 213**,** 1-14.

LIN, Y. 2013. Two-phase electro-hydrodynamic flow modeling by a conservative level set model. *Electrophoresis,* 34**,** 736-744.

LINK, D., ANNA, S. L., WEITZ, D. & STONE, H. 2004. Geometrically mediated breakup of drops in microfluidic devices. *Physical review letters,* 92**,** 054503.

LIU, C., TANAKA, H., MA, J., ZHANG, L., ZHANG, J., HUANG, X. & MATSUZAWA, Y. 2012a. Effect of microbubble and its generation process on mixed liquor properties of activated sludge using Shirasu porous glass (SPG) membrane system. *Water Research,* 46**,** 6051-6058.

LIU, H. & ZHANG, Y. 2011. Droplet formation in microfluidic cross-junctions. *Physics of Fluids,* 23**,** 082101.

LIU, J.-L. 2010. Poisson's Equation in Electrostatics. unpublished.

LIU, J., SHANG, T., WANG, F., CAO, Y., HAO, L., REN, J., RAN, H., WANG, Z., LI, P. & DU, Z. 2017. Low-intensity focused ultrasound (LIFU)-induced acoustic droplet vaporization in phase-transition perfluoropentane nanodroplets modified by folate for ultrasound molecular imaging. *International journal of nanomedicine,* 12**,** 911-923.

LIU, S., WANG, Q., SUN, T., WU, C. & SHI, Y. 2012b. The effect of different types of micro-bubbles on the performance of the coagulation flotation process for coke waste-water. *Journal of Chemical Technology & Biotechnology,* 87**,** 206-215.

MAHALINGAM, S., MEINDERS, M. B. & EDIRISINGHE, M. 2014. Formation, stability, and mechanical properties of bovine serum albumin stabilized air bubbles produced using coaxial electrohydrodynamic atomization. *Langmuir,* 30**,** 6694-6703.

MAHALINGAM, S., XU, Z. & EDIRISINGHE, M. 2015. Antibacterial Activity and Biosensing of PVA-Lysozyme Microbubbles Formed by Pressurized Gyration. *Langmuir,* 31**,** 9771-9780.

MAHESHWARI, S. & CHANG, H.-C. 2006. Anomalous conical menisci under an ac field-departure from the dc Taylor cone. *Applied Physics Letters,* 89**,** 234103.

MAHESHWARI, S., CHETWANI, N. & CHANG, H.-C. 2009. Alternating current electrospraying. *Industrial & Engineering Chemistry Research,* 48**,** 9358-9368.

MANN, T. L. & KRULL, U. J. 2004. The application of ultrasound as a rapid method to provide DNA fragments suitable for detection by DNA biosensors. *Biosensors and Bioelectronics,* 20**,** 945-955.

MAO, L. & KOSER, H. 2006. Towards ferrofluidics for μ-TAS and lab on-a-chip applications. *Nanotechnology,* 17**,** S34.

MEIER, M., YADIGAROGLU, G. & SMITH, B. L. 2002. A novel technique for including surface tension in PLIC-VOF methods. *European Journal of Mechanics - B/Fluids,* 21**,** 61-73.

MILLER, D. B. & O'CALLAGHAN, J. P. 2017. New horizons for focused ultrasound (FUS) – therapeutic applications in neurodegenerative diseases. *Metabolism,* 69, Supplement**,** S3-S7.

MINOR, M., VINGERHOEDS, M. H., ZOET, F. D., DE WIJK, R. & VAN AKEN, G. A. 2009. Preparation and sensory perception of fat-free foams – effect of matrix properties and level of aeration. *International Journal of Food Science & Technology,* 44**,** 735-747.

MIRZAEE, I., SONG, M., CHARMCHI, M. & SUN, H. 2016. A microfluidics-based on-chip impinger for airborne particle collection. *Lab on a Chip,* 16**,** 2254-2264.

MITCHELL, P. 2001. Microfluidics--downsizing large-scale biology. *Nature biotechnology,* 19**,** 717.

MOHAMEDI, G., AZMIN, M., PASTORIZA-SANTOS, I., HUANG, V., PÉREZ-JUSTE, J., LIZ-MARZÁN, L. M., EDIRISINGHE, M. & STRIDE, E. 2012. Effects of Gold Nanoparticles on the Stability of Microbubbles. *Langmuir,* 28**,** 13808-13815.

MOSHKIN, N. P. & YAMBANGWAI, D. 2012. Numerical simulation of pressure-driven startup laminar flows through a planar T-junction channel. *Communications in Nonlinear Science and Numerical Simulation,* 17**,** 1241-1250.

MOTT, B., PACKWOOD, W., XIE, A., BELCIK, J. T., TAYLOR, R., ZHAO, Y., DAVIDSON, B. & LINDNER, J. 2016. Echocardiographic Ischemic Memory Imaging Through Complement-Mediated Vascular Adhesion?of

Phosphatidylserine-Containing Microbubbles. *JACC. Cardiovascular imaging,* 9**,** 937-946.

MOUNTFORD, P. A. & BORDEN, M. A. 2016. On the thermodynamics and kinetics of superheated fluorocarbon phase-change agents. *Advances in Colloid and Interface Science,* 237**,** 15-27.

MOVASSAT, M., ASHGRIZ, N. & BUSSMANN, M. 2015. Oscillation and breakup of a bubble under forced vibration. *International Journal of Heat and Fluid Flow,* 54**,** 211-219.

NABAVI, S. A., GU, S., VLADISAVLJEVIĆ, G. T. & EKANEM, E. E. 2015. Dynamics of double emulsion break-up in three phase glass capillary microfluidic devices. *Journal of Colloid and Interface Science,* 450**,** 279-287.

NAIR, A., THEVENOT, P., DEY, J., SHEN, J., SUN, M.-W., YANG, J. & TANG, L. 2010. Novel Polymeric Scaffolds Using Protein Microbubbles as Porogen and Growth Factor Carriers. *Tissue Engineering Part C: Methods,* 16**,** 23-32.

NARASIMHAN, J. & PAPAUTSKY, I. 2003. Polymer embossing tools for rapid prototyping of plastic microfluidic devices. *Journal of Micromechanics and Microengineering,* 14**,** 96.

NISISAKO, T., TORII, T. & HIGUCHI, T. 2002. Droplet formation in a microchannel network. *Lab on a Chip,* 2**,** 24-26.

O'BRIEN, F. J. 2011. Biomaterials & scaffolds for tissue engineering. *Materials Today,* 14**,** 88-95.

OPHIR, J. & PARKER, K. J. 1989. Contrast agents in diagnostic ultrasound. *Ultrasound in medicine & biology,* 15**,** 319-333.

OSHER, S. & SETHIAN, J. A. 1988. Fronts propagating with curvature-dependent speed: Algorithms based on Hamilton-Jacobi formulations. *Journal of Computational Physics,* 79**,** 12-49.

PAK KIN, W., TZA-HUEI, W., DEVAL, J. H. & CHIH-MING, H. 2004. Electrokinetics in micro devices for biotechnology applications. *IEEE/ASME Transactions on Mechatronics,* 9**,** 366-376.

PANCHOLI, K., STRIDE, E. & EDIRISINGHE, M. 2008a. Dynamics of bubble formation in highly viscous liquids. *Langmuir,* 24**,** 4388-4393.

PANCHOLI, K., STRIDE, E. & EDIRISINGHE, M. 2008b. Generation of microbubbles for diagnostic and therapeutic applications using a novel device. *Journal of drug targeting,* 16**,** 494-501.

PAPADAKIS, G. & BERGELES, G. 1995. A locally modified second order upwind scheme for convection terms discretization. *International Journal of Numerical Methods for Heat & Fluid Flow,* 5**,** 49-62.

PARHIZKAR, M., EDIRISINGHE, M. & STRIDE, E. 2013. Effect of operating conditions and liquid physical properties on the size of monodisperse microbubbles

produced in a capillary embedded T-junction device. *Microfluidics and nanofluidics,* 14**,** 797-808.

PARHIZKAR, M., EDIRISINGHE, M. & STRIDE, E. 2015. The effect of surfactant type and concentration on the size and stability of microbubbles produced in a capillary embedded T-junction device. *RSC Advances,* 5**,** 10751-10762.

PARHIZKAR, M., REARDON, P. J. T., KNOWLES, J. C., BROWNING, R. J., STRIDE, E., PEDLEY, R. B., GREGO, T. & EDIRISINGHE, M. 2017. Performance of novel high throughput multi electrospray systems for forming of polymeric micro/nanoparticles. *Materials & Design,* 126**,** 73-84.

PARHIZKAR, M., STRIDE, E. & EDIRISINGHE, M. 2014. Preparation of monodisperse microbubbles using an integrated embedded capillary T-junction with electrohydrodynamic focusing. *Lab on a Chip,* 14**,** 2437-2446.

PARK, J. I., NIE, Z., KUMACHEV, A. & KUMACHEVA, E. 2010. A microfluidic route to small CO 2 microbubbles with narrow size distribution. *Soft Matter,* 6**,** 630-634.

PATANKAR, N. A., JOSEPH, D. D., WANG, J., BARREE, R. D., CONWAY, M. & ASADI, M. 2002. Power law correlations for sediment transport in pressure driven channel flows. *International Journal of Multiphase Flow,* 28**,** 1269-1292.

PATANKAR, S. V. 1981. A calculation procedure for two-dimensional elliptic situations. *Numerical heat transfer,* 4**,** 409-425.

PATRACHARI, A. R., PODICHETTY, J. T. & MADIHALLY, S. V. 2012. Application of computational fluid dynamics in tissue engineering. *Journal of Bioscience and Bioengineering,* 114**,** 123-132.

PIERANSKI, P. 1980. Two-Dimensional Interfacial Colloidal Crystals. *Physical Review Letters,* 45**,** 569-572.

PLESSET, M. S. & PROSPERETTI, A. 1977. Bubble dynamics and cavitation. *Annual Review of Fluid Mechanics,* 9**,** 145-185.

PUGMIRE, D. L., WADDELL, E. A., HAASCH, R., TARLOV, M. J. & LOCASCIO, L. E. 2002. Surface Characterization of Laser-Ablated Polymers Used for Microfluidics. *Analytical Chemistry,* 74**,** 871-878.

QIAN, D. & LAWAL, A. 2006. Numerical study on gas and liquid slugs for Taylor flow in a T-junction microchannel. *Chemical Engineering Science,* 61**,** 7609-7625.

QIN, D., XIA, Y. & WHITESIDES, G. M. 2010. Soft lithography for micro-and nanoscale patterning. *Nature protocols,* 5**,** 491.

QUAN, X., CHEN, G. & CHENG, P. 2011. Effects of electric field on microbubble growth in a microchannel under pulse heating. *International Journal of Heat and Mass Transfer,* 54**,** 2110-2115.

RAEINI, A. Q., BLUNT, M. J. & BIJELJIC, B. 2012. Modelling two-phase flow in porous media at the pore scale using the volume-of-fluid method. *Journal of Computational Physics,* 231**,** 5653-5668.

RAFAILIDIS, V., CHRYSSOGONIDIS, I., TEGOS, T., KOUSKOURAS, K. & CHARITANTI-KOURIDOU, A. 2017. Imaging of the ulcerated carotid atherosclerotic plaque: a review of the literature. *Insights into Imaging,* 8**,** 213-225.

RAHIMPOUR, A., MADAENI, S. S. & MANSOURPANAH, Y. 2007. The effect of anionic, non-ionic and cationic surfactants on morphology and performance of polyethersulfone ultrafiltration membranes for milk concentration. *Journal of Membrane Science,* 296**,** 110-121.

RAHMANPOUR, M. & EBRAHIMI, R. 2016. Numerical simulation of electrohydrodynamic spray with stable Taylor cone–jet. *Heat and Mass Transfer,* 52**,** 1595-1603.

REIJNS, G. L. & LUO, J. 1992. *Transputing in numerical and neural network applications*, IOS Press.

RESHADI, M., SAIDI, M. H. & FIROOZABADI, B. 2016. Electrokinetic and aspect ratio effects on secondary flow of viscoelastic fluids in rectangular microchannels. *Microfluidics and Nanofluidics,* 20.

RIESS, J. G. 2002. Blood substitutes and other potential biomedical applications of fluorinated colloids. *Journal of Fluorine Chemistry,* 114**,** 119-126.

RIESS, J. G. 2003. Fluorocarbon-based injectable gaseous microbubbles for diagnosis and therapy. *Current Opinion in Colloid & Interface Science,* 8**,** 259-266.

RIESS, J. G. & KRAFFT, M. P. 1998. Fluorinated materials for in vivo oxygen transport (blood substitutes), diagnosis and drug delivery. *Biomaterials,* 19**,** 1529-1539.

RIJNS, J. 1996. CMOS low-distortion high-frequency variable-gain amplifier. *Solid-State Circuits, IEEE Journal of,* 31**,** 1029-1034.

ROSEN, M. J. & KUNJAPPU, J. T. 2012. *Surfactants and interfacial phenomena*, John Wiley & Sons.

ROSS, D., JOHNSON, T. J. & LOCASCIO, L. E. 2001. Imaging of Electroosmotic Flow in Plastic Microchannels. *Analytical Chemistry,* 73**,** 2509-2515.

ROSSI, S., WATON, G. & KRAFFT, M. P. 2010. Phospholipid-Coated Gas Bubble Engineering: Key Parameters for Size and Stability Control, as Determined by an Acoustical Method. *Langmuir,* 26**,** 1649-1655.

ROVERS, T. A. M., SALA, G., VAN DER LINDEN, E. & MEINDERS, M. B. J. 2016. Potential of Microbubbles as Fat Replacer: Effect on Rheological, Tribological and Sensorial Properties of Model Food Systems. *Journal of texture studies,* 47**,** 220-230.

SANTOS, R. M. & KAWAJI, M. 2010. Numerical modeling and experimental investigation of gas–liquid slug formation in a microchannel T-junction. *International Journal of Multiphase Flow,* 36**,** 314-323.

SARKAR, S., DEEVI, S. & TEPPER, G. 2007. Biased AC electrospinning of aligned polymer nanofibers. *Macromolecular rapid communications,* 28**,** 1034-1039.

SCHARFF, T. G. & MAUPIN, W. C. 1960. Correlation of the metabolic effects of benzalkonium chloride with its membrane effects in yeast. *Biochemical Pharmacology,* 5**,** 79-86.

SEEBERGH, J. E. & BERG, J. C. 1992. Dynamic wetting in the low capillary number regime. *Chemical Engineering Science,* 47**,** 4455-4464.

SEO, M., GORELIKOV, I., WILLIAMS, R. & MATSUURA, N. 2010. Microfluidic Assembly of Monodisperse, Nanoparticle-Incorporated Perfluorocarbon Microbubbles for Medical Imaging and Therapy. *Langmuir,* 26**,** 13855-13860.

SERTEL, K. & VOLAKIS, J. L. 2000. Incomplete LU preconditioner for FMM implementation.

SETHU, P., SIN, A. & TONER, M. 2006. Microfluidic diffusive filter for apheresis (leukapheresis). *Lab on a Chip,* 6**,** 83-89.

SHAMSI, A., SHAMLOO, A., MOHAMMADALIHA, N., HAJGHASSEM, H., MEHRABADI, J. F. & BAZZAZ, M. 2016. High throughput blood plasma separation using a passive PMMA microfluidic device. *Microsystem Technologies,* 22**,** 2447-2454.

SHAN, L. 2004. Perfluoropropane-filled, sorbitan monostearate–and polyoxyethylene 40 stearate–shelled nanobubbles. National Center for Biotechnology Information (US), Bethesda (MD).

SHEN, Y., LONGO, M. L. & POWELL, R. L. 2008a. Stability and rheological behavior of concentrated monodisperse food emulsifier coated microbubble suspensions. *Journal of Colloid and Interface Science,* 327**,** 204-210.

SHEN, Y., POWELL, R. L. & LONGO, M. L. 2008b. Interfacial and stability study of microbubbles coated with a monostearin/monopalmitin-rich food emulsifier and PEG40 stearate. *Journal of Colloid and Interface Science,* 321**,** 186-194.

SHIM, J., DUTTA, P. & IVORY, C. F. 2007. Finite-volume methods for isotachophoretic separation in microchannels. *Numerical Heat Transfer, Part A: Applications,* 52**,** 441-461.

SHUTTLEWORTH, R. R., ELMAN, H. C., LONG, K. R. & TEMPLETON, J. A. 2011. Fast solvers for models of ICEO microfluidic flows. *International Journal for Numerical Methods in Fluids,* 65**,** 383-404.

SHYY, W., THAKUR, S. & WRIGHT, J. 1992. Second-order upwind and central difference schemes for recirculatingflow computation. *AIAA journal,* 30**,** 923-932.

SIVASAMY, J., WONG, T.-N., NGUYEN, N.-T. & KAO, L. T.-H. 2011. An investigation on the mechanism of droplet formation in a microfluidic T-junction. *Microfluidics and Nanofluidics,* 11**,** 1-10.

SOH, G. Y., YEOH, G. H. & TIMCHENKO, V. 2016. Numerical investigation on the velocity fields during droplet formation in a microfluidic T-junction. *Chemical Engineering Science,* 139**,** 99-108.

SONTTI, S. G. & ATTA, A. 2017. CFD analysis of microfluidic droplet formation in non–Newtonian liquid. *Chemical Engineering Journal,* 330**,** 245-261.

SRIDHAR, S., PATEL, A. & DALVI, S. V. 2016. Estimation of Storage Stability of Aqueous Microbubble Suspensions. *Colloids and Surfaces A: Physicochemical and Engineering Aspects,* 489**,** 182-190.

SRIVASTAVA, Y., LOSCERTALES, I., MARQUEZ, M. & THORSEN, T. 2008. Electrospinning of hollow and core/sheath nanofibers using a microfluidic manifold. *Microfluidics and Nanofluidics,* 4**,** 245-250.

STEEGMANS, M. L. J., SCHROËN, K. G. P. H. & BOOM, R. M. 2009. Characterization of Emulsification at Flat Microchannel Y Junctions. *Langmuir,* 25**,** 3396-3401.

STONE, H. A., STROOCK, A. D. & AJDARI, A. 2004. Engineering flows in small devices: microfluidics toward a lab-on-a-chip. *Annu. Rev. Fluid Mech.,* 36**,** 381-411.

STRIDE, E. 2009. Physical Principles of Microbubbles for Ultrasound Imaging and Therapy. *Cerebrovascular Diseases,* 27(suppl 2)**,** 1-13.

STRIDE, E. & EDIRISINGHE, M. 2008. Novel microbubble preparation technologies. *Soft matter,* 4**,** 2350-2359.

STRIDE, E. & EDIRISINGHE, M. 2009. Novel preparation techniques for controlling microbubble uniformity: a comparison. *Medical & biological engineering & computing,* 47**,** 883-892.

STUBEN, P. T. A. K. 2012. Advanced algebraic multigrid application for the accelaration of groundwater simulations. *XIX International conference on water Resources.* University of Illinois at Urbana-Champaign.

STUDART, A. R., NELSON, A., IWANOVSKY, B., KOTYRBA, M., KUNDIG, A. A., DALLA TORRE, F. H., GONZENBACH, U. T., GAUCKLER, L. J. & LOFFLER, J. F. 2012. Metallic foams from nanoparticle-stabilized wet foams and emulsions. *Journal of Materials Chemistry,* 22**,** 820-823.

SZÍJJÁRTÓ, C., ROSSI, S., WATON, G. & KRAFFT, M. P. 2012. Effects of Perfluorocarbon Gases on the Size and Stability Characteristics of

Phospholipid-Coated Microbubbles: Osmotic Effect versus Interfacial Film Stabilization. *Langmuir,* 28**,** 1182-1189.

TAKEUCHI, S., GARSTECKI, P., WEIBEL, D. B. & WHITESIDES, G. M. 2005. An axisymmetric Flow-Focusing microfluidic device. *Advanced materials,* 17**,** 1067-1072.

TALU, E., LOZANO, M. M., POWELL, R. L., DAYTON, P. A. & LONGO, M. L. 2006. Long-Term Stability by Lipid Coating Monodisperse Microbubbles Formed by a Flow-Focusing Device. *Langmuir,* 22**,** 9487-9490.

TAMAMIDIS, P. & ASSANIS, D. N. 1993. Evaluation of various high-order-accuracy schemes with and without flux limiters. *International Journal for Numerical Methods in Fluids,* 16**,** 931-948.

TAN, S. H., SEMIN, B. & BARET, J.-C. 2014. Microfluidic flow-focusing in ac electric fields. *Lab on a Chip,* 14**,** 1099-1106.

TANDON, V., BHAGAVATULA, S. K., NELSON, W. C. & KIRBY, B. J. 2008. Zeta potential and electroosmotic mobility in microfluidic devices fabricated from hydrophobic polymers: 1. The origins of charge. *Electrophoresis,* 29**,** 1092-1101.

TANG, G., YAN, D., YANG, C., GONG, H., CHAI, J. C. & LAM, Y. C. 2006. Assessment of Joule heating and its effects on electroosmotic flow and electrophoretic transport of solutes in microfluidic channels. *Electrophoresis,* 27**,** 628-639.

TAYLOR, G. 1934. The formation of emulsions in definable fields of flow. *Proceedings of the Royal Society of London. Series A, Containing Papers of a Mathematical and Physical Character***,** 501-523.

TAYLOR, G. 1964. Disintegration of Water Drops in an Electric Field. *Proceedings of the Royal Society A Mathematical, Physical and Engineering sciences,* 280**,** 383-397.

TEH, S.-Y., LIN, R., HUNG, L.-H. & LEE, A. P. 2008. Droplet microfluidics. *Lab on a Chip,* 8**,** 198-220.

TEN, S. T., HASHIM, U., GOPINATH, S. C. B., LIU, W. W., FOO, K. L., SAM, S. T., RAHMAN, S. F. A., VOON, C. H. & NORDIN, A. N. 2017. Highly sensitive Escherichia coli shear horizontal surface acoustic wave biosensor with silicon dioxide nanostructures. *Biosensors and Bioelectronics,* 93**,** 146-154.

THORSEN, T., ROBERTS, R. W., ARNOLD, F. H. & QUAKE, S. R. 2001. Dynamic pattern formation in a vesicle-generating microfluidic device. *Physical review letters,* 86**,** 4163.

TRAN, S. B. Q., BYUN, D., NGUYEN, V. D. & KANG, T. S. 2009. Liquid meniscus oscillation and drop ejection by ac voltage, pulsed dc voltage, and superimposing dc to ac voltages. *Physical Review E,* 80**,** 026318.

TRONRUD, D. E. 1992. Conjugate-direction minimization: an improved method for the refinement of macromolecules. *Acta crystallographica. Section A, Foundations of crystallography,* 48**,** 912-916.

UNGER, E., PORTER, T., LINDNER, J. & GRAYBURN, P. 2014. Cardiovascular drug delivery with ultrasound and microbubbles. *Advanced drug delivery reviews,* 72**,** 110-126.

UNGER, E. C., PORTER, T., CULP, W., LABELL, R., MATSUNAGA, T. & ZUTSHI, R. 2004. Therapeutic applications of lipid-coated microbubbles. *Advanced Drug Delivery Reviews,* 56**,** 1291-1314.

UNGER, M. A., CHOU, H.-P., THORSEN, T., SCHERER, A. & QUAKE, S. R. 2000. Monolithic Microfabricated Valves and Pumps by Multilayer Soft Lithography. *Science,* 288**,** 113-116.

USHIKUBO, F. Y., OLIVEIRA, D. R. B., MICHELON, M. & CUNHA, R. L. 2015. Designing Food Structure Using Microfluidics. *Food Engineering Reviews,* 7**,** 393-416.

VAN DOORMAAL, J. & RAITHBY, G. 1984. Enhancements of the SIMPLE method for predicting incompressible fluid flows. *Numerical heat transfer,* 7**,** 147-163.

VAN SINT ANNALAND, M., DIJKHUIZEN, W., DEEN, N. & KUIPERS, J. 2006. Numerical simulation of behavior of gas bubbles using a 3-D front-tracking method. *AIChE Journal,* 52**,** 99-110.

VAN STEIJN, V., KLEIJN, C. R. & KREUTZER, M. T. 2010. Predictive model for the size of bubbles and droplets created in microfluidic T-junctions. *Lab on a Chip,* 10**,** 2513-2518.

VAN STEIJN, V., KREUTZER, M. T. & KLEIJN, C. R. 2007. μ-PIV study of the formation of segmented flow in microfluidic T-junctions. *Chemical Engineering Science,* 62**,** 7505-7514.

VAN WAMEL, A., KOOIMAN, K., HARTEVELD, M., EMMER, M., TEN CATE, F. J., VERSLUIS, M. & DE JONG, N. 2006. Vibrating microbubbles poking individual cells: Drug transfer into cells via sonoporation. *Journal of Controlled Release,* 112**,** 149-155.

VANKA, S. 1987. Second-order upwind differencing in a recirculating flow. *AIAA journal,* 25**,** 1435-1441.

VONNEGUT, B. & NEUBAUER, R. L. 1952. Production of monodisperse liquid particles by electrical atomization. *Journal of Colloid Science,* 7**,** 616-622.

WALKER, G. M. & BEEBE, D. J. 2002. A passive pumping method for microfluidic devices. *Lab on a Chip,* 2**,** 131-134.

WANG, J. 2016. Self-propelled affinity biosensors: Moving the receptor around the sample. *Biosensors and Bioelectronics,* 76**,** 234-242.

WANG, J., JOSEPH, D. D., PATANKAR, N. A., CONWAY, M. & BARREE, R. D. 2003. Bi-power law correlations for sediment transport in pressure driven channel flows. *International Journal of Multiphase Flow,* 29**,** 475-494.

WANG, K., LU, Y., XU, J., TAN, J. & LUO, G. 2011. Generation of micromonodispersed droplets and bubbles in the capillary embedded T-junction microfluidic devices. *AIChE journal,* 57**,** 299-306.

WARMING, R. & BEAM, R. M. 1976. Upwind second-order difference schemes and applications in aerodynamic flows. *AIAA J,* 14**,** 1241-1249.

WEN, H. B., WIJN, J. R. D., BLITTERSWIJK, C. A. V. & GROOT, K. D. 1999. Incorporation of bovine serum albumin in calcium phosphate coating on titanium. *Journal of Biomedical Materials Research,* 46**,** 245-252.

WEN, L. H., ISMAIL, A. B., MENON, P., SATHTHASIVAM, J., THU, K. & CHOON, N. K. 2011. Case studies of microbubbles in wastewater treatment. *Desalination and Water Treatment,* 30**,** 10-16.

WU, S.-Y., CHEN, C. C., TUNG, Y.-S., OLUMOLADE, O. O. & KONOFAGOU, E. E. 2015. Effects of the microbubble shell physicochemical properties on ultrasound-mediated drug delivery to the brain. *Journal of Controlled Release,* 212**,** 30-40.

WU, Y. & CLARK, R. L. 2008. Electrohydrodynamic atomization: a versatile process for preparing materials for biomedical applications. *Journal of Biomaterials Science, Polymer Edition,* 19**,** 573-601.

XIA, Y. & WHITESIDES, G. M. 1998. Soft lithography. *Annual review of materials science,* 28**,** 153-184.

XIANGCHUN, X. & DONGQING, L. 2004. Analysis of electrokinetic flow in microfluidic networks. *Journal of Micromechanics and Microengineering,* 14**,** 290.

XIE, J., LIM, L. K., PHUA, Y., HUA, J. & WANG, C.-H. 2006. Electrohydrodynamic atomization for biodegradable polymeric particle production. *Journal of Colloid and Interface Science,* 302**,** 103-112.

XING, Z., KE, H., WANG, J., ZHAO, B., YUE, X., DAI, Z. & LIU, J. 2010. Novel ultrasound contrast agent based on microbubbles generated from surfactant mixtures of Span 60 and polyoxyethylene 40 stearate. *Acta Biomaterialia,* 6**,** 3542-3549.

XU, J., LI, S., TAN, J. & LUO, G. 2008. Correlations of droplet formation in T-junction microfluidic devices: from squeezing to dripping. *Microfluidics and Nanofluidics,* 5**,** 711-717.

XU, J. H., LI, S. W., TAN, J., WANG, Y. J. & LUO, G. S. 2006. Preparation of highly monodisperse droplet in a T-junction microfluidic device. *AIChE Journal,* 52**,** 3005-3010.

XU, Q., NAKAJIMA, M., ICHIKAWA, S., NAKAMURA, N., ROY, P., OKADOME, H. & SHIINA, T. 2009. Effects of surfactant and electrolyte concentrations on bubble formation and stabilization. *Journal of Colloid and Interface Science,* 332**,** 208-214.

YAN, W.-C., ONG, X. J., PUN, K. T., TAN, D. Y., SHARMA, V. K., TONG, Y. W. & WANG, C.-H. 2017. Preparation of tPA-loaded microbubbles as potential theranostic agents: A novel one-step method via coaxial electrohydrodynamic atomization technique. *Chemical Engineering Journal,* 307**,** 168-180.

YAN, Y. Y., ZHANG, H. B. & HULL, J. B. 2004. NUMERICAL MODELING OF ELECTROHYDRODYNAMIC (EHD) EFFECT ON NATURAL CONVECTION IN AN ENCLOSURE. *Numerical Heat Transfer, Part A: Applications,* 46**,** 453-471.

YANG, U. M. 2006. *Parallel algebraic multigrid methods—high performance preconditioners*, Springer.

YEO, L. Y., GAGNON, Z. & CHANG, H.-C. 2005. AC electrospray biomaterials synthesis. *Biomaterials,* 26**,** 6122-6128.

YOSHIZAWA, S., TAKAGI, R. & UMEMURA, S.-I. 2017. Enhancement of High-Intensity Focused Ultrasound Heating by Short-Pulse Generated Cavitation. *Applied Sciences,* 7**,** 288.

YOUSSEF, R. M. & UNIVERSITY, W. V. 2007. *Modeling the Effect of a Spray on a Liquid Film on a Heated Surface*, West Virginia University.

ZELENY, J. 1914. The Electrical Discharge from Liquid Points, and a Hydrostatic Method of Measuring the Electric Intensity at Their Surfaces. *Physical Review,* 3**,** 69-91.

ZHAO, C.-X. & MIDDELBERG, A. P. J. 2011. Two-phase microfluidic flows. *Chemical Engineering Science,* 66**,** 1394-1411.

ZHAO, N. & QI, L. 2006. Low-Temperature Synthesis of Star-Shaped PbS Nanocrystals in Aqueous Solutions of Mixed Cationic/Anionic Surfactants. *Advanced Materials,* 18**,** 359-362.

ZHAO, Z.-Y., ZHANG, Q.-M., TAN, G.-L. & XU, J. 1991. A new preconditioner for CGS iteration in solving large sparse nonsymmetric linear equations in semiconductor device simulation. *IEEE transactions on computer-aided design of integrated circuits and systems,* 10**,** 1432-1440.

ZHENG, G.-F., LIU, H.-Y., XU, R., WANG, X., LIU, J., WANG, H. & SUN, D.-H. 2014. Alternating Current Electrohydrodynamic Printing of Microdroplets. *Journal of Nanomaterials,* 2014**,** 7.

ZHENG, J., HE, A., LI, J., XU, J. & HAN, C. C. 2006. Studies on the controlled morphology and wettability of polystyrene surfaces by electrospinning or electrospraying. *Polymer,* 47**,** 7095-7102.

ZHOU, W., OUYANG, J., ZHANG, L., SU, J., WANG, X. & YANG, B. 2016. Development of new finite volume schemes on unstructured triangular grid for simulating the gas-liquid two-phase flow. *International journal for numerical methods in fluids,* 81**,** 45-67.

ZHOU, Y., SESHIA, A. A. & HALL, E. A. H. Microfluidics-based acoustic microbubble biosensor. 2013 IEEE SENSORS, 3-6 Nov. 2013 2013. 1-4.

ZHU, J., ZHANG, P., QING, Y., WEN, K., SU, X., MA, L., WEI, J., LIU, H., HE, H. & XI, Y. 2017. Novel intercalation mechanism of zwitterionic surfactant modified montmorillonites. *Applied Clay Science,* 141**,** 265-271.

ZIAIE, B., BALDI, A., LEI, M., GU, Y. & SIEGEL, R. A. 2004. Hard and soft micromachining for BioMEMS: review of techniques and examples of applications in microfluidics and drug delivery. *Advanced Drug Delivery Reviews,* 56**,** 145-172.